The proton's and neutron's internal structures: a long overdue clarification of what is inside the atomic nucleus

András Kovács, Valery Zatelepin, Dmitry Baranov, Giorgio Vassallo, and Heikki Sipilä

Published by the Zitter Institute (zitter-institute.org). The book content does not necessarily represent a consensus of all Zitter Institute members.

ISBN 978-952-65314-6-5 (softcover)

ISBN 978-952-65314-7-2 (PDF)

ABSTRACT. To correctly interpret nuclear measurements, we strictly adhere to the foundational laws of Physics. We avoid paradoxical postulates, fantasy forces, fantasy particles, or curve-fitting parametrization. We show that an electron's and a proton's internal structures can be described through analogous approaches, the main difference being the topology of their Zitterbewegung. Our methodology enables the calculation of proton's radius and gyromagnetic ratio. The match between the calculated and experimentally measured proton parameters is remarkable, and cannot be coincidence. These results lead to the conclusion that the proton is an elementary particle. The electron and proton differ only in their mass and Zitterbewegung topology.

We compare our proton model against experiments designed to explore the proton's internal structure, such as deep inelastic electron-proton scattering experiments. We show that their raw experimental data is compatible with proton's Zitterbewegung structure, but contradicts the quark model assumptions. Specifically, quark proponents' presentation of contradicting experimental data as an experimental proof involves incompatible data mixing and untenable assumptions: we explain these mistakes, which evaded scientific scrutiny up to now. Historically, measurements of the extended proton structure drove speculation about its sub-particles; 20^{th} century particle physicists were forced to model elementary charges as infinitesimally small point-particles. By recognizing the proton's realistic Zitterbewegung structure, we can finally establish the compatibility between its elementary particle status and its measured physical dimensions.

To understand the precise meaning of proton-neutron difference, we survey relevant experiments. We also develop novel measurement methods; our experiments fill in a few missing gaps in the observation of nuclear phenomena. Numerous experiments converge to the same result: the neutron comprises two waves, carrying a positive and a negative elementary charge. A neutron can be split into a proton and a short-lived "nuclear electron", whose free-particle mass is 1.554 MeV. Conversely, a proton and a nuclear electron may combine into a neutron, with 0.26 MeV binding energy emission via gamma radiation.

At the end of this short journey, the reader is rewarded by understanding what comprises the matter we touch. As nuclear energy represents the highest known energy density, the rational development of nuclear technologies is critical for future progress. The correct knowledge of nuclear structures and interactions eventually becomes indispensable for nuclear technology development: the last three chapters introduce new technology perspectives, with experimental validation.

Contents

Foreword 4

Chapter 1. Particle mass as electromagnetic field energy 6

Bibliography 14

Chapter 2. Magnetic flux quantization and magnetic moment calculation 15

Bibliography 19

Chapter 3. A toroidal proton model that matches experimental data 20

Bibliography 35

Chapter 4. Proton spin and gyromagnetic factor 36

Chapter 5. Neutrinos and Occam's razor 40

Chapter 6. The discovery of nuclear electrons that appear during β-decay 46

Bibliography 64

Chapter 7. The neutron structure is deduced via a direct interpretation of experimental data 65

Bibliography 78

Chapter 8. Neutrino-induced inverse β-decay 79

Bibliography 84

Chapter 9. Nuclear chemistry with alpha particles: experimental signatures of neutral particles with $4N$ mass pattern 85

Bibliography 93

Chapter 10. A simple demonstration of nuclear electrons 94

Bibliography 98

Foreword

The development of quantum mechanics began with the discovery of the electron by J.J. Thompson in 1897 and culminated with the 1933 award of the Nobel Prize for physics to Erwin Schrödinger and Paul Dirac, essentially for developing the Dirac equation, a relativistic generalization of Schrödinger's equation for the electron. That provided a secure foundation for working out the rich experimental and theoretical implications of electron theory which continues to this day.

Birth of the Dirac equation is one of the most spectacular stories in scientific history. To mention some highlights: First, upon generalizing Schrödinger's equation with special relativity, the electron spin seemed to appear gratuitously without any additional assumption. That led many to conclude that "spin is a relativistic phenomenon." Instead, we now know from reformulation with geometric algebra that the i in Schrödinger's Hamiltonian should be recognized as a space-like bivector, representing constant spin. Hence geometry, not relativity is the origin of spin. Second, the Dirac wave function had double the degrees of freedom needed to describe a spinning electron, with a charge of opposite sign for each component. At first that seemed ideal for a single wave function describing both electron and proton, the only known charged particles at the time. But that hope was soon dashed by proof that both components must have the same mass. Then, like a bolt from the gods, Carl Anderson discovered the positron in 1932. That promoted the Dirac equation to the status of a complete theory of the electron, just in time to be recognized for the Nobel prize in 1933.

Since its inception in 1933, the original version of the Dirac equation has survived, unscathed, in every effort to modify it in any significant way. However, as harbinger of new physics to come, Dirac mentioned in his Nobel address the existence of puzzling high frequency solutions to the equation of motion, called "zitterbewegung" by Schrödinger.

Ironically, zitterbewegung had little impact on the development of quantum mechanics in subsequent decades. Some authors even claimed it can be eliminated completely by a change of variables. However, there was little consensus on the choice of variables and their physical significance. To address that issue, a systematic study of local observables using geometric algebra in Dirac theory was initiated, and an interim report was given in:

D. Hestenes, "The Zitterbewegung Interpretation of Quantum Mechanics", Foundations of Physics 20, 1213-1232 (1990)[1]

The essential features of the zitterbewegung interpretation are that the electron is modeled as a classical point particle with mass m and charge e, moving on a circular orbit at the speed of light c, around a center of mass $x(t)$. Electron energy is specified by the Einstein-Planck relation $mc^2 = \hbar\omega$, with equal kinetic and magnetic energy components specified by scalar and vector potentials in Maxwell's equation. These features have already been incorporated in models of the electron using the Dirac equation.

This small book follows that lead with a new proposal to model the proton with variables constrained in strict analogy to structure of the Dirac electron. The electron's circular orbit had already been generalized to a toroidal one, and that seemed to use up

[1] *Unfortunately, the published version is marred by numerous typos.*

all the degrees of freedom in a Dirac wave function. But this book notes that the torus can be partitioned into orthogonal toroidal and poloidal directions which adds one more degree of freedom. That seems to be the limit for modeling protons and electrons with Maxwell-Dirac electrodynamics.

With the preceding brief sketch of theoretical underpinnings, the balance of this book is devoted to experimental research and data analysis to probe the zitterbewegung structure in the proton and the neutron, in particular to evaluate evidence for a 1.5 MeV lepton in neutron beta decay.

David Hestenes

Emeritus Professor of Physics, Arizona State University

CHAPTER 1

Particle mass as electromagnetic field energy

Andras Kovacs[1]
[1] ExaFuse. E-mail: andras.kovacs@broadbit.com

1.1. Introduction

> "According to our present conceptions the elementary particles of matter are, in their essence, nothing else than condensations of the electromagnetic field" Einstein in 1920
>
> "You know, it would be sufficient to understand the electron" also Einstein

Understanding the electron is the basis for developing an understanding of other particles' inner structures. The above quotations show that the idea of equating particle mass with electromagnetic field energy was formulated already 100 years ago. However, the details of how to account for the electron's mass, spin, and scattering cross section remained ambiguous until recently.

Our work builds on the electron model described in the freely available reference [**1**]. While adhering to the foundational laws of physics, such as Maxwell's equation and Einstein's general relativity, this work gives tangible answers to fundamental questions, such as: what is the electron made of?, what generates the electron's spin?, what is the meaning of the experimentally measured Compton radius?, and what is the meaning of the experimentally measured classical electron radius? Moreover, it establishes a foundation for deducing the laws of quantum mechanics without making postulates.

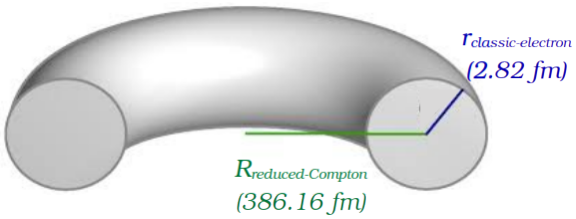

FIGURE 1.1.1. An illustration of the electron's particle aspect. The electron's charge moves at the speed of light within a torus whose major radius is the reduced Compton radius, and whose minor radius is classical electron radius. This circular Zitterbewegung motion generates the electron's spin.

Adapting the gaugeless electrodynamics approach from reference [**1**], we summarize in this chapter all the relevant electron and positron related formulas. Studying the reference [**1**] is thus optional for those readers who wish to understand gaugeless electrodynamics in more detail.

The electron's Zitterbewegung current circulates in a toroidally shaped volume, as illustrated in figure 1.1.1. The electron charge is carried by a longitudinal electromagnetic wave, that moves at the speed of light within a torus whose 386.16 fm major radius is the reduced Compton radius, and whose 2.82 fm minor radius is classical electron radius.

Neither radius value is constant however; they are inversely proportional to the electron energy. In this sense one cannot use high-energy scattering to measure "how large" the electron is, because with growing kinetic energy the outcome will show ever shrinking electron size.

The circular Zitterbewegung current within the torus of figure 1.1.1 generates the electron's spin.

The poloidal radius of this electron geometry directly shows up in electron-light interaction. At low frequency, electrons scatter light via the Thomson scattering process wherein the scattering cross section is similar to the 2.82 fm classical electron radius. At high frequency, electrons scatter light via the Compton scattering process wherein the scattering cross section is set by the 2.82 fm classical electron radius of the Klein-Nishina formula. The toroidal Compton radius calculation is described in the following section.

There are two equivalent ways of calculating the electron mass. The trivial approach is to integrate the energy density of electric and magnetic fields over all of space. The second approach is to integrate the electromagnetic Lagrangian density within the toroidal volume. In the following we focus on this second approach because it turns out to be very relevant for nuclear interactions as well. At the end of the chapter, we will show that these two approaches yield the same electron mass.

1.2. Gaugeless electrodynamics

1.2.1. The electromagnetic Lagrangian density. Transversal electromagnetic waves are trivial solutions of Maxwell's equation. Such transversal electromagnetic waves may travel millions of kilometers across vacuum. Upon entering the curved space-time region in the vicinity of a nucleus, the trivial electromagnetic wave may generate an electron-positron particle pair. The electromagnetic four-potential can thus be seen as the field, a "*Materia Prima*", from which the physical entities that we call "electrons" and "positrons" are generated. It is therefore reasonable to universally apply this approach to all charged elementary particles.

Leaving behind the experimentally paradoxical hypothesis of electromagnetic gauges [**2, 3**], we do not assume the presence of any electromagnetic gauge, and arrive at the simplest form of Maxwell's equation [**1**]:

$$\boldsymbol{\partial}^2 \boldsymbol{A}_{\square} = 0 \tag{1.2.1}$$

where the $\boldsymbol{A}_{\square}$ notation refers to the electromagnetic four-potential $\boldsymbol{A}_{\square} = \boldsymbol{A} + \gamma_t V$, and γ_t is the Clifford basis vector along the time direction. The electric charges and currents then correspond to a scalar field component of the electromagnetic field. As required by Maxwell's equation, this charged surface is moving at light speed, and is characterized by a vector potential $\boldsymbol{A}$, an electric potential V, a mechanical momentum $m\boldsymbol{c} = e\boldsymbol{A}$, and an angular speed $\omega = eV$.

Prior to reference [**1**], gaugeless electrodynamics has been already introduced and explored by other authors [**4, 5, 6**]. Most of these preceding works introduce the electromagnetic scalar field as an additional entity besides charges and currents, rather than the entity that actually produces the apparent charges and currents. A notable exception is the work of Giuliano Bettini that recognizes the electromagnetic sources as the partial derivatives of the scalar field.

Before exploring how gaugeless electrodynamics applies to a proton, which will be discussed in chapter 3, we firstly review how it applies to a positron.

To calculate a particle's properties, we must start from the electromagnetic Lagrangian density, which can be derived from the $\boldsymbol{\partial}^2 \boldsymbol{A}_{\square} = 0$ equation [**1**]:

(1.2.2)
$$\mathscr{L} = \frac{1}{2\mu_0}\boldsymbol{\partial A}_{\square}\widetilde{\boldsymbol{\partial A}_{\square}} = \frac{1}{2\mu_0}\boldsymbol{G}\widetilde{\boldsymbol{G}} = \frac{1}{2\mu_0}\|\boldsymbol{G}\|^2 = \frac{1}{2\mu_0}(S+\boldsymbol{F})(S-\boldsymbol{F}) = \frac{1}{2\mu_0}\left(S^2-\boldsymbol{F}^2\right) =$$
$$= \frac{1}{2\mu_0}\left(-\frac{E^2}{c^2}+B^2+S^2-\frac{2}{c}\mathcal{I}\boldsymbol{E}\cdot\boldsymbol{B}\right)$$

where $\mathcal{I}$ is the Clifford pseudo-scalar, $\boldsymbol{G}$ is the generalized electromagnetic field, S is the electromagnetic scalar field, and $\boldsymbol{F}$ is the usual scalar-free electromagnetic field:

(1.2.3)
$$\boldsymbol{F} = \frac{1}{c}\boldsymbol{E}\gamma_t + \mathcal{I}\boldsymbol{B}\gamma_t = \frac{1}{c}(\boldsymbol{E}+\mathcal{I}c\boldsymbol{B})\gamma_t$$

The $\widetilde{\ }$ operator denotes Clifford reversion, which reverses the order of base vectors.

Essentially, equation 1.2.2 expresses that the electromagnetic Lagrangian density is the square of the generalized electromagnetic field strength.

As can be seen in the above expression, the electromagnetic Lagrangian density comprises two parts:

$$\mathscr{L} = \mathscr{L}_{\perp} + \mathscr{L}_{\parallel}$$

where $\mathscr{L}_{\perp} = \frac{1}{2\mu_0}\left(-\frac{E^2}{c^2}+B^2\right)$ is the Lorentz-invariant Lagrangian density of a transversal electromagnetic wave, and $\mathscr{L}_{\parallel} = \frac{1}{2\mu_0}\left(S^2-\frac{2}{c}\mathcal{I}\boldsymbol{E}\cdot\boldsymbol{B}\right)$ is the Lorentz-invariant Lagrangian density of a longitudinal electromagnetic wave. The transversal electromagnetic wave is well known, and has been the focus of electromagnetism studies over the past 150 years. The longitudinal electromagnetic wave is what nuclear scientists refer to as a light-speed moving "neutrino"; its electromagnetic nature shall be derived in chapter 5.

When a particle's momentum changes, it emits or absorbs a transversal electromagnetic wave. When a particle's internal structure changes changes, e.g. in $\mu^+ \to e^+$ decays, it emits a longitudinal electromagnetic wave. This fact highlights the key importance of $\mathscr{L}_{\parallel}$ for understanding a particle's internal structure.

The $\mathscr{L}_{\parallel} = \frac{1}{2\mu_0}\left(S^2-\frac{2}{c}\mathcal{I}\boldsymbol{E}\cdot\boldsymbol{B}\right)$ Lagrangian density can be also written as $\mathscr{L}_{\parallel} = \boldsymbol{J}_{\square}\cdot\boldsymbol{A}_{\square}$. This equivalence is derived in the first appendix. The $\mathscr{L}_{\perp} = \frac{1}{2\mu_0}\left(-\frac{E^2}{c^2}+B^2\right)$ and $\mathscr{L}_{\parallel} = \boldsymbol{J}_{\square}\cdot\boldsymbol{A}_{\square}$ terms are well-known in the scientific literature, and are referred to as the "field term" and "interaction term" of the electromagnetic Lagrangian density[1].

In the following paragraphs, we show that the elementary charge is characterized by a simple Lagrangian $L_{\parallel}$ that defines the action $\mathscr{S}$:

(1.2.4)
$$L_{\parallel} = \int \boldsymbol{J}_{\square}\cdot\boldsymbol{A}_{\square}\,dv\,dt = e\boldsymbol{A}\cdot\boldsymbol{c} - eV$$

$$\mathscr{S} = \int L_{\parallel}dt$$

where the $e\boldsymbol{A}$ term describes the Zitterbewegung momentum of the elementary charge, eV term describes its electric energy, and $\boldsymbol{J}_{\square}$ is the averaged internal four-current density of the particle. The dv and dt terms represent the infinitesimal volume and time elements of the space-time integral.

[1] In the following, we also use the $\mathscr{L}_{\parallel} = \boldsymbol{J}_{\square}\cdot\boldsymbol{A}_{\square}$ formulation. The significance of knowing the $\mathscr{L}_{\parallel} = \frac{1}{2\mu_0}\left(S^2-\frac{2}{c}\mathcal{I}\boldsymbol{E}\cdot\boldsymbol{B}\right)$ formulation is that it reveals the connection with longitudinal electromagnetic waves.

The stationary action condition $\delta\mathscr{S} = 0$ is can be written as:

$$\mathscr{S} = \int (e\boldsymbol{A}\cdot\boldsymbol{c} - eV)\, dt = e\int \boldsymbol{A}\cdot\boldsymbol{dl} - e\int V dt = 0$$

$$\delta\mathscr{S} = 0$$

The stationary action condition is satisfied when the elementary charge's electromagnetic four potential $\boldsymbol{A}_{\square} = \boldsymbol{A} + \gamma_t V$ is a nilpotent vector: $\boldsymbol{A}_{\square}^2 = 0$. This $\boldsymbol{A}_{\square}^2 = 0$ condition leads to the well-known magnetic and electric Aharonov-Bohm relations between the electromagnetic phase φ and the electromagnetic four potential:

$$\varphi = \frac{e}{\hbar}\int \boldsymbol{A}\cdot d\boldsymbol{l} \tag{1.2.5}$$

$$\varphi = \frac{e}{\hbar}\int_T V dt \tag{1.2.6}$$

Considering circular Zitterbewegung, we shall now show that identifying φ with the Zitterbewegung phase leads to the Aharonov-Bohm relations. As $\boldsymbol{A}$ and $\boldsymbol{c}$ are parallel vectors for a freely moving charge, it's possible to substitute the dot product with the product of their norm:

$$L_{\parallel} = eAc - eV = eA\frac{dl}{dt} - eV$$

If the radius of the charge's Zitterbewegung trajectory is r, the differential of the displacement dl can be substituted by the $rd\varphi$ product:

$$dl = rd\varphi$$

$$L_{\parallel} = eAr\frac{d\varphi}{dt} - eV$$

Consequently, the following simple conditions guarantee that the action $\mathscr{S}$ is always zero:

$$eAr = \hbar = 1$$

$$\frac{d\varphi}{dt} = eV = eA = \frac{1}{r}$$

$$r^{-1} = \frac{d\varphi}{dt} = \omega = m$$

In natural units, the electron's or positron's mass-energy is equal to its Zitterbewegung angular speed, to the inverse of its Zitterbewegung radius, and to the absolute value of its Zitterbewegung momentum eA.

The $eV = eA$ condition is equivalent to the $\boldsymbol{A}_{\square}^2 = 0$ condition on the electromagnetic four potential, and it is easy to see that the above listed three conditions directly lead to the Aharonov-Bohm relations.

One may also understand the $r^{-1} = m$ relation as a consequence of Lorentz transformation. When a particle having rest mass m_0 is observed from a reference frame boosted by a Lorentz boost factor γ_L, its mass becomes $\gamma_L m_0$ from the perspective of the boosted reference frame. Keeping in mind that circular Zittebewegung comprises electromagnetic waves that are perpendicular to the axial direction of particle motion, the transversal relativistic Doppler shift will change these electromagnetic wavelengths by γ_L^{-1} factor. In

the axial direction, the particle size changes also by γ_L^{-1} factor because of Lorentz contraction. Therefore, from the perspective of the boosted reference frame, the particle size changes by γ_L^{-1} factor, leading to the $r^{-1} = m$ relation.

The principles introduced in this section may be considered as a powerful tool for modeling the structure and properties of elementary charged particles. To illustrate them in practice, we apply them to the positron in the following paragraphs.

1.2.2. The calculation of electron's and positron's mass value. One may compute the electron's or positron's mass from the Lagrangian density, which is measured in $\mathrm{J/m^3}$ units. To see this, we evaluate the positron's electromagnetic field energy starting from $\mathscr{L}_{\parallel}$:

$$\mathscr{L}_{\parallel} = \boldsymbol{J} \cdot \boldsymbol{A} = JA = \frac{I_{positron}}{\pi r_{cl}^2} \cdot \frac{\hbar}{e r_{ZBW}} \approx 1.352\,604 \cdot 10^{27}\ \mathrm{J \cdot m^{-3}}$$

where r_{cl}=2.82 fm is the minor toroidal radius, r_{ZBW}=386.16 fm is the major toroidal radius, and $I_{positron} = e\frac{c}{2\pi r_{ZBW}}$ is the Zitterbewegung current. It is interesting to note that the ratio of the two toroidal radii shown in figure 1.1.1 is exactly the fine structure constant: $r_{cl}/r_{ZBW} = \alpha$.

By integrating over the toroidal volume shown in figure 1.1.1, where the scalar field S is non-zero, it is possible to compute the positron's energy:

$$W_{positron} = \iiint_V JA\, dv = \frac{I_{positron}}{\pi r_{cl}^2} \cdot \frac{\hbar}{e r_{ZBW}} \cdot 2\pi^2 r_{ZBW} r_{cl}^2 = \phi I_{positron} = \frac{\hbar c}{r_{ZBW}} \approx 511\ \mathrm{keV}$$

The ϕ term appearing in the above expression is the magnetic flux of the electron's or positron's internal charge circulation; this term shall be in the focus of chapter 2.

1.2.3. The electron's and positron's quantum mechanical wave-function. In the electron's or positron's rest frame, equation 1.2.6 defines the time-wise evolution of its Zitterbewegung phase: $\varphi = \frac{e}{\hbar}\int_T V dt$.

Consider a positron moving at speed v. In relation to light-speed, its speed is characterized by $\beta = \frac{v}{c}$, $\gamma_L = (1-\beta^2)^{-\frac{1}{2}}$ and rapidity w defined as $\gamma_L = \cosh w$. It follows that $\cosh^2 w - \sinh^2 w = 1$, $\tanh w = \beta$, and $\sinh w = \gamma_L \beta$.

A relativistic boost rotates the time and space axes into each other according to the following hyperbolic rotation matrix:

$$\begin{pmatrix} ct' \\ x' \end{pmatrix} = \begin{pmatrix} \cosh w & -\sinh w \\ -\sinh w & \cosh w \end{pmatrix} \begin{pmatrix} ct \\ x \end{pmatrix}$$

Therefore, the time-wise Zitterbewegung phase evolution of the rest frame acquires a spatial oscillation component in the boosted reference frame. Specifically, the Zitterbewegung frequency of the rest frame is $\frac{\omega}{2\pi} = \frac{m_0 c^2}{h}$, and the corresponding wavenumber in the boosted frame is:

$$\frac{k}{2\pi} = \frac{\omega}{2\pi}\frac{\sinh w}{c}$$

Evaluating the right side of the above equation, we obtain:

$$\frac{k}{2\pi} = \frac{m_0 c^2}{h}\frac{\gamma_L v}{c^2}$$

Rearranging the above equation, we finally obtain:

$$\hbar k = (\gamma_L m_0)\, v = mv = p_{kinetic}$$

We recognize the above result as the basic postulate of quantum mechanics. However, it is no longer a postulate in our case: the appearing quantum mechanical wave is simply the Lorentz transformed component of the positron's Zitterbewegung oscillation.

Historically, quantum mechanics has been established over a set of experimentally motivated postulates. An intense philosophical debate ensued over the past 100 years regarding the physical interpretation of these postulates. If gaugeless electrodynamics had been known 100 years ago, quantum mechanics would have been immediately recognized as its natural consequence. With these results, we can not only give a tangible answer to the "what is the positron made of?" question, but also give a specific answer to the "what is the physical meaning of the positron wave-function?" question.

Using the Aharonov-Bohm relations, the total energy conservation equation $E_t = E_{kinetic} + E_{potential}$ directly leads to the Schrödinger equation[2], and also satisfies the continuity requirement of the quantum mechanical phase. The quantum mechanical Aharonov-Bohm effect, which has been considered paradoxical up to now, also directly follows from our elementary particle model. These results transform quantum mechanics from a postulates-based science into a proofs-based science that is ultimately derived from Maxwell's equation.

Our positron model demonstrates that the electron and positron only differ in the sign of their electric charge. There is no need to assign a negative energy value to the positron's electromagnetic field energy, which would be a gross violation of Maxwell's equation and yet appears in many present-day quantum mechanics textbooks.

1.3. The equivalence between the two field energy calculation methods

1.3.1. Magnetic field energy calculation. Upon electron-positron annihilation, it follows from angular momentum conservation that the emerging electromagnetic wave carries these particles' angular momenta. It is experimentally known that such annihilation events produce two circularly polarized electromagnetic wave quanta, each carrying $\hbar$ angular momentum. Thus setting the positron's angular momentum to $\hbar$, which is also in line with the above-discussed stationary action for non-rotating reference frame, we obtain the norm of the vector potential experienced by the elementary charge:

$$eAr_{ZBW} = \hbar$$

$$A = \frac{\hbar}{er_{ZBW}}$$

Once we know the vector potential, it is possible to determine the magnetic flux produced by the rotating elementary charge by applying the circulation of the vector potential A:

$$\phi = \oint_{\lambda} A d\lambda = \int_0^{2\pi} \frac{\hbar}{er_{ZBW}} r_{ZBW} d\vartheta = 2\pi\frac{\hbar}{e} = \frac{h}{e} \approx 4.135\,667 \cdot 10^{-15}\ \mathrm{V \cdot s} \tag{1.3.1}$$

i.e. the magnetic flux crossing the Zitterbewegung loop is quantized. Now it is possible to calculate the magnetic energy stored in the positron current loop:

$$W_m = \frac{1}{2}\phi I_{positron} = \frac{1}{2} \cdot 2\pi\frac{\hbar}{e} \cdot \frac{ec}{2\pi r_{ZBW}} = \frac{\hbar c}{2r_{ZBW}} \approx 255.5\ \mathrm{keV}$$

[2]A detailed explanation of Schrödinger equation derivation from the Aharonov-Bohm equations can be found in reference [**1**].

which is equal to half the electron or positron rest mass. Electromagnetic induction requires that electric and magnetic field energies must be equal: this is the $W_e = W_m$ requirement of an electromagnetic wave. Consequently, the other half of field energy is electric, and thus the total electron or positron rest mass is 511 keV.

The above result establishes the equivalence between the two field energy counting methods presented in this chapter.

We note that most scientists assume the electron's and positron's intrinsic angular momentum to be $\frac{\hbar}{2}$, even though that assumption contradicts the above-discussed angular momentum conservation in electron-positron annihilation events. Experimentally, the electron's angular momentum is measured under the externally applied magnetic field, and the apparent $\frac{\hbar}{2}$ angular momentum value is just one component of the spin-precessing angular momentum vector: this component is parallel to the externally applied magnetic field. This Larmor spin-precession phenomenon of the electron's angular momentum vector is thoroughly discussed in reference [**7**], and we shall discuss the proton's Larmor spin-precession in chapter 4

1.3.2. The Compton scattering radius measurement as a proxy for electric field energy measurement. The Compton scattering cross-section measurement, which is evaluated via the Klein-Nishina formula, directly measures the radius of the volume element traced out by an elementary charge. This volume element is a torus in the electron's rest frame, and becomes a spiral from the perspective of a boosted reference frame.

The radius of this volume element, within which the elementary charge circulates, determines the particle's electric field energy because a charged particle's electric field lines terminate in this volume element. In other words, the electric potential that is experienced by the elementary charge is the summation of surrounding electric field energy. Keeping in mind the $W_e = W_m$ requirement of an electromagnetic wave, we may think of Compton scattering cross section measurement as particle mass measurement.

In the electron's rest frame, Compton scattering measurement yields the r_{cl}=2.82 fm classical electron radius. When the same scattering process is observed from a boosted reference frame, where the relativistic electron mass is $\gamma_L m_0$, the Compton scattering measurement shall yield the correspondingly smaller r_{cl}/γ_L scattering radius value. This relationship reflects the above-discussed phenomenon of the particle mass increasing due to the shrinking particle size; the shrinking of particle dimensions by γ_L factor implies a corresponding increase of electromagnetic field intensities around the elementary charge.

It follows that Compton scattering radius measurement is essentially a particle mass measurement. We shall see the usefulness of this technique in chapters 3 and 7.

With this understanding of particle mass as electromagnetic field energy, we are ready to take a closer look at magnetic flux quantization.

Appendix 1: The formulations of longitudinal Lagrangian density

We start from the $\mathscr{L}_{\parallel} = \frac{1}{2\mu_0}\left(S^2 - \frac{2}{c}\mathcal{I}\boldsymbol{E}\cdot\boldsymbol{B}\right)$ Lagrangian density term, which directly follows from the gaugeless Maxwell equation. We take its partial derivative with respect to various components of the electromagnetic four-potential $\boldsymbol{A}_{\square}$.

For the partial derivative along the time-wise γ_t Clifford basis vector we find

$$\begin{aligned}
-\gamma_t\frac{\partial\mathscr{L}_{\parallel}}{\partial A_t} &= -\gamma_t\frac{\partial}{\partial x}\frac{\partial\mathscr{L}_{\parallel}}{\partial\left(\frac{\partial A_t}{\partial x}\right)} - \gamma_t\frac{\partial}{\partial y}\frac{\partial\mathscr{L}_{\parallel}}{\partial\left(\frac{\partial A_t}{\partial y}\right)} - \gamma_t\frac{\partial}{\partial z}\frac{\partial\mathscr{L}_{\parallel}}{\partial\left(\frac{\partial A_t}{\partial z}\right)} - \gamma_t\frac{\partial}{\partial t}\frac{\partial\mathscr{L}_{\parallel}}{\partial\left(\frac{\partial A_t}{\partial t}\right)} = \\
&= \frac{\gamma_t}{\mu_0}\left(\mathcal{I}\frac{\partial B_x}{\partial x} + \mathcal{I}\frac{\partial B_y}{\partial y} + \mathcal{I}\frac{\partial B_z}{\partial z} + \frac{1}{c}\frac{\partial S}{\partial t}\right) = \frac{\gamma_t}{\mu_0}\left(\mathcal{I}\nabla\cdot\boldsymbol{B} + \frac{1}{c}\frac{\partial S}{\partial t}\right) = \\
&= \frac{\gamma_t}{\mu_0 c}\frac{\partial S}{\partial t} = \gamma_t J_t = -\gamma_t c\rho.
\end{aligned}$$

Integrating the above equation yields

$$\mathscr{L}_{\parallel}|_t = \int\frac{\partial\mathscr{L}_{\parallel}}{\partial A_t}dA_t = \int\frac{1}{\mu_0 c}\frac{\partial S}{\partial t}dA_t = \frac{1}{\mu_0 c}\frac{\partial S}{\partial t}A_t = -\frac{1}{\mu_0}\mu_0 c\rho A_t = -c\rho A_t = J_t A_t. \tag{1.3.2}$$

Analogously, for the component along γ_x we find

$$\begin{aligned}
\gamma_x\frac{\partial\mathscr{L}_{\parallel}}{\partial A_x} &= \gamma_x\frac{\partial}{\partial x}\frac{\partial\mathscr{L}_{\parallel}}{\partial\left(\frac{\partial A_x}{\partial x}\right)} + \gamma_x\frac{\partial}{\partial y}\frac{\partial\mathscr{L}_{\parallel}}{\partial\left(\frac{\partial A_x}{\partial y}\right)} + \gamma_x\frac{\partial}{\partial z}\frac{\partial\mathscr{L}_{\parallel}}{\partial\left(\frac{\partial A_x}{\partial z}\right)} + \gamma_x\frac{\partial}{\partial t}\frac{\partial\mathscr{L}_{\parallel}}{\partial\left(\frac{\partial A_x}{\partial t}\right)} = \\
&= \frac{\gamma_x}{\mu_0}\left(\frac{\partial S}{\partial x} + \frac{\mathcal{I}}{c}\frac{\partial E_z}{\partial y} - \frac{\mathcal{I}}{c}\frac{\partial E_y}{\partial z} + \frac{\mathcal{I}}{c}\frac{\partial B_x}{\partial t}\right) = \frac{\gamma_x}{\mu_0}\frac{\partial S}{\partial x} = \gamma_x J_x
\end{aligned}$$

Integrating the above equation yields

$$\mathscr{L}_{\parallel}|_x = \int\left(\frac{\partial\mathscr{L}_{\parallel}}{\partial A_x}\right)dA_x = \int\frac{1}{\mu_0}\frac{\partial S}{\partial x}dA_x = \frac{1}{\mu_0}\frac{\partial S}{\partial x}A_x = J_x A_x$$

The same procedure is clearly valid also for the components in γ_y and γ_z. Finally, by summing up all components we get the $\mathscr{L}_{\parallel}$ term:

$$\mathscr{L}_{\parallel} = \sum_{j=x,y,z,t}\int\left(\frac{\partial\mathscr{L}_{\parallel}}{\partial A_j}\right)dA_j = J_{ex}A_x + J_{ey}A_y + J_{ez}A_z - c\rho A_t = \boldsymbol{J}_{\square}\cdot\boldsymbol{A}_{\square}$$

which is the usual "interaction" term that is added in traditional Lagrangian theory for classical electromagnetism in order to obtain the complete set of Maxwell's equations.

Bibliography

[1] A. Kovacs, G. Vassallo, A. O. Di Tommaso, and F. Celani "What is inside an electron: the physics of electromagnetic waves that are perceived as quantum mechanical waves", Zitter Institute (2025)

[2] G. Rousseaux "The gauge non-invariance of classical Electromagnetism", arXiv:physics/0506203v1

[3] P. J. Cote and M. A. Johnson "Groupthink and the blunder of the gauges", arXiv:0912.2977

[4] L. Hively et al "classical and extended electrodynamics", Physics Essays, Volume 32.1 (2019)

[5] D. A. Woodside "Three-vector and scalar field identities and uniqueness theorems in Euclidean and Minkowski spaces", American Journal of Physics, Volume 77.5 (2009)

[6] P. K. Anastasovski et al "Aharonov-Bohm effect as the basis of electromagnetic energy inherent in the vacuum", Foundations of Physics Letters, Volume 15 (2002)

[7] A. Kovacs and G. Vassallo "Rethinking Electron Statistics Rules", Symmetry, Volume 16.9 (2024)

CHAPTER 2

Magnetic flux quantization and magnetic moment calculation

Andras Kovacs[1]
[1] ExaFuse. E-mail: andras.kovacs@broadbit.com

2.1. Magnetic flux quantization of the electron spin

In this chapter, we study the electron's magnetic flux and magnetic moment. The obtained insights shall be then applied in the proton model development. The fundamental importance of magnetic flux quantization was suggested more than 50 years ago [**2**], and has been gaining attention recently [**1**].

Equation 1.3.1 of chapter 1 demonstrates that the magnetic flux of the electron or positron spin is $\Phi_M = {}^{h}/_{e}$, where h is the Planck constant and e is the elementary charge. I.e. the electron or positron Zitterbewegung is associated with ${}^{h}/_{e}$ magnetic flux quantum.

Since the Zitterbewegung of electron charge is at the speed of light, the circulating charge is characterized by a momentum p and energy E_e of purely electromagnetic nature:

$$(E_e\gamma_t, \boldsymbol{p})_{\square} = eA_{\square} \tag{2.1.1}$$

where $A_{\square}$ is the four-vector potential seen by the electron's charge, and $(E_e\gamma_t, \boldsymbol{p})_{\square}$ is the energy-momentum four-vector. $A_{\square}$ has the following components:

$$A_{\square} = V\gamma_t + \boldsymbol{A}_{\perp} + \boldsymbol{A}_{\parallel} \tag{2.1.2}$$

where $\boldsymbol{A}_{\parallel}$ is the vector potential along the Zitterbewegung circle, $\boldsymbol{A}_{\perp}$ is the axial vector potential perpendicular to the Zitterbewegung circle, V is the electric potential, γ_t is the basis vector along the time axis, and $\gamma_t^2 = -1$.

In the electron's rest frame, $\boldsymbol{A}_{\perp} = 0$ because there is no current along the Zitterbewegung axis.

While $A_{\parallel}$ depends on the reference frame from which we observe the electron, in the previous chapter we derived the $A_{\parallel} = \frac{\hbar}{er_{ZBW}}$ relation which ensures the invariance of spin magnetic flux in any reference frame:

$$\Phi_M = \oint_{\lambda} A_{\parallel} d\lambda = \int_0^{2\pi} \frac{\hbar}{er_{ZBW}} r_{ZBW} d\vartheta = 2\pi\frac{\hbar}{e} = \frac{h}{e} \tag{2.1.3}$$

2.2. Magnetic flux quantization of electron orbitals

Let r_{orb} be the mean radius of the electron orbital. The wavefunction's continuity requires that:

$$k\,(2\pi r_{orb}) = n2\pi \tag{2.2.1}$$

where n is positive integer number. It follows from equation 2.1.1 that the kinetic momentum defines the vector potential component along the Zitterbewegung axis:

$$p_{kinetic} = eA_{\perp} \tag{2.2.2}$$

Recaling the derivation of $p_{kinetic} = \hbar k$ from chapter 1, it is now possible to determine the magnetic flux of an electron orbital by applying the circulation of the vector potential $A_\perp$:

$$\phi_{orb} = \oint A_\perp d\lambda = \int_0^{2\pi} \frac{\hbar k}{e} r_{orb} d\vartheta = k\,(2\pi r_{orb})\,\frac{\hbar}{e} = n\frac{h}{e} \tag{2.2.3}$$

Therefore, the magnetic flux of electron orbitals is also quantized by elementary magnetic flux $\Phi_M = h/e$. This result further illustrates the fundamental nature of magnetic flux quantization.

2.3. Magnetic flux quantization of relativistic orbitals

When an inner-shell electron is bound to a heavy nucleus, such as Pb or Th, its magnetic moment deviates >10% from the free electron value [**3**]. Nevertheless, as we will show in the following paragraphs, its orbital magnetic flux quantum remains h/e. In this scenario, the inner-shell electron circulates at a relativistic speed, and the Thomas precession effect of its non-inertial reference frame must be taken into account. Since Thomas precession involves a rotation of the whole wavefunction, it does not alter the circulating wavenumber. Therefore, k remains the same before and after accounting for Thomas precession, and we can write $k_{lab} = k$. We discussed in section 2.2 the wavefunction continuity requirement, given by equation 2.2.1. This condition must be always fulfilled in the laboratory frame, otherwise there would be a wavefunction discontinuity. We must therefore write equation 2.2.1 for the laboratory frame, and using $k_{lab} = k$ we obtain:

$$k\,(2\pi r_{orb}) = n2\pi \tag{2.3.1}$$

As before, we use the $\hbar k = p_{kinetic}$ and $p_{kinetic} = eA_\perp$ formulas of section 2.2.1, to obtain $\hbar k = eA_\perp$. This $\hbar k = eA_\perp$ formula was derived via a relativistic transformation, so we can directly apply it in the relativistic electron case.

The relativistic orbit's magnetic flux can now be calculated from equation 2.2.3, by using the $\hbar k = eA_\perp$ relation together with the wavefunction continuity requirement given by equation 2.3.1. We thus arrive at equation 2.2.3 also in the relativistic electron case; it continues to yield $\phi_{orb} = n\frac{h}{e}$ magnetic flux value.

2.4. A precise magnetic moment calculation

The magnetic moment is traditionally given by the $\mu_B = \frac{e\hbar}{2m_e}$ formula, where the only non-constant parameter is the electron mass. This magnetic moment formula can be directly calculated from the electron structure, by calculating the area enclosed by the electron current. Neglecting the electron's charge radius, the electron magnetic moment is equal to the product between the current I_e and the enclosed area $\mathcal{A}_e$

$$\mu_B = I_e \mathcal{A}_e = \frac{e\omega_e}{2\pi}\pi r_e^2 = \frac{ec}{2} r_e = \frac{ec^2}{2\omega_e} = \frac{e\hbar}{2m_e} \tag{2.4.1}$$

where μ_B is being referred to as the Bohr magneton.

Measurements indicate that there is a small deviation between the experimental magnetic moment and the above formula. According to equation 2.4.1, the measurement of the electron's magnetic moment can be interpreted as a measurement of its mass. The presence of the small anomalous part means that the formula is not exactly correct, and the implicit assumptions going into this formula must be checked. It has the implicit

assumption that the dipole magnetic field is created by the electric charge, upon exactly one full rotation. Let us check whether this assumption is valid.

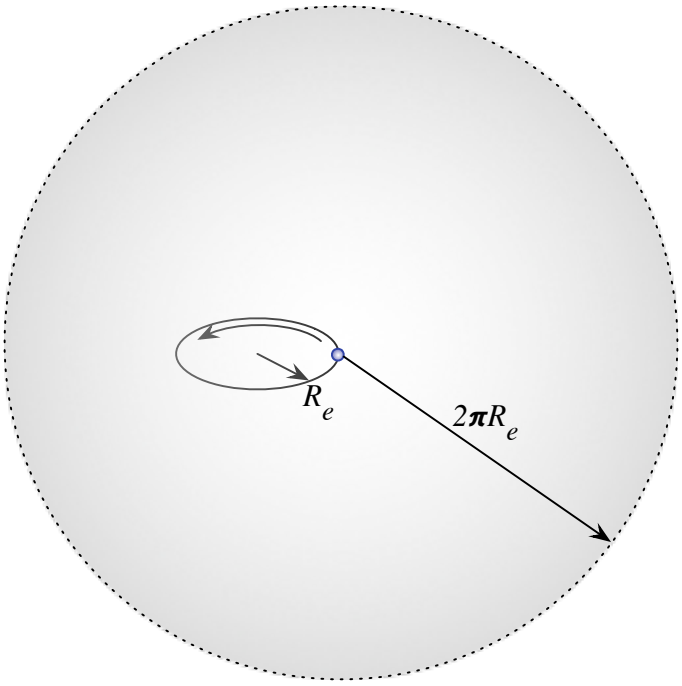

FIGURE 2.4.1. The spherical volume element within the reach of electromagnetic signals during one full Zitterbewegung circulation

Starting from the fundamentals, the $\boldsymbol{\partial}^2 \boldsymbol{A}_{\square} = 0$ Maxwell equation describes how electric and magnetic fields induce each other. As discussed in chapter 1, the electromagnetic energy density has symmetric contributions from the electric and magnetic fields. The electron mass is accounted by the electric and magnetic field energies, that induce each other.

But let us consider the circular Zitterbewegung of an electron, as illustrated in figure 2.4.1. During one Zitterbewegung cycle at circulation radius R_e, the induction is influenced by electromagnetic signals propagating at the speed of light from within a sphere of $2\pi R_e$ radius. The total electric field energy of the electron is:

$$W_e = \frac{1}{2} m_e c^2 \tag{2.4.2}$$

However, the electric field energy outside of a sphere of $2\pi R_e$ radius is:

$$W_{2\pi R} = \frac{e^2}{32\pi^2 \epsilon_0} \int_{2\pi R_e}^{\infty} \frac{1}{r^4} \cdot 4\pi r^2 dr = \frac{e^2}{8\pi\epsilon_0} \int_{2\pi R_e}^{\infty} \frac{1}{r^2} dr = -\frac{e^2}{8\pi\epsilon_0} \frac{1}{r}\bigg|_{2\pi R_e}^{\infty} = \frac{e^2}{8\pi\epsilon_0 2\pi R_e} \tag{2.4.3}$$

The above equation means that only a part of the total electric field could exert its magnetic-field-inducing effect during a Zitterbewegung rotation by 2π phase. The unaccounted ratio of electric field energy is:

$$\frac{W_{2\pi R}}{W_e} = \frac{e^2}{4\pi\epsilon_0 2\pi R_e m_e c^2} = \frac{r_{cl}}{2\pi R_e} \tag{2.4.4}$$

where we used the $r_{cl} = \frac{1}{4\pi\varepsilon_0} \frac{e^2}{m_e c^2}$ definition of the classical electron radius.

It follows from the above result that the ratio of single loop account electric field energy is $1 - \frac{W_{2\pi R}}{W_e} = 1 - \frac{r_{cl}}{2\pi R_e}$.

In order to calculate the correct magnetic dipole field strength, we must account the induction of the total electric field energy. Therefore, the anomalous magnetic moment is just the inverse of the single loop accounted electric field energy ratio:

$$g = \left(1 - \frac{r_{cl}}{2\pi R_e}\right)^{-1} \approx 1 + \frac{\alpha}{2\pi} \tag{2.4.5}$$

The approximation part in the above formula corresponds to the Schwinger factor. It can be observed from the above result that the correct $g = \left(1 - \frac{r_{cl}}{2\pi R_e}\right)^{-1}$ formula is just slightly different from the Schwinger factor when $\frac{r_{cl}}{R_e}$ is small, but becomes significantly different when r_{cl} and R_e are similar in size.

2.5. Conclusions

We showed that the magnetic flux quantization in h/e units is a universal property of the electron's spin circulation, atomic orbitals, and even relativistic orbitals. Essentially, the $A_{\parallel}$ and $A_{\perp}$vector potential components define two orthogonal circulations, and each circulation carries $\Phi_M = h/e$ magnetic flux. Therefore, we shall formulate our proton model with the use of h/e magnetic flux quantization, recognizing that it is a fundamental property of elementary particles and orbitals.

We derived the electron's anomalous magnetic moment from causality considerations. The presented derivation is much simpler than the calculation proposed by Schwinger. This calculation will be also used in a later chapter, in the neutron context.

Acknowledgements: The author thanks Giorgio Vassallo for some essential suggestions.

Bibliography

[1] D. Hestenes "Zitterbewegung structure in electrons and photons", arXiv:1910.11085 (2019)
[2] H. Jehle Relationship of flux quantization to charge quantization and the electromagnetic coupling constant, Physical Review D, Volume 3.2 (1971)
[3] W. Quint and M. Vogel "Magnetic Moment of the Bound Electron", chapter 3 in "Fundamental Physics in Particle Traps" (2014)

CHAPTER 3

A toroidal proton model that matches experimental data

Andras Kovacs[1]
[1] ExaFuse. E-mail: andras.kovacs@broadbit.com

ABSTRACT. Otto Stern's 1933 measurement of the unexpectedly large proton magnetic moment indicated to most physicists that the proton is not a point particle. At that time, many physicists modeled elementary particles as point particles, and therefore Stern's discovery initiated the speculation that the proton might be a composite particle. This speculation eventually led to the quark-based proton model, which we review in section 3.1. Surprisingly, we find that all major experiments contradict the quark-based proton model. This motivates us to develop a more realistic proton model. We require our model to naturally match experimental data and to respect all foundational Physics laws.

To make sense of the unexpectedly large proton magnetic moment data, one must firstly understand the theory of magnetic moment calculations, which we covered in chapters 1-2. In order to compare a proton model against experimental data, one must clarify how large the proton is; this is issue is explored in section 3.2.

We identify a simple proton structure that explains the origin of its principal parameters. Our model uses only relativistic and electromagnetic concepts, highlighting the primary role of the electromagnetic potentials and of the magnetic flux quantum $\Phi_M = {}^{h}/_{e}$. Unlike prior proton models, our methodology does not violate Maxwell's equation or Noether's theorem.

Considering that the proton has an anapole (toroidal) magnetic moment, we propose that the proton comprises an elementary charge that moves at the speed of light along a path that encloses a toroidal volume. Two distinct $\Phi_M = {}^{h}/_{e}$ magnetic flux quanta stabilize the proton's charge trajectory: these are poloidal and toroidal Zitterbewegung loops.

We calculate the radii of the toroidal and poloidal current loops, and the proton equivalent of the classical electron radius. We compare our calculations against experimental data, and find a surprisingly precise match.

3.1. Motivation

3.1.1. A brief history of the proton model. Before the 1970s, most scientists viewed the proton as an elementary particle. Starting from the 1970s, scientists working with high energy particle colliders proposed that protons and neutrons are not elementary particles, but comprise smaller sub-particles. According to their model, a proton and a neutron both comprise three quark sub-particles. The existence of quarks has been suggested initially in the 1960s, based on the theoretical efforts by Gell-Mann to model baryons and mesons [**3**], which were observed in a great variety during high energy nuclear experiments. The momentum distribution of particles emerging from a high-energy collision is characterized by the F_2 structure function[1]. Feynman's proposition was that the F_2 structure function probes the internal momentum distribution of sub-particles; for

[1]A detailed explanation of the $F_1(x)$ and $F_2(x)$ structure functions can be found for example in [**16**]. In these functions, the variable x measures the fraction of the nucleon's longitudinal momentum carried by the struck particle, evaluated in the Breit frame. The $F_1(x)$ function at a given x is interpreted as $\frac{1}{2}$ of the likelihood of scattering from a particle which, in the Breit frame, has longitudinal momentum fraction x of the proton. In case of scattering from spin-$\frac{1}{2}$ particles, $F_2(x) = 2xF_1(x)$.

a particle comprising N sub-particles, its F_2 structure function must peak at $x = \frac{1}{N}$. Gell-Mann's original quark theory thus required the F_2 momentum distribution to peak at $x = \frac{1}{3}$. However, as will be shown in section 3.1.3, this is not the case because the experimentally observed F_2 data peaks at $x = \frac{1}{9}$. Since the 1970s, this deviation from the required peak at $x = \frac{1}{3}$ was explained away via the hypothesis that the three quarks originally thought to form the proton are the so-called "valence quarks", which are swimming in the background of "sea quarks" [**4**]. These so-called sea quarks are a collection of quark-antiquark pairs, radiated by the three valence quarks. However, the calculations of 1970s still showed that the valence quarks together with the sea quarks only accounted for 54% of the proton's momentum [**2**]. A further hypothesis was added to supplement the momentum shortfall of the quarks; chargeless particles called gluons were introduced into the proton model [**5**]. Since gluons have no electric charge, the thinking was that they are there, but the electrons probing the proton in deep inelastic scattering cannot see them. These hypothesized gluons were assigned the missing proton momentum, and the resulting proton model became the quark-gluon model that it is today. Despite the absence of any direct quark observation, the quark-gluon model gained popularity during the 1970s, and remained embraced by most theoretical physicists ever since.

According to the 1970s model of "valence quarks" swimming in the background of "sea quarks and gluons", there seemed to be an angular momentum deficit with respect to the measured angular momentum of the proton, and therefore the presence of "virtual strange quarks" was also postulated during the 1990s [**7**].

In the context of quark theory, the fulfillment of $F_2(x) = 2xF_1(x)$ relation around $x = \frac{1}{3}$ implies that an individual quark's spin is detectable[2]. Since the proton's magnetic moment measurements yield a constant value of $\mu_p = 2.793\mu_N$, quark proponents postulated that the three valence quarks are always spin correlated and that the sea quarks' spin contribution always sums up to zero. The $\mu_p \approx 3\mu_N$ relation has been interpreted as the almost parallel orientation of the three valence quark spins. It was pointed out to pioneering quark proponents that their requirement might be in contradiction with the Pauli exclusion principle. This issue lead Oscar Greenberg to postulate in 1964 that quarks also have "color charge"; the purpose of this color charge hypothesis was to remove the perceived contradiction with respect to the Pauli exclusion principle.

3.1.2. Experimental counter-evidence to the quark model. Although the quark-based model was inspired by the great variety of mesons, the proposed quark masses do not add up the masses of observed mesons. According to quark proponents, this is explained by a negative binding energy between quarks: any particle's valence quarks masses are only a small percentage of the total particle mass, with the bulk of the particle mass coming from virtual particles which represent the binding force: i.e. virtual quarks and gluons. Moreover, the valence quark : virtual quark : gluon mass ratio is allowed to vary from particle to particle in order to match the observed masses. Now what is the physical meaning of negative binding energy? By definition, negative binding energy means a metastable bound state. This model implies that individual quarks should be easily observable upon the break-up of their metastable binding. However, quark proponents also postulated that these metastable bonds between quarks can never be dissociated. There is a fundamental contradiction between the hypothesis of metastable quark binding and the hypothesis of unbreakable quark bonds.

[2]The $F_2(x) = 2xF_1(x)$ equation is referred to as the Callan-Gross relation. Scattering experiments have indeed observed this Callan-Gross relation, at least within the $x = [0.25, 0.75]$ range.

Proton-antiproton reactions provide rather direct counter-evidence. Figure 3.1.1 shows traces of a proton-antiproton reaction event, highlighting the produced pion tracks. According to the quark model, a proton-antiproton pair comprises six quarks. After a partial annihilation of quark-antiquark pairs, there can be up to four remaining quarks, which may be organized into two pions. However, figure 3.1.1 shows at least eight pions emerging from the annihilation event, which contradicts the quark model. A quark model proponent may try to explain this phenomenon by assuming that the kinetic energy of the incoming antiproton was converted into the production of numerous pion-antipion pairs just prior to its annihilation. However, such an explanation is refuted by reference [**5**], whose authors exposed a nuclear emulsion to antiprotons, and then analyzed the resulting tracks in the emulsion. Their discussion of figure 2 in reference [**5**] clearly states that the antiproton first came to a rest in the emulsion, and then produced at least five pions upon annihilation with a proton. Such large number of pions emerging from proton-antiproton reactions is impossible under the quark-antiquark annihilation model.

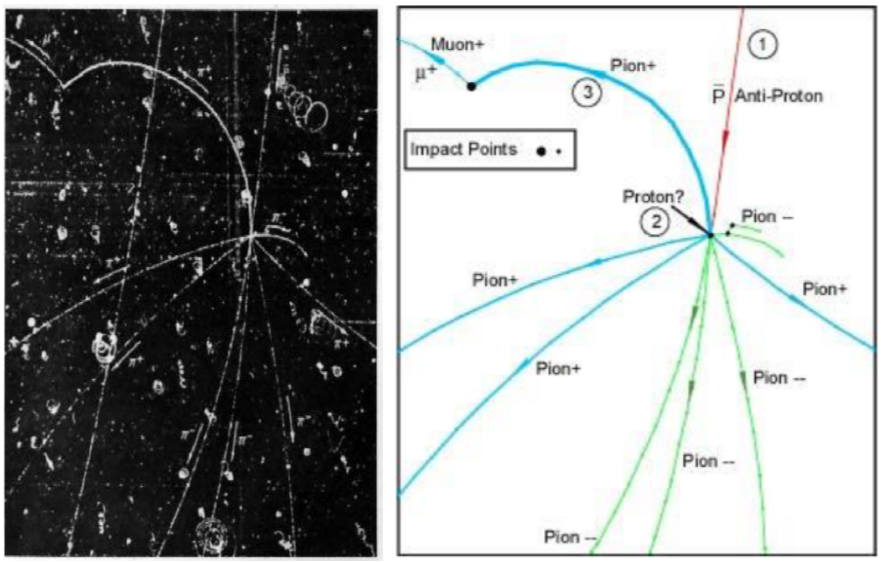

FIGURE 3.1.1. Proton-antiproton annihilation event. Left: bubble chamber photograph. Right: diagram of the photo, identifying the particles created by the annihilation event. Source: Lawrence Berkeley National Laboratory Science Photo Library - photograph K003/4377.

According to the quark model, the proton and neutron both comprise three quarks, only differing in one quark type. However, we shall establish in the following chapters that the neutron comprises a positive and a negative elementary charge, which again invalidates the quark-gluon model.

3.1.3. A re-interpretation of high-energy particle collision data. Considering the above outlined problems with the quark-based proton model, one may wonder about the origin of the F_2 momentum-distribution data recorded in high-energy collisions.

The production of particle-antiparticle pairs is a well established phenomenon of high-energy collisions. Therefore, an incoming energetic electron may produce muon-antimuon pairs upon scattering. Heavier pairs, such as a pion-antipion pair, soon decay into longer-lived muons and antimuons. Also, an incoming electron may be energized into a muon upon scattering. It is thus pertinent to consider a relationship between the F_2 data and the short-lived particles produced in scattering events.

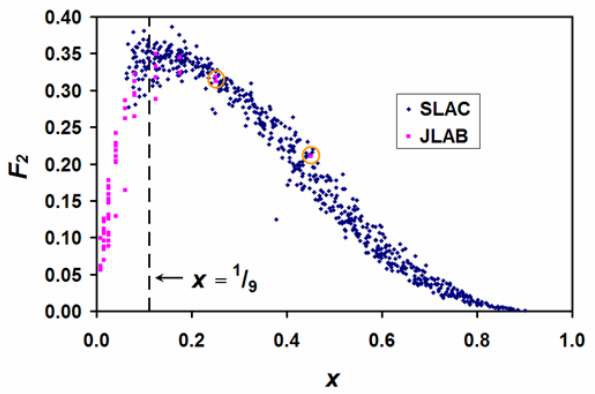

FIGURE 3.1.2. Combined SLAC and JLAB data of F_2 momentum distribution measurements from electron-proton scattering, reproduced from [**22**].

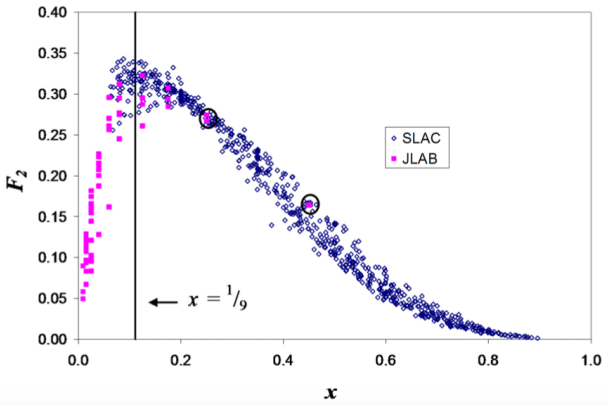

FIGURE 3.1.3. Combined SLAC and JLAB data of F_2 momentum distribution measurements from electron-deuteron scattering, reproduced from [**22**]. This scattering data shows the same F_2 momentum distribution as in the electron-proton case.

Reference [**22**] presents a thorough analysis of high energy scattering data from measurements performed at the Stanford Linear Accelerator Center (SLAC), Thomas Jefferson National Accelerator Facility (JLAB), and Hadron Electron Ring Accelerator (HERA). As shown in figures 3.1.2 and 3.1.3, the combined SLAC and JLAB data of F_2 momentum distribution measurements shows clearly, without any curve fittings, that their F_2 values peak in the vicinity of $x = \frac{1}{9}$. The JLAB F_2 values at $x = 0.45$ and $x = 0.25$ (circled) show that JLAB data integrates well with the original SLAC F_2 data. Is the use of single-variable $F_2(x)$ distribution justified, i.e. are the energy and momentum exchange sufficiently high for convergence? The use of $F_2(x)$ rather than $F_2(x, Q^2)$ is justified because the SLAC data was shown to satisfy Bjorken scaling, i.e. for x>0.2, the F_2 values are essentially the same for a given x regardless of the Q amount of energy transferred between the scattering particles. In this x>0.2 region, Q^2 values range from 0.6 to about 30 GeV^2. Regarding the x<0.2 region, the JLAB Q^2 values shown in Figure 3.1.4 are nearly the same as the SLAC Q^2 values listed in Appendix A.1 of [**22**], which makes the two results directly comparable.

One may wonder why this F_2 peak at $x = \frac{1}{9}$ doesn't show up in any other literature? By 1973, mainstream theorists have essentially embraced the quark-gluon model as adequately describing the structure of the proton. Most attempts to explain the SLAC

x	Q^2	F_2 - p	F_2 - d	x	Q^2	F_2 - p	F_2 - d
0.009	0.034	0.056	0.0492	0.04	0.287	0.2027	0.2002
0.009	0.051	0.0616	0.058	0.04	0.353	0.2244	0.2077
0.009	0.086	0.0997	0.0896	0.04	0.37	0.2288	0.2139
0.015	0.059	0.0696	0.0669	0.04	0.371	0.2186	0.2155
0.015	0.095	0.0842	0.0831	0.04	0.38	0.2102	0.2231
0.015	0.098	0.0961	0.0935	0.04	0.421	0.2416	0.2268
0.015	0.112	0.0876	0.0966	0.06	0.18	0.1641	0.1616
0.015	0.127	0.1058	0.1073	0.06	0.479	0.2622	0.2563
0.015	0.144	0.1114	0.1129	0.06	0.491	0.2617	0.2702
0.015	0.151	0.1216	0.1186	0.06	0.543	0.2751	0.2609
0.015	0.164	0.1253	0.1227	0.06	0.633	0.2863	0.2958
0.015	0.172	0.1118	0.1286	0.08	0.456	0.265	0.2451
0.025	0.067	0.0883	0.0834	0.08	0.617	0.2935	0.2752
0.025	0.092	0.096	0.0953	0.08	0.619	0.296	0.2767
0.025	0.104	0.104	0.0994	0.08	0.799	0.3128	0.295
0.025	0.113	0.1069	0.1024	0.08	0.818	0.3227	0.3122
0.025	0.14	0.1251	0.1208	0.125	0.588	0.2876	0.2609
0.025	0.186	0.1469	0.1441	0.125	0.797	0.3179	0.2873
0.025	0.195	0.1312	0.1439	0.125	1.032	0.3319	0.2952
0.025	0.212	0.1675	0.1545	0.125	1.056	0.3491	0.3228
0.025	0.222	0.1593	0.1568	0.175	1.029	0.3242	0.2846
0.025	0.24	0.178	0.1656	0.175	1.045	0.3235	0.2939
0.025	0.252	0.1696	0.1745	0.175	1.365	0.3447	0.3072
0.025	0.253	0.153	0.1601	0.25	1.332	0.3126	0.2673
0.025	0.287	0.1669	0.1814	0.25	1.761	0.3183	0.2744
0.04	0.133	0.1295	0.128	0.45	2.275	0.2104	0.1638
0.04	0.273	0.2038	0.1876				

FIGURE 3.1.4. F_2 structure function values for the proton (F_2 - p) and the deuteron (F_2 - d) as a function of x and Q^2 from the JLAB E99-118 deep inelastic scattering experiments [**23**].

scattering results any other way had ended, and the bulk of the theoretical effort focused on enhancing the quark model. Different versions of the quark-gluon plasma model predict either constant or rising F_2 values as $x \to 0$. In the 1990s, when HERA experiments began producing data in this x<0.1 range, it was assumed that HERA filled the low-x gap left by SLAC, even though its data was generated from scatterings with Q^2 values tens to hundreds of times higher than the SLAC data. Many theorists could not resist the temptation of mixing non-comparable data in this low-x region of the F_2 curve, and mistakenly proclaimed experimental support for their quark-gluon model. Reference [**21**] is a typical example of such erroneous data analysis. Around 2000, the JLAB experiment began producing scatterings with comparable Q^2 values to the SLAC experiment. By that time, the erroneous blending of high-Q^2 HERA data with low-Q^2 SLAC data was already a consensus procedure for obtaining the proton's F_2 curve, and mainstream theorists had no interest in pointing out their colleagues' mistakes or discussing the implications of the JLAB experiment.

Upon dividing the proton's mass by 9, we obtain approximately the muon mass. This match with the F_2 peak location at $x = \frac{1}{9}$ suggests that it may correspond to electron scattering from a muon or antimuon that was produced in some preceding scattering event. Our interpretation implies that one should also find a peak corresponding to electron-electron scattering in the very low-x region because an incoming electron may also collide with a previously scattered other electron. Upon the analysis of HERA experiments, reference [**22**] indeed identifies yet another F_2 momentum distribution peak near $x = \frac{1}{1836}$, which corresponds to the electron mass.

Since there is no F_2 peak at $x = \frac{1}{3}$, the fulfillment of Callan-Gross relation around $x = \frac{1}{3}$ simply means that the energetic electron is mainly scattering from the proton, which is a spin-$\frac{1}{2}$ particle.

In summary, the F_2 momentum distribution data shows signatures of electron-muon and electron-electron scattering. Consequently, the quark model is contradicted by all experimental data. The absence of a reasonable proton model motivates us to explore the proton's internal structure.

Antiprotons are generated in sufficiently energetic collisions between light and heavy nuclei. Would a violent collision create complex structures involving many sub-particles? That would be very unlikely; violent collisions do not decrease entropy by creating elaborate structures. Occam's razor principle favors that the emerging proton-antiprotion could be just a pair of elementary vortices. We thus investigate whether a relatively simple proton model exists, which would match its experimentally observed properties.

3.2. How large is the proton?

3.2.1. The "classical proton radius". Any particle's Compton scattering cross-section is given by the Klein-Nishina formula, where one parameter is the charge radius. Upon fitting the electron's experimental Compton scattering cross-section to the Klein-Nishina formula, in the 0.5 MeV photon energy range, one obtains 2.82 fm classical electron radius. This classical electron radius is also given by the $r_{cl} = \frac{1}{4\pi\varepsilon_0}\frac{e^2}{m_e c^2}$ formula.

Is the same method applicable for determining the analogous "classical proton radius", given by the $r_{cl} = \frac{1}{4\pi\varepsilon_0}\frac{e^2}{m_p c^2}$ formula? Figure 3.2.1 shows the proton's scattering cross-section in the 1 GeV photon energy range, which corresponds to the proton mass. There are numerous peaks in the scattering data of figure 3.2.1; these correspond to photo-production of new particles. Experimental measurements determined that the largest peak around 300 MeV corresponds to the photo-production of neutral pions, while the peak around 700 MeV corresponds to the photo-production of a pion and an η meson. In contrast to the electron case, the scattering cross-section is now a sum of particle photo-production and Compton scattering processes. Nevertheless, we can make an estimation of the "classical proton radius".

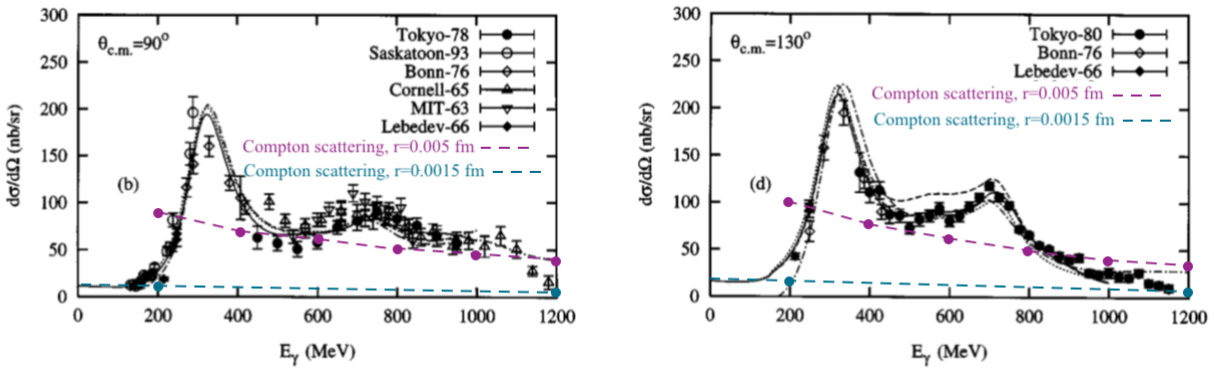

FIGURE 3.2.1. The proton's interaction cross-section with high frequency radiation, reproduced from [**20**]. The horizontal scale shows the incoming photon energy, the left and right panels show the cross-section at 90° and 130° scattering angles, respectively. The red and and blue dashed lines show the Compton scattering cross-section for the indicated charge radius values.

The dashed lines on figure 3.2.1 show the Compton scattering cross-section at $5 \cdot 10^{-18}$ m and at $1.5 \cdot 10^{-18}$ m "classical proton radius" values. With $5 \cdot 10^{-18}$ m radius, the Compton scattering cross-section becomes larger than the experimental values in the $<$200 MeV and $>$1000 MeV regions. Therefore, the true radius is smaller than $5 \cdot 10^{-18}$ m. In contrast, with $1.5 \cdot 10^{-18}$ m radius value the Compton scattering cross-section converges to the experimental values both in the $<$200 MeV and $>$1000 MeV regions. Therefore, light scattering measurements indicate that the "classical proton radius" is approximately $1.5 \cdot 10^{-18}$ m.

3.2.2. The proton's apparent Zitterbewegung radius. Numerous experiments aim to precisely measure the proton's so-called "charge radius", which is defined as the mean radius value of its charge distribution. High-energy electron-proton scattering experiments are one class of such measurements.

As shown in table 1, one of the earliest scattering analysis based proton charge radius extraction was published in 1963: it comprises a systematic review of scattering experiments performed up to that date, and its authors calculated a $0.805 \cdot 10^{-15}$ m charge radius value. By the early 2000s, the consensus mean proton radius value increased to $0.875 \cdot 10^{-15}$ m, but reference [**19**] re-analyzes the involved measurements and claims to have found a systemic error which caused over-estimations.

Recent measurements converge around the $0.84 \cdot 10^{-15}$ m mean radius value, and claim very small error margins of only $(5 - 8) \cdot 10^{-18}$ m.

This $0.84 \cdot 10^{-15}$ m mean radius value is several orders of magnitude larger than the above identified $r_{cp} < 5 \cdot 10^{-18}$ m parameter. To understand the physical meaning of the $0.84 \cdot 10^{-15}$ m radius value, we use electron analogy. When an electron interacts with high frequency light, its scattering cross section is given by the Klein-Nishina formula, and such scattering data reveals the electron's 2.82 fm spherical charge radius. The electron's much larger Zitterbewegung radius was shown to be 386 fm in chapter 1. In the scientific literature, this electron Zitterbewegung radius is also referred to as the electron's "reduced Compton radius". By analogy, we associate the proton's $0.84 \cdot 10^{-15}$ m radius value as an approximation of the major radius of the torus enclosed by the proton charge trajectory.

Publication year	Mean proton radius value	Reference
1963	0.805 ± 0.011 fm	[**13**]
2016	0.840 ± 0.016 fm	[**10**]
2020	0.831 ± 0.019 fm	[**27**]
2021	0.847 ± 0.008 fm	[**7**]
2022	0.840 ± 0.005 fm	[**19**]

TABLE 1. Electron-proton scattering analysis based mean proton radius measurements.

Besides the electron-proton scattering analysis, there are also spectroscopic methods for the proton's charge radius calculation [**11**]; all spectroscopic estimate the impact of non-zero proton radius on the electrostatic potential of the electron's wavefunction. Table 2 shows the results of recent proton radius measurements, based on spectroscopic methods.

Publication year	Involved particles	Charge radius	Reference
2017	e^-, p^+	0.8335 ± 0.0095 fm	[**2**]
2019	e^-, p^+	0.833 ± 0.01 fm	[**3**]
2020	e^-, p^+	0.8483 ± 0.0038 fm	[**11**]

TABLE 2. Spectroscopic analysis based mean proton radius measurements.

Tables 1 and 2 show remarkably similar values. Omitting the 1963 data, the remaining recent measurements average out to $r_{mean} = 0.839 \pm 0.007$ fm.

3.2.3. Charge density measurements. With the advancement of electron-proton scattering measurements, it has become possible to directly map out the proton's radial charge distribution. Such radial charge distribution data is measured for example at

JLAB [**6**], and is visualized in figure 3.2.2. This distribution's average RMS (Root Mean Square) value is 0.8 fm, which implies only 4% deviation from the data of tables 1 and 2. Figure 3.2.2 conveys the important information that the proton charge is located mainly within 0.2-1.4 fm from its center. Any realistic proton model must yield a similar radial distribution range.

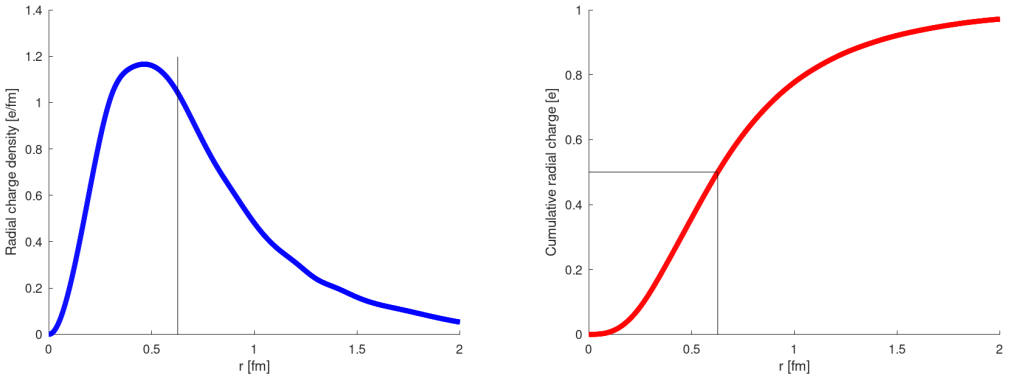

FIGURE 3.2.2. The proton's radial charge distribution, according to JLAB measurements [**6**]. Left: the proton's radial charge density. Right: the cumulative proton charge contained within a given radius. In both charts, the black vertical line indicates the radius which contains 50% of the total charge.

3.2.4. The proton's electric polarizability radius. Electric polarizability measurements represent yet another proton size measurement method. Recent measurements by this method are reported in references [**18, 8**]: their authors obtain $1.2-1.3$ fm proton size. This size is significantly larger than the above-mentioned proton size measurements, and the origin of such discrepancy has not been understood in preceding works.

As can be seen in figure 3.2.2, nearly all of the proton charge is contained within this $1.2-1.3$ fm radius. It is therefore reasonable to consider whether electric polarizability measurements indicate the true outer limit of the proton charge distribution.

3.3. Methodology

In this work, we explore an electromagnetic proton structure which is in accordance with Maxwell's equation. The preceding chapters outlined our methodology.

As shown in table 3, our methodology is in accordance with all fundamental physical laws. In comparison, the quark-based methodology has multiple drawbacks: i) the quark model violates foundational laws, such as Maxwell's equation or Noether's theorem, ii) as explained in section 3.1, the quark model lacks any experimental evidence, and iii) the quark model is contradicted by the commercial Nuclear Magnetic Resonance (NMR) technology. The implications of proton NMR data will be discussed in chapter 4.

At first it seems natural to use the exact same model for describing both the electron and proton, scaling the given particle's dimensions by the appropriate particle mass. The advantages of a simple ring-shaped proton model were indeed pointed out by David L. Bergman in his paper "The Real Proton" [**1**]. This approach, while works well for muons, introduces unacceptably large errors if naively used for proton modeling. Let us refer to such a circular Zitterbewegung proton model as the "scaled positron model". The

[3]The quark-based model assigns over 98% of the proton mass to virtual particles.

	Quark-based proton model	**This work**
Violates Maxwell's equation?	Yes (point-like charges)	No
Neglects infinite quantities?	Yes (renormalization)	No
Violates Noether's theorem?	Yes (virtual particles)[3]	No
Relation to NMR measurements?	Contradicts p^+ NMR data	Explains p^+ NMR
Radius calculations can be verified?	No (too lengthy/complex)	Yes

TABLE 3. A comparison between the quark-based proton model and our present work.

magnetic moment of this scaled positron model is the so-called "nuclear magneton" value μ_N, given by the $\mu_N = \frac{e\hbar}{2m_p}$ formula.

It follows from the $r^{-1} = m$ relation of section 1.2 that Zitterbewegung radius of a scaled positron is:

$$r_{scaled} = r_e \frac{m_e}{m_p}$$

where m_e is the electron mass and m_p is the proton mass.

Using the above equation with the r_e=386.16 fm electron Zitterbewegung radius, which is the reduced Compton radius, we obtain r_{scaled}=0.2103 fm. This value will be used for comparison against the real proton Zitterbewegung radius.

While the magnetic moment of a scaled positron model is equal to the nuclear magneton value μ_N, the experimental proton magnetic moment value is approximately 2.79 times larger. Secondly, as discussed in section 3.2.2, the proton's experimental Zitterbewegung radius value is 0.839 ± 0.007 fm, while the "scaled positron" model yields a 0.2103 fm Zitterbewegung radius from the $e^+ : p^+$ mass ratio. The following sections present a simple proton model that overcomes these large discrepancies while fully maintaining the previously introduced conceptual framework.

3.4. Proton geometric structure

3.4.1. Zitterbewegung topology. We develop a proton model according to the above considerations, employing gaugeless electrodynamics. While the natural choice for a proton model is a simple "scaled positron" model, it leads to some unacceptable discrepancies with the experimental data, that we have already pointed out.

Measurements of the proton's anapole magnetic moment have been claimed since 1997 [**26**]. In such experiments, electron-proton coupling interactions are used for mapping out the proton's various magnetic modes. Since the anapole magnetic moment is generated by a toroidal charge current, these experiments suggest that the proton's charge circulates over a toroidal surface.

We therefore consider a model where the stationary proton charge follows a toroidal Zitterbewegung trajectory, similar to a toroidal coil winding. The toroidal volume enclosed by the proton charge trajectory has a minor (poloidal) proton radius r_{pp} and a major (toroidal) proton radius r_{pt}, which remain to be determined.

A toroidally shaped Zitterbewegung comprises two Zitterbewegung loops, corresponding to the poloidal and toroidal directions. Such a topology is illustrated in figure 3.4.1. According to chapter 2 results, these loops must correspond to two distinct h/e magnetic flux quanta, representing the poloidal and toroidal directions. This scenario is

geometrically analogous to the two distinct h/e magnetic flux quanta of a bound electron, corresponding to its circular Zitterbewegung and orbital current[4].

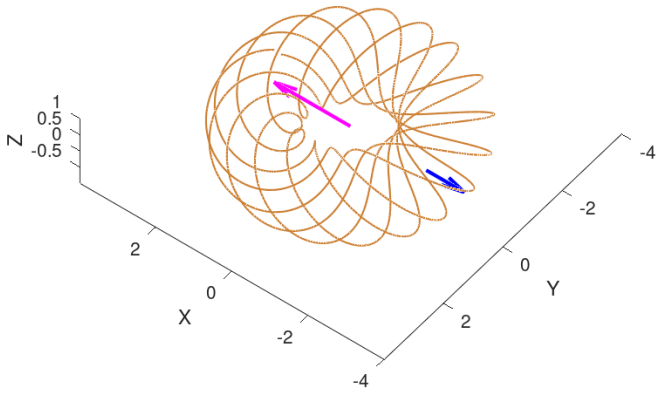

FIGURE 3.4.1. An illustration of this model's toroidal proton geometry. The brown curve is the Zitterbewegung trajectory, the blue arrow represents the poloidal proton radius (r_{pp}), and the purple arrow represents the toroidal proton radius (r_{pt}). The X, Y, Z units are multiples of r_{pp}.

3.4.2. Poloidal and toroidal magnetic flux loops. At the Compton radius scale, the magnetic flux quantum h/e induces a centripetal magnetic force that constrains the positive elementary charge to follow a circular Zitterbewegung path. This h/e magnetic flux quantization was derived in chapter 2. There are two Zitterbewegung loops: a poloidal and a toroidal one. As both loops are generated by the same elementary charge, each loop must have h/e magnetic flux.

In the following, we apply the above introduced methodology to a toroidal proton model. Firstly, we calculate the "classical proton radius", and then we calculate its poloidal and toroidal radii. Section 3.5.3 takes the proton mass and magnetic moment as input parameters and directly applies the h/e magnetic flux quantization condition.

3.5. The calculation of proton parameters

3.5.1. The "classical proton radius" calculation. We calculate the "classical proton radius" analogously to the electron case:

$$r_{cp} = \frac{1}{4\pi\varepsilon_0}\frac{e^2}{m_p c^2} \simeq 1.534698267 \cdot 10^{-18}\, m$$

This calculated r_{cp} value is remarkably similar to the experimental value discussed in section 3.2.1.

As in the electron case, electromagnetic induction implies that the proton mass comprises equal amounts of electric and magnetic field energy:

$$W_e = W_m = \frac{m_p}{2}$$

[4]These considerations mark the main difference between the present work and the preceding proton model of reference [**25**].

3.5.2. The proton's poloidal and toroidal Zitterbewegung speed. Referring to figure 3.4.1, the proton's total magnetic field energy is shared between two Zitterbewegung loops, and therefore each loop's magnetic field now carries less than half of the particle mass. Therefore, the r_{pp} and r_{pt} proton radius values must be larger than the above calculated r_{scaled}=0.2103 fm radius.

To transform the circular Zitterbewegung model of the positron into a toroidal geometry, the naive approach is to view the positron from rotating reference frame. Such reference frame transformation must take into account the relativistic Thomas precession effect which arises in a rotating reference frame. This effect reduces the apparent lab-frame speed of a circularly orbiting object in proportion to its Lorentz boost factor:

$$\beta_{lab} = \frac{\beta'}{\gamma_{lab}}$$

where $c\beta'$ is the true rotation speed of the instantaneous rest frame, $c\beta_{lab}$ is the apparent rotation speed in the lab frame, and $\gamma_{lab} = \sqrt{1-\beta_{lab}^2}^{-1}$. When $\beta_{lab} = \frac{1}{\sqrt{2}}$, we get $\beta' = 1$: this limiting value corresponds to the true rotation speed being the speed of light. This result means that in the $\beta_{lab} < \frac{1}{\sqrt{2}}$ regime the toroidal charge distribution is in fact a rotating scaled positron because we can make a rotational change of reference frame which transforms the charge current back to the positron's ring shaped Zitterbewegung. Therefore, the $\beta_{lab} < \frac{1}{\sqrt{2}}$ regime corresponds to a rotating lepton model: such a rotating lepton would eventually transition into a non-rotating ground state.

On the other hand, the limiting $\beta_{lab} = \frac{1}{\sqrt{2}}$ value stays invariant under any rotational reference frame transformation, and therefore it implies a truly toroidal Zitterbewegung current, which retains the same geometry in any reference frame. Since the proton must retain its basic properties in all reference frames, this $\beta_{lab} = \frac{1}{\sqrt{2}}$ value defines its toroidal Zitterbewegung speed: $v_t = \frac{c}{\sqrt{2}}$. The corresponding $\beta' = 1$ value is indeed the property of light-speed Zitterbewegung.

It follows from Maxwell's equation that electromagnetic waves propagate at the speed of light, implying that the spherical charge's Zitterbewegung speed is always the speed of light [**15**]. In the toroidal geometry, the Zitterbewegung speed vector comprises toroidal and poloidal components, which are perpendicular to each other:

$$v_t^2 + v_p^2 = c^2$$

Since we already know the toroidal Zitterbewegung speed, we obtain: $v_p = v_t = \frac{c}{\sqrt{2}}$.

3.5.3. Proton size calculation from magnetic mass considerations. How is the proton's W_m =469.136 MeV magnetic field energy divided between its toroidal and poloidal current loops? The proton's magnetic moment measurement is in fact its toroidal magnetic moment measurement. For an elementary particle, its measured magnetic moment is given by the $\mu = \frac{e\hbar}{2m}$ formula, where the only non-constant factor is the particle mass. Since the proton mass is derived from electromagnetic induction, its excess toroidal magnetic moment is inversely proportional to its toroidal magnetic mass. Therefore the proton's toroidal magnetic energy is:

$$W_{mt} = W_m / \left(\frac{\mu_p}{\mu_N}\right) = \frac{469.136}{2.79285}\ \text{MeV} = 167.978\ \text{MeV}$$

The remaining poloidal magnetic field energy is:

$$W_{mp} = W_m - W_{mt} = 301.158\ \text{MeV}$$

Under the toroidal proton geometry there are two Zitterbewegung loops: a toroidal loop and a poloidal loop. Since both current loops are generated by the elementary charge e, the h/e magnetic flux quantization holds for each current loop. Thus we can calculate the magnetic energy values by applying the $\phi_t = h/e$ and $\phi_p = h/e$ magnetic flux quantization conditions:

$$W_{mt} = \frac{1}{2}\phi_t I_t = \frac{1}{2} \cdot 2\pi \frac{\hbar}{e} \cdot \frac{e v_t}{2\pi r_{pt}} = \frac{\hbar v_t}{2 r_{pt}}$$

$$W_{mp} = \frac{1}{2}\phi_p I_p = \frac{1}{2} \cdot 2\pi \frac{\hbar}{e} \cdot \frac{e v_p}{2\pi r_{pp}} = \frac{\hbar v_p}{2 r_{pp}}$$

We derived in section 3.5.2 the $v_p = v_t = \frac{c}{\sqrt{2}}$ values of the poloidal and toroidal Zitterbewegung speed. We may thus evaluate the toroidal and poloidal Zitterbewegung radii from the above equations:

$$r_{pt} = \frac{\hbar v_t}{2 W_{mt}} = 0.831 \text{ fm}$$

$$r_{pp} = \frac{\hbar v_p}{2 W_{mp}} = 0.463 \text{ fm}$$

The obtained 0.831 fm toroidal radius value is compatible with the experimentally measured $r_{mean} = 0.839 \pm 0.007$ fm proton charge radius value.

To further validate the consistency of our model, we check that the $\mu_p = I_t \pi r_{pt}^2$ magnetic moment formula is fulfilled for the toroidal current loop. The above-discussed scaled positron model corresponds to the nuclear magneton:

$$\mu_N = I \pi r_{scaled}^2 = \frac{ec}{2\pi r_{scaled}} \pi r_{scaled}^2 = \frac{ec}{2} r_{scaled}$$

where r_{scaled}=0.2103 fm is the scaled positron's Zitterbewegung radius. We now evaluate the proton's magnetic moment according to the current loop formula:

$$\mu_p = I_t \pi r_{pt}^2 = \frac{e\left(c/\sqrt{2}\right)}{2\pi r_{pt}} \pi r_{pt}^2 = \frac{ec}{2\sqrt{2}} r_{pt}$$

$$\mu_p/\mu_N = \left(c r_{pt}/\sqrt{2}\right) / \left(c r_{scaled}\right) = \frac{1}{\sqrt{2}} \frac{0.831}{0.2103} = 2.794$$

which precisely matches with the experimental μ_p/μ_N ratio. Comparing the above magnetic moment equation with the magnetic energy based r_{pt} calculation, one arrives at the same $\mu_p/\mu_N = r_{pt}/\left(\sqrt{2} r_{scaled}\right)$ formulation in either case: i.e. these are two ways of expressing the same physics.

3.5.4. The outer radius of the proton charge distribution. The toroidal proton geometry implies that the circulating proton charge is radially distributed between $r_{pt} - r_{pp} - r_{cp}$ and $r_{pt} + r_{pp} + r_{cp}$ distance from its center, i.e. its charge reaches up to r_{max}=1.3 fm radial distance. This 1.3 fm radius precisely matches the electric polarizability measurements based radius value, that was introduced in section 3.2.4. Indeed, it is logical to interpret the electric polarizability based radius as the proton charge's furthest distance from its center because one can polarize a charge distribution only within that range where it is physically present.

This r_{max} value is also matching the experimental data shown in figure 3.2.2, which demonstrates that the proton charge is distributed mainly within 1.2-1.4 fm radial distance. As discussed in section 3.2.3, this distribution's RMS distance is 0.8 fm, which is close to the calculated r_{pt} distance.

3.6. Proton-neutron interaction

3.6.1. The proposed electromagnetic model based interpretation of the proton-neutron reaction. In this section, we take a look at the simplest nuclear interaction: the $p^+ + n \rightarrow {}^2H^+$ reaction. It has been experimentally measured that a proton-neutron reaction is accompanied by the emission of a single-frequency electromagnetic wave at $f = 5.378 \cdot 10^{20}$ Hz frequency. This electromagnetic wave carries away 2.224 MeV energy; this energy exactly corresponds to the mass difference between a ${}^2H$ nucleus and the $p + n$ nuclei. A measurement of the proton-neutron interaction's single-frequency electromagnetic emission is shown in figure 3.6.1.

It follows from our proton model that the neutron comprises a proton and a negative elementary charge.

In chemistry, it is well-known that the $p^+ + H \rightarrow H_2^+$ chemical reaction involves the quantum mechanical state change of a single electron, and this electron radiates away a small fraction of the three particle masses. Analogously, the quantum mechanical state change of a nuclear negative charge radiates away a small fraction of the three particle masses. The toroidal proton geometry is thus stable not only for the 938.272 MeV free particle mass value, but also for a range of lower masses.

Any quantum mechanical state change emits a single-frequency electromagnetic wave, that radiates away $\triangle E = hf$ energy, where f is the wave frequency and h is the Planck constant. This $\triangle E = hf$ relation is exactly fulfilled during the $p^+ + n \rightarrow {}^2H^+$ reaction. The proton-neutron interaction may be thought of as a quantum mechanical state change of a single nuclear electron particle.

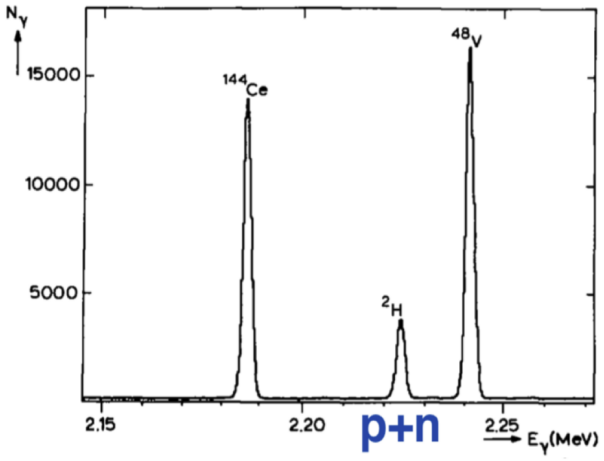

FIGURE 3.6.1. The simplest nuclear reaction: a proton approaches a neutron, causing radiation emission at 2.224 MeV photon frequency. The gamma spectrum measurement is reproduced from reference [**24**]; the ^{144}Ce and ^{48}V peaks are present for calibration purpose.

The proton and neutron do not have any electric quadrupole moments. The resulting ${}^2H^+$ nucleus has however an electric quadrupole moment of $+2.86$ mb. This positive quadrupole moment value indicates a negative charge distribution between the two protons, i.e. the negative nuclear charge may be an electron-like particle.

3.6.2. The quark model based interpretation of the proton-neutron reaction. The quark-based proton model describes the $p^+ + n \rightarrow {}^2H^+$ reaction as an interaction among six valence quarks and an undefined number of virtual quarks. This

interaction is supposedly mediated by a "spill-over" of the same attractive force that acts between any two quarks.

The mass defect of the $p^+ + n \rightarrow {}^2H^+$ reaction is three times smaller than the mass defect of the ${}^2H^+ + n \rightarrow {}^3 H^+$ reaction. In the quark model context, this indicates a larger spill-over of the attractive force for the ${}^2H^+ + n \rightarrow {}^3H^+$ reaction. As there is no Coulomb repulsion in either of these nuclear reactions, the quark model predicts a larger reaction probability for the ${}^2H^+ + n \rightarrow {}^3 H^+$ reaction. This prediction is contradicted by experiment; the ${}^2H^+ + n \rightarrow {}^3H^+$ reaction rate is around 1000 times smaller than the $p^+ + n \rightarrow {}^2H^+$ reaction rate. This contradiction signals yet another fundamental incompatibility between the quark model and experiments.

According to Maxwell's equation, a single-frequency wave emission implies that all involved quarks must oscillate at the same frequency during the reaction. It means that the proton's and neutron's hypothetical quarks must remain in a coherent state, i.e. in the same quantum mechanical state. But if these hypothetical quarks remain in the same quantum mechanical state, achieving a charge polarization that corresponds to the +2.86 mb electric quadrupole moment is impossible. This contradiction again signals a fundamental incompatibility between the quark model and experiments.

3.7. Conclusions

We have presented a proton model that describes the physical origin of numerous proton parameters, such as its mass, spin, charge radius, dipole magnetic moment, and anapole magnetic moment. The proton's elementary charge has a Zitterbewegung current over a toroidal surface. We calculated the proton's classical charge radius, poloidal radius, and toroidal radius, using only the proton mass and magnetic moment as input values. Despite our model's simplicity, our calculations are in very good agreement with experimental values.

A consistent application of Maxwell's equation lead to the discovery of the proposed proton model. The strong similarities with the electron model suggest a universal applicability of fundamental physical laws. Both the electron and the proton comprise an electromagnetic wave, whose formulation can be derived by solving Maxwell's equation. These solutions must not neglect the effects of general relativity, as demonstrated in our present work. Our proton mass calculation demonstrates that Maxwell's equation remains valid at least down to 10^{-18} m.

Based on our results, the proton may regain its elementary particle status. The main difference between an electron and a proton is the topology of their Zitterbewegung: a circular Zitterbewegung current in the electron case and a toroidal Zitterbewegung current in the proton case. While in the electron case a longitudinal electromagnetic wave circulates within the entire toroidal electron volume illustrated in figure 1.1.1, in the proton case a longitudinal electromagnetic wave circulates along the toroidal surface illustrated in figure 3.4.1. Along this toroidal proton structure, the longitudinal electromagnetic wave is found within a thickness of $2r_{cp} \approx 3 \cdot 10^{-18}$ m. It remains to be understood why only these two topologies lead to a stable particle in free space.

Acknowledgements: The author thanks William Stubbs for insightful discussions of high-energy electron-proton scattering data, and thanks Giorgio Vassallo for suggesting the proton's toroidal shape.

Appendix 1: Physical constants in Natural Units

Conversion constants for natural units.

$1.9732898 \cdot 10^{-7}\ m \simeq 1eV^{-1}$ length

$6.5821220 \cdot 10^{-16}\ s \simeq 1eV^{-1}$ time

$2.99792458 \cdot 10^{8}\ ms^{-1} = 1$ speed
$1.5192669 \cdot 10^{15}\ Hz \simeq 1eV$ frequency
$8.1193997 \cdot 10^{-13}\ N \simeq 1eV^2$ force
$1.8755460 \cdot 10^{-18}\ C = 1$ charge

Relevant physical constants in natural units:

$h = 2\pi$ Planck's constant $\left(6.62607015 \cdot 10^{-34} JHz^{-1}\right)$
$\hbar = {}^{h}/_{2\pi} = 1$ reduced Planck's constant
$\varepsilon_0 = \frac{1}{4\pi}$ vacuum permittivity
$\mu_0 = 4\pi$ vacuum magnetic permeability
$c = 1$ light speed in vacuum $\left(2.99792458 \cdot 10^{8} ms^{-1}\right)$
$\alpha^{-1} \simeq 137.036$ inverse of the fine structure constant
$e = \pm\sqrt{\alpha} \simeq 0.085424546$ $\left(1.602176634 \cdot 10^{-19} C\right)$ elementary charge
$\mu_N \simeq 4.552225759 \cdot 10^{-11}\ eV^{-1}$ $\left(5.0507837461 \cdot 10^{-27} JT^{-1}\right)$ nuclear magneton
$\mu_p \simeq 1.271367397 \cdot 10^{-10}\ eV^{-1}$ $\left(1.41060679736 \cdot 10^{-26} JT^{-1}\right)$ proton magnetic moment
$\frac{\mu_p}{\mu_N} \simeq 2.79284734463$ CODATA proton magnetic moment to nuclear magneton ratio
$m_p \simeq 0.93827208816 \cdot 10^{9}\ eV$ proton mass
$\lambda_p \simeq 6.696549362 \cdot 10^{-9}\ eV^{-1}$ $\left(1.32140985539 \cdot 10^{-15} m\right)$ proton Compton wavelength
$A_e \simeq 5.981875085 \cdot 10^{6} eV$ norm of the vector potential of the electron charge
$V_e = A_e$ electric potential at surface of the electron's charge
$\Phi_M = \frac{\hbar}{e} = 2\pi\alpha^{-1/2} \simeq 73.55246020$ elementary charge's magnetic flux
$m_e = \omega_e \simeq 0.51099895 \cdot 10^{6} eV$ electron rest mass
$\omega_e = m_e$ electron's charge angular speed
$T_e = \frac{2\pi}{\omega_e}$ electron Zitterbewegung period
$r_e = \omega_e^{-1} \simeq 1.956951198 \cdot 10^{-6} eV^{-1}$ $\left(0.3861592676 \cdot 10^{-12} m\right)$ electron Zitterbewegung radius
$r_{ce} = \alpha r_e$ classical electron radius
$R_{p,exp} \simeq 4.264 \cdot 10^{-9}\ eV^{-1}$ $\left(0.8414 \cdot 10^{-15} m\right)$ "proton charge radius" CODATA value

Appendix 2: Proton model parameters

$r_{pp} \simeq 0.463 \cdot 10^{-15} m$ proton torus minor (poloidal) radius
$r_{pt} \simeq 0.831 \cdot 10^{-15} m$ proton torus major (toroidal) radius
$r_{cp} \simeq 1.534698267 \cdot 10^{-18} m$ classical proton radius
$\eta = \frac{r_{pt}}{r_{pp}} \simeq 1.8$ proton torus aspect ratio
$v_{pt} = \frac{c}{\sqrt{2}}$ the toroidal component of the charge speed c
$\mu_p \simeq 2.793 \mu_N$ toroidal proton magnetic moment
$L_p = \boldsymbol{r}_{pt} \times \left(\frac{\mu_N}{\mu_p} m_p\right) \boldsymbol{v}_{pt} = \hbar$ the proton's toroidal angular momentum, calculated from its toroidal magnetic energy
$\hbar \cos(\vartheta) = \pm {}^{1}/_{2}\hbar$ $(\vartheta \in \{{}^{\pi}/_{3}, {}^{2\pi}/_{3}\})$ measured proton spin, see chapter 4
$\Phi_{pt} = \Phi_{pp} = {}^{h}/_{e} \simeq 73.55246020$ proton model magnetic flux quanta in natural units

Bibliography

[1] D. Bergman, *The real proton*, Foundations of Science, 3 (2000).

[2] A. Beyer, *The rydberg constant and proton size from atomic hydrogen*, Science, 358 (2017).

[3] N. Bezginov, *A measurement of the atomic hydrogen lamb shift and the proton charge radius*, Science, 365 (2019).

[4] J. D. Bjorken, *Inelastic electron-proton and gamma-proton scattering and the structure of the nucleon*, Physical Review, 185 (1969).

[5] O. Chamberlain, *Example of an antiproton-nucleon annihilation*, Physical Review, 102 (1956).

[6] T. D. N. S. A. Committee, *The frontiers of nuclear science - a long range plan*, (2007).

[7] Z. F. Cui, *Fresh extraction of the proton charge radius from electron scattering*, Physical Review Letters, 127 (2021).

[8] H. Fonvieille, *Virtual compton scattering and nucleon generalized polarizabilities*, Progress in Particle and Nuclear Physics, 113 (2020).

[9] M. Gell-Mann, *A schematic model of baryons and mesons*, Physics Letters, 8 (1964).

[10] K. Griffioen, C. Carlson, and S. Maddox, *Consistency of electron scattering data with a small proton radius*, Physical Review C, 93 (2016).

[11] A. Grinin, *Two-photon frequency comb spectroscopy of atomic hydrogen*, Science, 370 (2020).

[12] F. Halzen, *Quarks and leptons: An introductory course in modern particle physics*, John Wiley and Sons, (1984).

[13] L. N. Hand, *Electric and magnetic form factors of the nucleons*, Reviews of Modern Physics, 35 (1963).

[14] R. L. Jaffe, *Where does the proton really get its spin?*, Physics Today, (1995).

[15] A. Kovacs, G. Vassallo, P. O'Hara, F. Celani, and A. Di Tommaso, *Unified Field Theory and Occam's Razor*, World Scientific, 04 2022.

[16] S. E. Kuhn, *Nucleon structure functions: Experiments and models*, Proceedings of the 12th Annual HUGS at CEBAF, 231 (1998).

[17] J. Kuti, *Inelastic lepton-nucleon scattering and lepton pair production in the relativistic quark-parton model*, Physical Review D, 4 (1971).

[18] R. Li, *Measured proton electromagnetic structure deviates from theoretical predictions*, Nature, 611 (2022).

[19] Y. H. Lin, *New insights into the nucleon's electromagnetic structure*, Physical Review Letters, 128 (2022).

[20] A. I. L'vov and V. A. Petrun'kin, *Dispersion theory of proton compton scattering in the first and second resonance regions*, Physical Review C, 55 (1997).

[21] E. Perez, *The quark and gluon structure of the proton*, Reports on Progress in Physics, 76 (2013).

[22] W. L. Stubbs, *The nucleus of atoms: One interpretation*, CreateSpace Independent Publishing Platform, (2018).

[23] V. Tvaskis, *Proton and deuteron f2 structure function at low q2*, Physical Review C, 81 (2010).

[24] C. van der Leun, *The deuteron binding energy*, Nuclear Physics A, 380 (1982).

[25] G. Vassallo and A. Kovacs, *The proton and occam's razor*, Proceedings of the 2022 International Association for Relativistic Dynamics (IARD) conference, Journal of Physics - Conference Series, (2023).

[26] C. S. Wood, *Measurement of parity nonconservation and an anapole moment in cesium*, Science, 275 (1997).

[27] W. Xiong, *A high precision measurement of the proton charge radius at jlab*, PhD dissertation, Duke University, (2020).

CHAPTER 4

Proton spin and gyromagnetic factor

Andras Kovacs[1]
[1] ExaFuse. E-mail: andras.kovacs@broadbit.com

ABSTRACT. We explain the origin of proton spin, and calculate the proton's gyromagnetic factor. We compare our calculations against experimental data, and find a surprisingly precise match with the experimentally measured gyromagnetic factor value. Our theory also matches the operating principle of NMR devices.

In contrast, upon reviewing the quark model based interpretation of proton spin, we find that the quark model contradicts both the operating principle of NMR devices and the Pauli exclusion principle.

4.1. The proposed electromagnetic model based interpretation of proton spin

Let us recall that a scaled positron, whose total energy equals the proton mass, would have $r_{scaled} m_p c = \hbar$ angular momentum. The r_{scaled}=0.2103 fm distance denotes the scaled positron's Zitterbewegung radius.

Our proton model implies that the proton's spin angular momentum is the same as its toroidal angular momentum. We denote this toroidal angular momentum as L_p. It follows from chapter 3 results that the toroidal angular momentum is expressed by the $\boldsymbol{L}_p = \boldsymbol{r}_{pt} \times \left(\frac{\mu_N}{\mu_p}\right) m_p \boldsymbol{v}_{pt}$ formula, reflecting the fact that only a fraction of the proton mass is generated by the toroidal Zitterbewegung. Here, r_{pt}denotes the proton's toroidal radius, m_p is its mass, and v_{pt} is the toroidal speed component of the proton charge.

Recalling from chapter 3 that r_{pt} =0.831 fm, $v_{pt} = c/\sqrt{2}$, and $\mu_N/\mu_p = 1/2.793$, we obtain:

$$L_p = \boldsymbol{r}_{pt} \times \left(\frac{\mu_N}{\mu_p}\right) m_p \boldsymbol{v}_{pt} = \hbar$$

We thus found that, analogously to the electron case, the absolute value L_p of the proton's spin angular momentum $\boldsymbol{L}_p$ is equal to the reduced Planck constant:

$$L_p = \hbar$$

In the presence of an external magnetic field $\boldsymbol{B}_E$, we can write the vector L_p as the sum of two vectors. One vector is parallel to B_E, and the second one is orthogonal to it:

$$\boldsymbol{L}_p = \boldsymbol{L}_{p\parallel} + \boldsymbol{L}_{p\perp}$$

$$L_{p\parallel} = L_p \cos(\theta)$$

$$L_{p\perp} = L_p \sin(\theta)$$

where θ is the angle between the vectors $\boldsymbol{\mu}_p$ and $\boldsymbol{B}_E$. The proton is therefore subjected to a torque $\boldsymbol{\tau}$:

$$\tau = \left|\boldsymbol{\mu}_p \times \boldsymbol{B}_E\right| = \mu_p B_E \sin(\theta)$$

Consequently, the proton's toroidal structure will be in a Larmor precession, with angular frequency ω_{pP}:

$$\tau = \left|\frac{d\boldsymbol{L}_p}{dt}\right| = L_p \sin(\theta)\frac{d\phi}{dt} = L_p \sin(\theta)\,\omega_{pp}. \tag{4.1.1}$$

$$\mu_p B_E = \hbar\omega_{pp}$$

What we call "proton spin" s_p is the measured component of its angular momentum vector L_p along the external magnetic field B_E :

$$s_p = \hbar\cos(\theta)$$

Figure 4.1.1 illustrates the precessing proton structure under an external magnetic field $\boldsymbol{B}_E$.

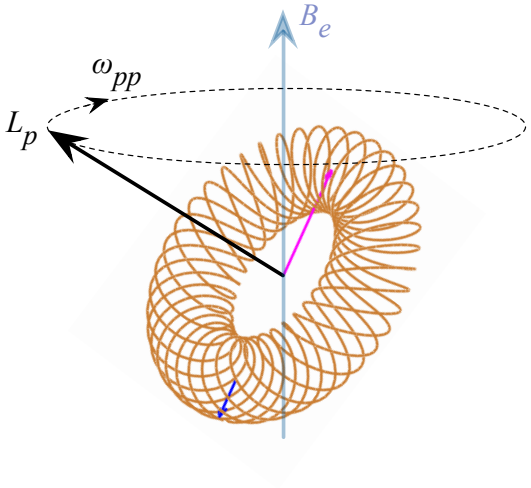

FIGURE 4.1.1. The Larmor precessing proton in external magnetic field $\boldsymbol{B}_E$. The proton's toroidal angular momentum vector $\boldsymbol{L}_p$ precesses with angular frequency ω_{pp}.

The measurable angular momentum transitions are also universally quantized to $\hbar$ value. This implies the following for the quantization of the angle θ :

$$\triangle L_{p\|} = \pm\hbar \Longrightarrow \theta \in \left\{\frac{\pi}{3}, \frac{2\pi}{3}\right\},\ \cos(\theta) = \pm\frac{1}{2}$$

$$s_p = \pm\frac{\hbar}{2}$$

The two spin values are characterized by two different energy levels, E_L and E_H;

$$\theta = \frac{\pi}{3} \Longrightarrow E_L = -\hbar\omega_{pp}$$

$$\theta = \frac{2\pi}{3} \Longrightarrow E_H = \hbar\omega_{pp}$$

$$\triangle E = E_H - E_L = 2\hbar\omega_{pp}$$

This energy gap $\triangle E$ is equal to $\hbar\omega_{NMRp}$, where ω_{NMRp} is the proton's Nuclear Magnetic Resonance (NMR) angular frequency. Therefore:

$$\omega_{NMRp} = 2\omega_{pp} = 2\mu_p B_E = \frac{e}{m_p}\frac{\mu_p}{\mu_N}B_E \tag{4.1.2}$$

This linear relationship between the applied B_E magnetic field and the resulting $\triangle E$ energy gap is the basis of NMR technology. It is widely recognized by the operators of NMR equipment that the proton spin is in a Larmor precession when being placed under magnetic field.

The value of ω_{NMRp} can be written as a function of the gyromagnetic factor g_p:

$$\omega_{NMRp} = \frac{e}{2m_p}g_p B_E \tag{4.1.3}$$

The proton's gyromagnetic-factor g_p is therefore

$$g_p = 2\frac{\mu_p}{\mu_N} = 5.585696018$$

Our calculation precisely matches the CODATA value of the proton's experimentally measured gyromagnetic factor, which is 5.5856946893.

We note that all of the above applies completely analogously to the electron, whose angular momentum value is also $\hbar$. The exact same Larmor precession arises when the electron is placed under an external magnetic field $\boldsymbol{B}_E$, and thus the measured value of its angular momentum becomes $s_e = \pm\frac{\hbar}{2}$. This phenomenon is the basis of Electron Spin Resonance (ESR) technology: the measured energy gap $\triangle E$ is then equal to $\hbar\omega_{ESR}$, where $\omega_{ESR} = 2\mu_B B_E$ and μ_B is the Bohr magneton.

4.2. The quark model based interpretation of proton spin

When Otto Stern measured the proton's $\mu_p = 2.793\mu_N$ magnetic moment in 1933, most physicists assumed that this measured value is the absolute value of the proton's internal magnetic moment vector. The quark model based magnetic moment calculations were developed under this assumption. With the recent advent of NMR technology, the operators of NMR equipment have recognized that under applied magnetic field the proton is subjected to Larmor precession. However, quark proponents never revised their calculations, which do not consider quarks being in Larmor precession. Any Larmor precession implies that the absolute value of individual quarks' angular momentum vector must be larger than the $\frac{\hbar}{2}$ value assumed in those calculations. Therefore, the quark model based spin interpretation is fundamentally contradicted by the NMR technology.

The Callan-Gross relation, which was mentioned in section 3.1, implies that a hypothetical quark's spin is individually measurable in high-energy scattering experiments. Yet proton spin measurements always yield $\mu_p = 2.793\mu_N$. One may wonder why the hypothetical quarks' magnetic moments always add up to the same value of $2.793\mu_N$. To

explain this constant value, the quark model based proton spin interpretation also requires that the three valence quarks remain in isotropic spin entanglement, which means that their individual spin orientations are always correlated, regardless of the spin measurement direction. Such spin-correlation is required to maintain a constant value of the measured proton magnetic moment. As mentioned in section 3.1, the color charge hypothesis was then introduced in order to remove a perceived contradiction between the three-quark spin correlation and the Pauli exclusion principle. However, Paul O'Hara recently proved that Greenberg's postulate does not automatically remove the contradiction with the Pauli exclusion principle: reference [1] proves that the isotropic spin entanglement of three particles is a mathematical impossibility if their spins are individually measurable. This mathematical contradiction holds regardless of the presence or absence of color charges. Therefore, the quark model based interpretation of the proton spin requires that the hypothetical quark spins are individually measurable in the case of high-energy scattering, but not individually measurable with low-energy techniques. Unsurprisingly, there is still zero experimental evidence of the postulated color charges, even though more than 50 years passed since Greenberg published his hypothesis. In the case of multi-lepton configurations, a stable quantum mechanical state requires that the involved lepton spins are precisely aligned in parallel or anti-parallel directions. The electron pair of an atomic orbital is anti-parallel spin correlated, while the leptons of a positronium can be either parallel or anti-parallel spin correlated. The $\mu_p < 3\mu_N$ value implies that the three hypothetical quarks are "almost parallel" spin correlated; i.e. the postulate of quantum mechanical stability without precise spin alignment has been introduced.

In summary, the quark model based proton spin interpretation involves a fundamental contradiction with NMR technology, and also involves a long chain of ad-hoc postulates.

Acknowledgements: The author thanks Paul O'Hara for insightful discussions of the Pauli exclusion principle, and thanks Giorgio Vassallo for some essential suggestions.

References. [1] A. Kovacs and G. Vassallo "Rethinking Electron Statistics Rules", Symmetry (2024)

CHAPTER 5

Neutrinos and Occam's razor

Andras Kovacs[1] and **Giorgio Vassallo**[2,3]
[1] ExaFuse. E-mail: andras.kovacs@broadbit.com
[2] International Society for Condensed Matter Nuclear Science (ISCMNS)-UK.
[3] Università degli Studi di Palermo - Engineering Department, viale delle Scienze, 90128 Palermo, Italy. E-mail: giorgio.vassallo@unipa.it.

In order to understand nuclear interactions, one must make sense of neutrinos which are emitted e.g. in nuclear beta decay, nuclear electron capture, or muon decay. Despite 90 years of neutrino physics, neutrinos are still being discussed in mutually contradictory terms:

- Neutrinos have been initially modeled as chargeless particles representing the $m \to 0$ solution of the Dirac equation, and with $\frac{\hbar}{2}$ spin value assignment. But it remained unclear what the meaning of a massless particle is.
- A different neutrino particle has been proposed for each lepton type, but it was unclear what their difference would be if they are all massless. Proponents of "several neutrino types" therefore proposed, without experimental evidence, that neutrinos have a small rest-mass. This hypothesis is in contradiction with the historically embraced $m \to 0$ models.
- Direct measurements of the neutrino mass converge to zero as the accuracy of measurements gradually improves. This historical "exponential decay to zero" is illustrated in figure 5.0.1. After 70 years of gradually improving mass measurements, there is no sign of any non-zero neutrino mass value. From all measurements, the current limit on neutrino mass is $<$0.12 eV.
- Neutrinos have been considered to be leptons, and this concept historically originates from the Dirac equation based neutrino models. However, we will demonstrate in the following paragraphs that assigning a non-zero lepton number to neutrinos is contradicted by experiments.
- Neutrinos are claimed to be not interacting electromagnetically. We show experimental refutation of this claim in chapter 8. We note that the claim of electromagnetic non-interaction originates from deep underground inverse beta decay experiments, which claim to detect solar neutrinos traveling through 2.5 km of rock. However, such experiments do not account for geo-neutrinos produced via the thorium decay chain; the omni-present thorium decay chain was simply assumed to be irrelevant. Addressing this assumption, we also show in chapter 8 that the neutrino-nucleus interaction might be much stronger than previously assumed.

These contradictory concepts show that neutrino physics is in the need of serious revision. As we show in the following paragraphs, it is nevertheless possible to describe neutrinos in surprisingly simple terms. Resolving this 90 year deadlock of neutrino physics is a key that unlocks a new interpretation of nuclear interactions.

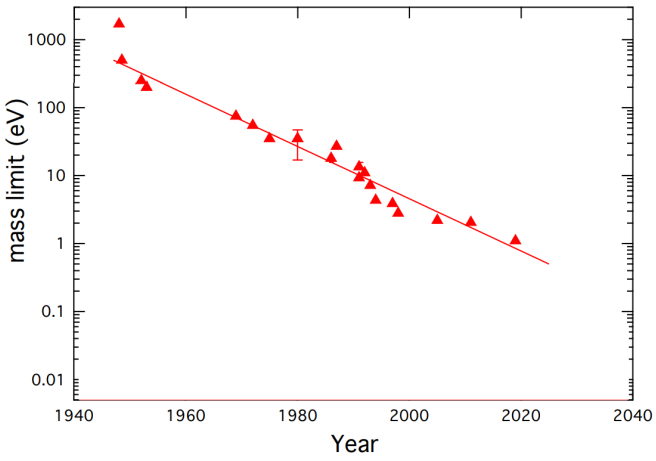

FIGURE 5.0.1. The historic evolution of neutrino mass limit from tritium decay measurements.

We start by considering the decay of a muon into an electron. Upon muon decay, the energy corresponding to muon-electron mass difference is departing as neutrino radiation. A muon is a lepton which always decays into an electron. The muon has the magnetic moment of a scaled electron, i.e. $\frac{e\hbar}{2m_\mu}$ magnetic moment value. Even its anomalous magnetic moment is close to the electron's $g = \left(1 - \frac{\alpha}{2\pi}\right)^{-1}$ factor. Therefore, for all practical purposes, we can consider the muon to be a scaled electron. We can thus apply the electron's circular Zitterbewegung structure to the muon as well.

We derived in section 1.2 the electron's longitudinal Lagrangian density $\mathscr{L}_\parallel$, which is measured in J/m^3 units, and is known as the "interaction term" of the electromagnetic Lagrangian density:

$$\mathscr{L}_\parallel = \boldsymbol{J} \cdot \boldsymbol{A} = JA = \frac{I_{electron}}{\pi r_{c,e}^2} \cdot \frac{\hbar}{e r_{ZBW}}$$

where I and r_{ZBW} are the Zitterbewegung current and radius, $r_{c,e}$ is the electron's classical charge radius. We also showed that this Lagrangian density fulfills the $\boldsymbol{J}_\square \cdot \boldsymbol{A}_\square = 0$ condition for stationary action, where the vectorial expression involves all four space-time coordinates.

We now apply the same circular Zitterbewegung structure to both electron and muon. Recall from section 1.2.2 that it is possible to compute the electron's or positron's mass from their longitudinal Lagrangian density $\mathscr{L}_\parallel$. By integration over the toroidal volume where the scalar field S is non-zero, we obtain exactly the particle mass:

$$W_{electron} = \iiint_V JA\, dV = \frac{I_{electron}}{\pi r_{c,e}^2} \cdot \frac{\hbar}{e r_{ZBW,e}} \cdot 2\pi^2 r_{ZBW,e} r_{c,e}^2 = \phi I_{electron} \approx 511 \text{ keV}$$

$$W_{muon} = \iiint_V JA\, dV = \frac{I_{muon}}{\pi r_{c,\mu}^2} \cdot \frac{\hbar}{e r_{ZBW,\mu}} \cdot 2\pi^2 r_{ZBW,\mu} r_{c,\mu}^2 = \phi I_{muon} \approx 105658.4 \text{ keV}$$

where $\phi = {}^{h}/_{e}$ is the magnetic flux quantum and I is the Zitterbewegung current.

It is evident from the above expression that the $\mu^- \to e^-$ decay involves a change in $\mathscr{L}_\parallel = \boldsymbol{J} \cdot \boldsymbol{A}$. It is shown in the first appendix of chapter 1 that $\boldsymbol{J}_\square \cdot \boldsymbol{A}_\square$ is equivalent to the electromagnetic $\frac{1}{2\mu_0}\left(S^2 - \frac{2}{c}\mathcal{I}\boldsymbol{E} \cdot \boldsymbol{B}\right)$ expression. Since neutrino emission is associated

with a change in $\boldsymbol{J}\cdot\boldsymbol{A}$, neutrino dynamics should be described by the $\frac{1}{2\mu_0}\left(S^2-\frac{2}{c}\mathcal{I}\boldsymbol{E}\cdot\boldsymbol{B}\right)$ expression.

Let us find such a wave solution to Maxwell's equation that its Lagrangian density is given by the $\frac{1}{2\mu_0}\left(S^2-\frac{2}{c}\mathcal{I}\boldsymbol{E}\cdot\boldsymbol{B}\right)$ expression, where the electric and magnetic fields are parallel. The gaugeless Maxwell equation is simply $\boldsymbol{\partial}^2\boldsymbol{A}_{\square}=0$, and we firstly look for its longitudinal wave solutions. One trivial solution transforms electric and scalar field energies into each other, with the electric field pointing along the direction of propagation. For a longitudinal wave traveling along the z direction, the trivial longitudinal solution is:

$$E_z=E_0\sin\left(\omega t-kz\right),\ S=S_0\sin\left(\omega t-kz\right)$$

where $S_0=E_0$ in Natural units, and the wave is propagating at the speed of light along the z direction.

An other trivial solution transforms magnetic and scalar field energies into each other, with the magnetic field pointing along the direction of propagation. For a longitudinal wave traveling along the z direction, the trivial longitudinal solution is:

$$B_z=B_0\cos\left(\omega t-kz\right),\ S=\mathcal{I}S_0\cos\left(\omega t-kz\right)$$

where $\mathcal{I}$ is the Clifford pseudo-scalar, $S_0=B_0$ in Natural units, and the wave is propagating at the speed of light into the z direction.

Recall from chapter 1 that the complete electromagnetic Lagrangian density is:

$$\mathscr{L}=\frac{1}{2\mu_0}\left(-\frac{E^2}{c^2}+B^2+S^2-\frac{2}{c}\mathcal{I}\boldsymbol{E}\cdot\boldsymbol{B}\right)$$

The above trivial longitudinal solutions correspond to either $-\frac{E^2}{c^2}+S^2=0$ with no magnetic field or $B^2+S^2=0$ with no electric field. It follows from the Lagrangian formula that a purely scalar electromagnetic field does not exist; the detailed explanation can be found in the appendix of this chapter.

Since electromagnetic wave solutions can be superposed, we can combine the trivial longitudinal wave solutions. Adding the above-written electric and magnetic wave expressions, we get a longitudinal wave where the out-of-phase electric and magnetic field energies rotate into each other with scalar field mediation.

Let us now consider adding the trivial electric and magnetic longitudinal waves with the same $\sin\left(\omega t-kz\right)$ phase. The amplitude of the scalar wave part becomes $S_0^2\left(1+\mathcal{I}\right)^2=S_0^2\cdot 2\mathcal{I}$. Multiplying the in-phase electric and magnetic fields gives a combined wave amplitude of $E_0B_0=S_0^2$. Clearly, we have found the longitudinal wave solution that corresponds to $S^2-\frac{2}{c}\mathcal{I}\boldsymbol{E}\cdot\boldsymbol{B}=0$, with parallel oriented electric and magnetic fields. In natural units, the neutrino wave solution is:

$$\nu:\left\{\begin{array}{c} E_z=E_0\sin\left(\omega t-kz\right),\ B_z=\pm B_0\sin\left(\omega t-kz\right) \\ S=S_0\sin\left(\omega t-kz\right)\pm\mathcal{I}S_0\sin\left(\omega t-kz\right)\end{array}\right\} \tag{5.0.1}$$

where $\mathcal{I}$ is the Clifford pseudo-scalar, $S_0=E_0=B_0$ in Natural units, and the wave is propagating at the speed of light into the z direction. In this simple plane wave case, the electric and magnetic fields have no x,y components. The reason why this neutrino solution has not been recognized in the past is its non-zero scalar field component.

The transversal part of the electromagnetic Lagrangian density is $\mathscr{L}_{\perp}=\frac{1}{2\mu_0}\left(-\frac{E^2}{c^2}+B^2\right)$. The well-known transversal light wave is the simplest such wave solution to Lagrangian density given by $\mathscr{L}_{\perp}$. In natural units, the linearly polarized transversal light wave is:

$$\gamma : \left\{ \begin{array}{l} E_x = E_0 \sin(\omega t - kz), \\ B_y = \pm B_0 \sin(\omega t - kz) \end{array} \right\} \tag{5.0.2}$$

It is thus a natural choice to associate neutrinos with the longitudinal electromagnetic wave, given by expression 5.0.1. The $\mathscr{L}_\perp = \frac{1}{2\mu_0}\left(-\frac{E^2}{c^2} + B^2\right)$ and the $\mathscr{L}_\parallel = \frac{1}{2\mu_0}\left(S^2 - \frac{2}{c}\mathcal{I}\boldsymbol{E}\cdot\boldsymbol{B}\right)$ components of electromagnetic Lagrangian density each have a trivial wave solution: these are the transversal and longitudinal electromagnetic waves.

Recall from chapter 1 that a stationary electron is characterized by a vector potential that is parallel to the Zitterbewegung circle; the vector potential is said to be in the $\boldsymbol{A}_\parallel$ direction. As the particle gains kinetic energy, its vector potential gains a component along the Zitterbewegung axis, and we denote this component with the $\boldsymbol{A}_\perp$ symbol. If the electron moves close to the speed of light, its vector potential comprises almost purely $\boldsymbol{A}_\perp$ component. A transversal electromagnetic wave is emitted in those reactions that involve a change of particle kinetic speed, such as a transition between two orbitals. A longitudinal electromagnetic wave is emitted in those reactions that do involve a change of particle structure. In other words, the electromagnetic wave is described by the $\mathscr{L}_\perp$ Lagrangian density when its producing particle undergoes a change of $\boldsymbol{A}_\perp$, and the electromagnetic wave is described by the $\mathscr{L}_\parallel$ Lagrangian density when its producing particle undergoes a change of $\boldsymbol{A}_\parallel$.

Our neutrino model matches the experimentally observed light-speed propagation of neutrinos, is compatible with the zero-converging neutrino mass measurements, and implies the 0 lepton number assignment to neutrinos. As will be shown in section 7.4.4, such lepton number assignment is the experimentally correct one.

The harmonic neutrino waves differ from each other only in their frequency and handedness, with the handedness being selected by the $\pm$ sign of expression 5.0.1. Analogously to the well-known case of transversal electromagnetic waves, the appropriate method of a given wave's detection depends on its frequency. While high-frequency neutrinos are being detected by scintillation sensors, low-frequency neutrinos should be detected by different equipment.

Nuclear reactions and heavy particle decays are energetic events, and the neutrinos emitted in such reactions have very high frequency. High-frequency transversal waves interact mainly via Compton-scattering and particle-antiparticle pair creation when being in the proximity of a nucleus. It is logical to anticipate the same interaction types for high-frequency longitudinal waves, but at a much lower interaction cross-section.

The Compton-scattering of electrons generates scintillation events, and high frequency neutrinos are indeed detected mainly by scintillation detectors.

Regarding particle-antiparticle pair production in the proximity of a nucleus, an interesting muon-related experiment is reported in reference [1]. Its authors measure correlated production of positrons and neutrons when their proton-containing detector is exposed to neutrino radiation originating from muon decay. The overall process can be interpreted as the following chain of reactions:

$$\mu^- \to e^- + \nu, \;\; \nu \to e^- + e^+, \;\; e^- + p^+ \to n$$

The last step of neutron production is possible because the produced electrons are highly energetic. Upon muon decay, neutrino radiation carries away 105 MeV energy. If our hypothesis of neutrino induced $e^- + e^+$ pair production is correct, the produced electrons and positrons shall have up to 52 MeV kinetic energy each. This hypothesis is compatible with the positron energy distribution shown in figure 29 of [1], where the detected positron energy indeed goes up to 50 MeV. While a skeptic might say that a

conclusive experiment should subtract the background positron energy distribution from the experiment-related positron energy distribution, it is clearly very improbable to see 40-50 MeV positrons in the background. This experiment thus demonstrates neutrino induced $e^- + e^+$ pair production.

In summary, both theory and experiments point to neutrinos being just longitudinal electromagnetic waves.

References. [1] C. Athanassopoulos et al "Evidence for neutrino oscillations from muon decay at rest", Physical Review C, Volume 54.5 (1996)

Appendix 1: Examining whether a purely scalar wave exists

We note that the current density field is identified with the space-time derivatives of the electromagnetic scalar field:

$$\frac{1}{\mu_0}\boldsymbol{\partial} S = \frac{1}{\mu_0}\left(\gamma_x\frac{\partial S}{\partial x} + \gamma_y\frac{\partial S}{\partial y} + \gamma_z\frac{\partial S}{\partial z} + \gamma_t\frac{1}{c}\frac{\partial S}{\partial t}\right) = \boldsymbol{J}_{\square} \tag{5.0.3}$$

It is important to note that equation 5.0.3 applies microscopically. While a macroscopic current of electrons in a wire primarily comprises the flow of individual electron particles, the role of equation 5.0.3 becomes apparent only after sufficiently zooming in. The law of electric charge conservation can now be formulated as:

$$\frac{1}{\mu_0}\boldsymbol{\partial}\cdot(\boldsymbol{\partial} S) = \boldsymbol{\partial}\cdot\boldsymbol{J}_{\square} = \frac{\partial J_x}{\partial x} + \frac{\partial J_y}{\partial y} + \frac{\partial J_z}{\partial z} + \frac{\partial \rho}{\partial t} = 0 \tag{5.0.4}$$

The wave equation of the scalar field S can be deduced from the charge-current conservation law:

$$\boldsymbol{\partial}\cdot(\boldsymbol{\partial} S) = \boldsymbol{\partial}^2 S = \frac{\partial^2 S}{\partial x^2} + \frac{\partial^2 S}{\partial y^2} + \frac{\partial^2 S}{\partial z^2} - \frac{1}{c^2}\frac{\partial^2 S}{\partial t^2} = \nabla^2 S - \frac{1}{c^2}\frac{\partial^2 S}{\partial t^2} = 0 \tag{5.0.5}$$

This scalar wave equation implies that scalar fields travel at the speed of light. Such a speed-of-light scalar field circulation does exist: it is the Zitterbewegung phenomenon, which we examined in preceding chapters.

Can we write a corresponding scalar wave solution in the simple $S = S_0\cos(\omega t - kz)$ form? Keeping in mind that $S \equiv \left(-\frac{1}{c}\partial_t A_t + \nabla\cdot\mathbf{A}\right)$, the corresponding vector potential field expression is:

$$A_z = \frac{ca}{\omega}\sin(\omega t - kz)\,\gamma_z, A_t = \frac{ca}{\omega}\sin(\omega t - kz)\,\gamma_t, A_x = 0, A_y = 0$$

where a is the amplitude parameter.

With the above formulation, the scalar field becomes the sought harmonic wave: $S = -2a\cos(\omega t - kz)$, i.e. the wave amplitude is $S_0 = 2a$.

At the same time, the electric field expression becomes:

$$\mathbf{E} = \left(-\frac{1}{c}\partial_t\mathbf{A} + \nabla A_t\right) = -a\cos(\omega t - kz)\,\gamma_z - a\cos(\omega t - kz)\,\gamma_z = -2a\cos(\omega t - kz)\,\gamma_z$$

Since the electric field becomes non-zero, a purely scalar longitudinal wave does not exist; longitudinal waves always have electric and/or magnetic field components as well.

CHAPTER 6

The discovery of nuclear electrons that appear during β-decay

Andras Kovacs[1], **Valery Zatelepin**[2], **Dmitry Baranov**[2], and **Heikki Sipilä**[3]
[1] ExaFuse. E-mail: andras.kovacs@broadbit.com
[2] INLEAS laboratory
[3] Fenno-Aurum

ABSTRACT. The nuclear electron concept does not violate Noether's theorem, does not require the emission of heavy particles that were never observed in any β-decay, and does not require fractional elementary charges. Each of these advantages is a major argument in favor of the nuclear electron concept.

We show how the energy spectrum of β-decay products reveals radial oscillation signatures, and calculate the most probable kinetic energy of an emitted electron. The demonstrated match between our simple calculation and experiments suggest two separate particles within a neutron, each having its own wavefunction.

However, in the context of a nuclear electron, it remained unclear up to now how to reconcile the Heisenberg uncertainty principle with an fm-scale nuclear radius. The fm-scale neutron size suggests treating it as a single particle, where its positive and negative elementary charges combine into a single composite particle.

While we normally associate each elementary charge with a distinct particle, multiple charges may combine into a single particle at the nuclear scale. The neutron comprises two elementary charges: it appears mainly as a single-particle, and rarely a two-particle system. We refer to its negative elementary charge as a "nuclear electron", with the understanding that this negative charge can be treated as a separate particle only in a tiny fraction of time. The nuclear capture or emission of a negative elementary charge involves the capture or decay of a nuclear electron particle. Using a precise measurement method, we determine that the nuclear electron input mass is 1554 keV.

6.1. The neutron's single particle aspect

We showed in chapter 3 that the proton is an elementary particle. It follows that the neutron is a composite of a proton and a negative elementary charge. Identifying the neutron's negative charge with a hypothetical nuclear electron, our first goal is to evaluate its size. We start from magnetic moment considerations. The neutron's magnetic moment is the sum of the proton's and nuclear electron's contributions. To arrive at the neutron's $-1.91\mu_N$ magnetic moment, the nuclear electron's contribution must be $-4.7\mu_N$:

$$\mu_n = \mu_+ + \mu_- = (2.79 - 4.7)\,\mu_N = -1.91\mu_N$$

where $\mu_N = \mu_B/1836.2$ is the nuclear magneton, and μ_B is the Bohr magneton.

With respect to the electron's $-\mu_B$ magnetic moment, a shrinking magnetic moment value is in direct proportion with the shrinking Zitterbewegung radius. Considering that the electron's Zitterbewegung radius is the reduced Compton radius ($r_{Compton}$=386.16 fm), the Zitterbewegung radius of the proton-bound nuclear electron can be estimated as follows:

$$r_- = r_{Compton}\frac{4.7\mu_N}{\mu_B} = 386.16\frac{4.7}{1836.2}\,fm = 0.99\,fm$$

This result is similar to the experimental "proton charge radius" value, and shows that the nuclear electron is captured by the proton's magnetic field; i.e. its Zitterbewegung trajectory is defined by the proton's magnetic field. With the advancement of electron-proton scattering measurements, it has become possible to directly map out the neutron's radial charge distribution. Such radial charge distribution data is measured for example at JLAB [**1**], and is visualized in figure 6.1.1. This experimental data confirms the above-calculated result that the neutron's negative charge extends only slightly further than its positive charge distribution.

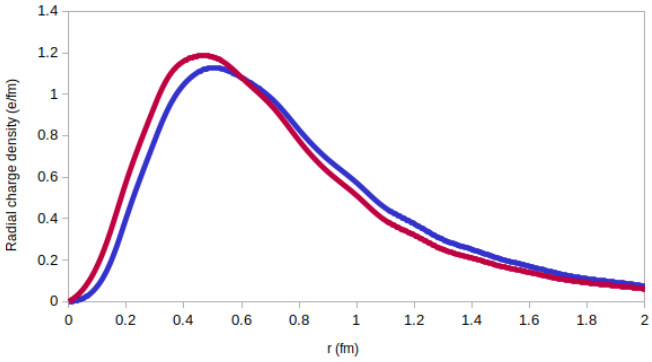

FIGURE 6.1.1. The radial density of the neutron's positive (red) and negative (blue) charges, from JLAB measurements [**1**].

As a first approximation, we established that the neutron has a single Zitterbewegung structure, and thus behaves as a single particle. As a more precise approximation, we can model the neutron being in a single particle state most of the time, and in a proton + nuclear electron state a tiny fraction of time. Despite the small probability of finding a proton + nuclear electron state, it is essential for understanding neutron decay. To explore this decay dynamics let us consider how a bound heavy electron decays.

6.2. The decay of an electron-like particle

The best known electron-like particle is the muon. As discussed in chapter 5, the decay of a stationary muon emits neutrino radiation that matches the muon-electron mass difference: $E_\nu = m_\mu c^2 - m_e c^2$. Suppose that we watch this muon decay event from a highly accelerated frame, with $\gamma_L = 10$ Lorentz boost factor value. We derived the $r_{ZBW}^{-1} = m$ relation in section 1.2; the boost-induced compression of Zitterbewegung radius compression can be interpreted as a relativistic transversal Doppler effect. In a highly boosted frame, the particle's electromagnetic vector potential has mainly just $\boldsymbol{A}_\perp$ component, and the path of its charge converges to a linear movement along its Zitterbewegung axis. This boost effect is illustrated in figure 6.2.1. Based on the $m_\mu/m_e \approx 207$ mass ratio, a stationary muon's Zitterbewegung radius is $\frac{386.16}{207}$ fm=1.87 fm. A $\gamma_L = 10$ boosted muon's Zitterbewegung radius is 10 times lower, i.e. just 0.187 fm.

From the perspective of our $\gamma_L = 10$ reference frame, the decaying muon has $9m_\mu c^2$ kinetic energy. The emission of $E_\nu = m_\mu c^2 - m_e c^2$ neutrino energy is independent of the observer's reference frame. In this highly boosted reference frame, the resulting electron carries on the enormous kinetic energy of $9m_\mu c^2$=951 MeV. Such a highly energetic electron travels close to the speed of light, on a nearly straight trajectory. In this boosted reference frame, the muon decay is not a dramatic event: the emerging particle retains a similar relativistic mass, and keeps traveling close to the speed of light on a nearly straight

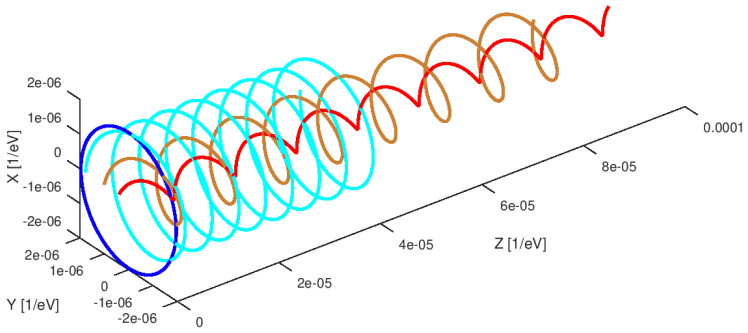

FIGURE 6.2.1. The electron Zitterbewegung trajectories at various kinetic energies. v/c=0 (dark blue), 0.43, 0.86, and 0.98 (red).

trajectory. In other words, the decay event produces mainly an energetic electron, and only a minor part of the particle energy is converted into neutrino radiation.

The point of the above example is to illustrate that a fast-moving electron-like particle decays into a fast-moving electron. On the other hand, a stationary electron-like particle decays with the emission of neutrino radiation. Taking the example of ^{3}H decay products, whose energy distribution is shown in figure 6.2.2, we see decay into an energetic electron at one end of the spectrum, and decay into a stationary electron plus neutrino radiation at the other end of the spectrum. This data tells us that the ^{3}H nucleus comprises a negative charge that oscillates for ∼12 years between stationary and near light-speed kinetic states.

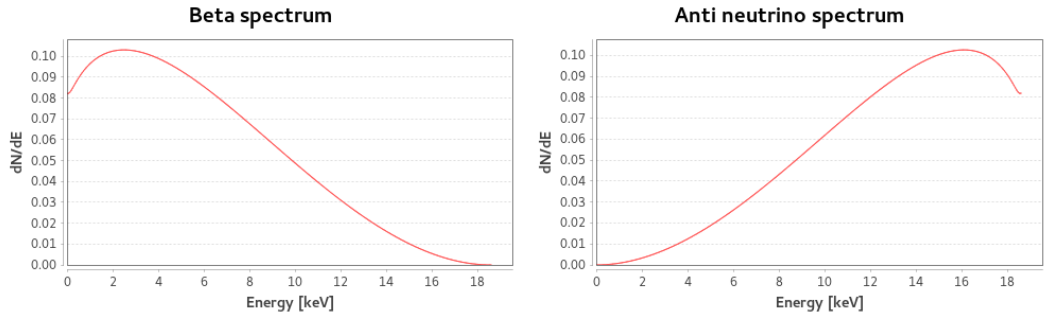

FIGURE 6.2.2. The energy distribution of ^{3}H decay products.

Taking the energy values of figure 6.2.2 at face value, the decaying negatively charged particle would be only very slightly heavier than an ordinary electron. However, we must consider also the effect of nuclear binding energy. We therefore look into the dynamics of bound-state oscillations.

6.3. The radial oscillation of a bound electron

A proton-bound electron occupies a quantum mechanical atomic orbital. Electron orbitals involve a rotation around the nucleus, which was explored in sections 2.2-2.3, and also involve radial oscillation. Up to now, these orbital wavefunctions have been calculated by using the Dirac equations on a point-particle model. Figure 6.3.1 shows the radial probability distribution of some proton-bound electron orbitals. Although the electron probability density is the highest near the nucleus, there is only a small overall probability of finding the electron close to the nucleus because of the tiny volume element in close nuclear proximity. Since the mean orbital radii are much larger than the electron's Zitterbewegung radius, or its charge radius, the point particle approximation

gives accurate results for the electron probability distribution. On the other hand, the point particle approximation is not useful for determining what happens at femtometer-range radial distances.

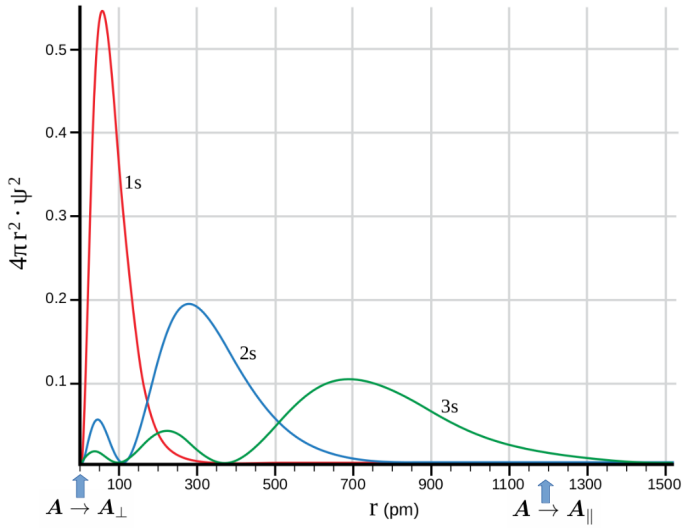

FIGURE 6.3.1. The radial probability distribution of some proton-bound electron orbitals. As indicated, the electron's electromagnetic vector potential rotates between the $\boldsymbol{A}_\perp$ and $\boldsymbol{A}_\parallel$ orientations as it oscillates between the $r \to 0$ and $r > 1000$ pm ranges.

Having determined the experimentally matching electron and proton structures, we may investigate the electron's radial oscillation all the way down to the nuclear scale.

Let us start by considering a classical model of radial electron oscillation state around a positively charged nucleus. At the oscillation turn-around point, the electron kinetic speed is zero, and its potential energy is the largest. We may say that the electron's rest mass is the highest at this location; i.e. its charge is at the largest $\boldsymbol{A}_\parallel$ vector potential component here. The electron's kinetic speed is largest at the midpoint, where the nucleus is located, and its potential energy is the lowest there. I.e. the electron has largest $\boldsymbol{A}_\perp$ vector potential component at the midpoint.

The electron's total energy remains invariant during such oscillation, and let us recall from chapter 1 the $E_e^2 = (eAc)^2$ relation, which relates the electron energy to the vector potential experienced by the electron charge. Essentially, we may characterize this radial oscillation as follows: part of the electron's vector potential is rotating between the $\parallel$ and $\perp$ directions.

This radial electron oscillation model remains similar in the quantum mechanical case, but its oscillation wavenumber must form a standing wave between two reflection points. The back and forth reflection of the standing electron wave requires the electron momentum being non-zero at the reflection points. Beyond the reflection points, the quantum mechanical wavefunction decays exponentially, as illustrated by the wavefunction tails in figure 6.3.1. The conservation of total energy means that the electron's spherical charge continues to experience the same vector potential value at every location; thus the orbital wavefunction is characterized by a single oscillation frequency and single energy eigenvalue. As in the classical case, the quantum mechanical radial oscillation can be characterized as electron's vector potential being rotated between the $\parallel$ and $\perp$ directions. Such an equivalence between the classical and quantum mechanical perspectives is illustrated by the virial theorem remaining valid in the quantum mechanical regime.

A radial oscillation involves electron acceleration, and thus radiates energy in the classical oscillator case. There is no energy radiation in the quantum mechanical case because the electron oscillates at frequencies that form standing waves, and the ground state frequency is at the limit of the Heisenberg uncertainty principle. In other words, the ground state oscillation is in balance with the electromagnetic vacuum noise. We note that a detailed analysis of this process can be found in "The Lamb shift as a spectrometer of electron-noise interaction" chapter of reference [**2**].

One may ask what A value the electron charge experiences at the mid-point: wouldn't it just annihilate against the positive charge? At its closest approach, the electron charge surrounds the proton. At that point, the electrostatic potential at the electron's charge surface is zero because the electron and proton potentials counter-balance each other; this means that the electron's vector potential is nearly fully rotated into just the $\boldsymbol{A}_\perp$ component and its speed converges to c. Therefore, if the electron could randomly decay into a lighter particle, the energy distribution of its decay products would be qualitatively the same as shown in figure 6.2.2:

- If the hypothetical electron decay happened near the nucleus, its decay energy would transform almost entirely into the kinetic energy of a lower mass particle. Such decay has low probability because the electron moves quickly through this location.
- If the hypothetical electron decay happened near the oscillation's classical turn-around points, its decay energy would transform almost entirely into neutrino radiation. Such decay has high probability because the electron moves slowly in this region.

Based on the above reasoning, the experimental energy distribution of β-decay products can be interpreted as a radial oscillation signature. In other words, it seems indeed reasonable neutron model that it is in a single particle state most of the time, and in a proton + nuclear electron state a tiny fraction of time. In the following section, we validate this model more quantitatively.

6.4. Calculation of β-decay peak energy from momentum conservation

In a β-decaying nucleus, a nuclear electron decays into an ordinary electron. Assuming a random decay time, the decay event happens mainly around the oscillation turn-around points where the low-speed nuclear electron spends more time. We established in section 6.3 that the decay energy is mainly carried away by neutrino radiation in this turn-around region, and mainly carried away by an energetic electron in the nuclear mid-point region. The decay event rarely happens near the nuclear mid-point because the nuclear electron speed is the highest in that region. Such a probability distribution of decay event locations leads to a corresponding distribution of decay product energies: this anticipated distribution indeed matches with the experimental distribution shown in figure 6.2.2. However, one may notice in figure 6.2.2 that the probability is not maximized at zero electron energy; it peaks at a small but non-zero value. To understand the reason, let us consider the nuclear electron decay event from momentum conservation point of view.

The nuclear electron has its highest decay probability in the turn-around region, where its kinetic energy is almost zero. Let E_ν denote the most probable value of emitted neutrino radiation. As neutrino radiation does not have a rest mass, it carries $p_\nu c = E_\nu$ momentum. By conservation of momentum, the emitted electron gains $p_\nu c$ momentum into opposite direction at the decay event. The corresponding peak electron energy and kinetic energy values are:

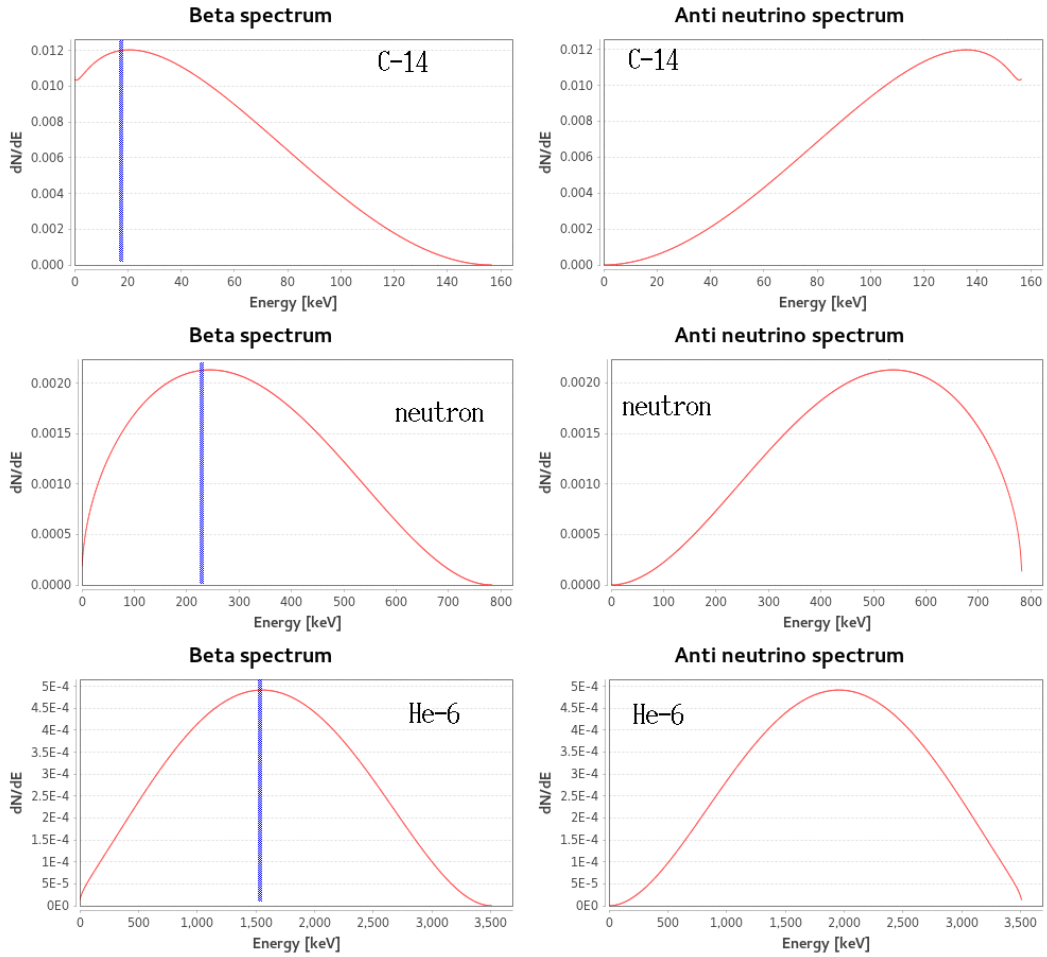

FIGURE 6.4.1. The energy distribution of light isotopes' decay products, from low to high decay energy. The vertical lines indicate the peak electron energy values calculated from equation 6.4.2.

$$E_e = \sqrt{(p_\nu c)^2 + (m_e c^2)^2}, \qquad T_e = \sqrt{(p_\nu c)^2 + (m_e c^2)^2} - m_e c^2 \tag{6.4.1}$$

On the other hand, we may also relate E_ν and T_e to the total energy of the β-decay. Let us denote the total β-decay energy as E_β. Since the emerging neutrino energy and electron kinetic energy add up to E_β, we get a simple relationship between the energy peaks: $E_\beta = E_\nu + T_e$. We can therefore write the electron kinetic energy in terms of E_β:

$$T_e = \sqrt{(E_\beta - T_e)^2 + (m_e c^2)^2} - m_e c^2 \tag{6.4.2}$$

The above equation is a second-order equation which can be solved for T_e. Figure 6.4.1 shows the experimental neutrino and electron energy spectrum for various light nuclei. As can be seen, the experimental electron energy peak location nicely matches the values calculated from equation 6.4.2. Our results clarify why the neutrino energy spectrum is an almost monotonously growing curve at low decay energy, and why it peaks near the middle of the spectrum at high decay energy.

As far as the authors know, the above calculation is the simplest quantitative evaluation of peak electron energy in β-decays.

6.5. The exponential tail of a nuclear electron wavefunction

The basic nuclear bond is formed between a proton and a nuclear electron. In larger nuclei, the nuclear electron wavefunction is distributed over multiple protons. Eventually, we might understand how to calculate the nuclear electron wavefunction. However, we can already identify one common feature of nuclear electron wavefunctions, which universally holds for **any** bound state wavefunction: its radial distribution has an exponentially decaying tail. This exponential tail is given by the $\psi(r) \sim e^{-\frac{r}{a}}$ relation, where r is the radial distance, and a is a wavefunction parameter. For ordinary atomic orbitals, the a parameter is proportional to the orbital's main quantum number, as can be seen in figure 6.3.1. This $\psi(r) \sim e^{-\frac{r}{a}}$ relation is universal because the exponential tail arises as a consequence of momentum conservation at the turn-around point of radial oscillation.

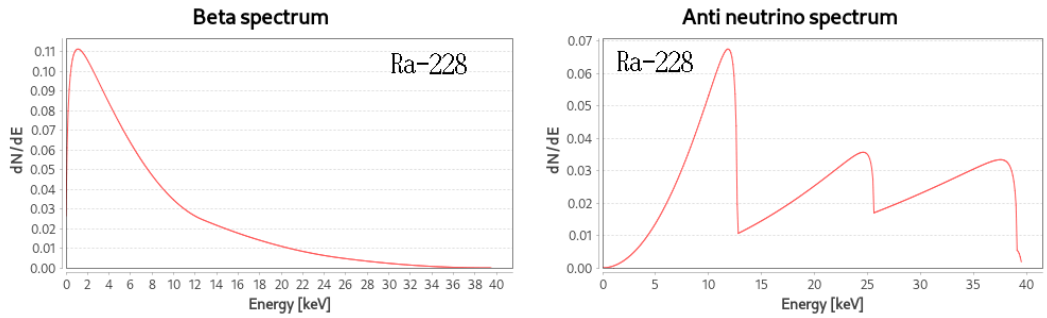

FIGURE 6.5.1. The energy distribution of ^{228}Ra β-decay products.

To demonstrate the nuclear electron's $\psi(r) \sim e^{-\frac{r}{a}}$ wavefunction tail, let us take the ^{228}Ra isotope example. Upon the β-decay of ^{228}Ra, the emerging electron has just about 1 keV kinetic energy, and the corresponding neutrino radiation is also only a few keV. If the β-decay event happened near the nucleus, the emerging electron would require a high kinetic energy in order to escape from the potential well of a highly charged nucleus. Specifically, the remaining Z=89 nuclear charge implies that ~1 MeV kinetic energy is required at ~130 fm radial distance, and ~10 MeV kinetic energy is required at ~13 fm radial distance. However, energy distribution of ^{228}Ra β-decay products, which is shown in figure 6.5.1, is analogous to figure 6.2.2: the decay energy goes mainly into neutrino radiation, which means that the nuclear electron has been close to stationary at its most probable β-decay. The unavoidable conclusion is that the β-decay of ^{228}Ra happens very far out from the nucleus, at picometer-scale radial distance. Essentially, the nuclear electron's $\psi(r) \sim e^{-\frac{r}{a}}$ wavefunction tail represents a tunneling region, where the mass difference between a nuclear electron and an ordinary electron is converted into a potential energy gain. In other words, the ^{228}Ra isotope has a very far-reaching nuclear halo prior to its nuclear decay, which comprises the exponentially decaying part of nuclear electrons' wavefunction. In a small fraction of time, β-decaying nuclei are much larger than their proton-filled radius. Figure 6.5.2 illustrates nuclear electrons' wavefunction tail around ^{228}Ra.

We experimentally demonstrate the existence of the above-described large nuclear halo. In the thorium decay chain, high-energy gamma peaks originate from β-decay products. We investigate gamma peaks in the 1.1 MeV region, and look for chemically induced differences in such nuclear radiation emissions.

We prepared two different thorium-containing solutions. A copper-based solution comprises 4 g thorium-nitrate, 10 g water, and 14 g copper-perchlorate hexahydrate. The radiation spectra of this solution are indicated by red color in figures 6.5.3-6.5.4. A

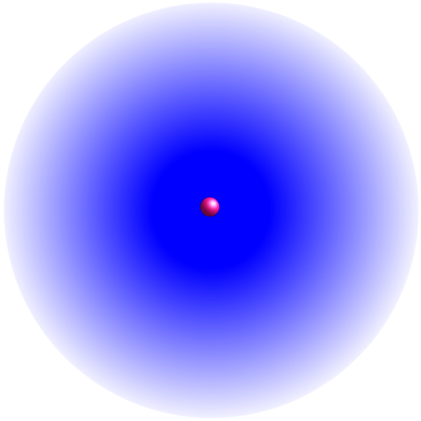

FIGURE 6.5.2. An illustration of ^{228}Ra's giant nuclear halo: the exponential tail of a nuclear electron wavefunction, represented by blue color, extends far beyond the fm-scale nuclear core.

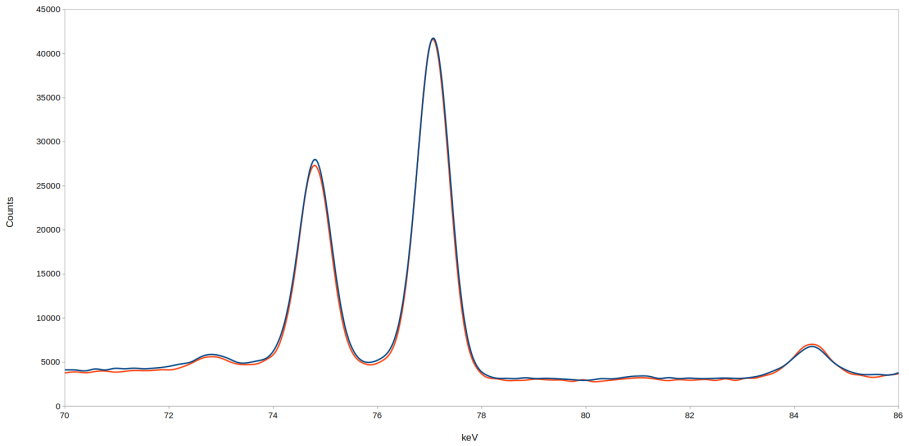

FIGURE 6.5.3. The gamma spectra of the two thorium solutions in K-line emission region. Red: solution with concentrated copper-perchlorate, blue: solution with concentrated potassium-carbonate.

potassium-based solution comprises 4 g thorium-nitrate, 16 g water, and 10 g potassium-carbonate. The radiation spectra of this solution are indicated by blue color in figures 6.5.3-6.5.4. We made high-precision gamma spectra measurements on these liquid samples, using Baltic Scientific Instruments' high purity germanium (HPGe) based detector, which resides in a lead shielded chamber. Figure 6.5.3 shows the normalization of the two measured spectra to the same K-line emission intensity, which means that we are looking at the same overall radioactive decay rate in both solutions.

Figure 6.5.4 shows gamma peaks in the 1.1 MeV region, which correspond to nuclear de-excitation of β-decay products. The gamma noise floor is the same for both solutions, as anticipated for the normalized decay rate. In contrast, only the 1111 keV gamma peak has the same strength for both solutions; two peaks are stronger in the solution with concentrated copper-perchlorate, and one peak is stronger in the solution with concentrated potassium-carbonate. These varying peak heights prove that the chemical environment does impact the nuclear processes in β-decaying heavy isotopes. The involved isotopes therefore demonstrate a large nuclear halo that comprises the exponential tail of nuclear electron wavefunctions.

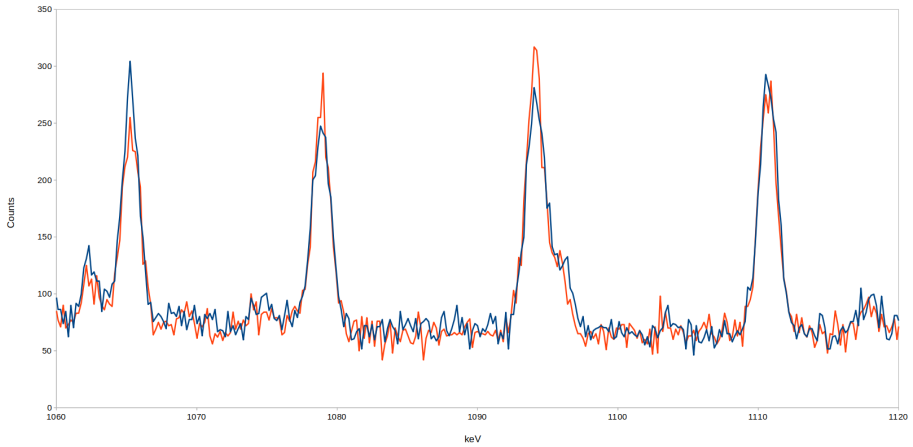

FIGURE 6.5.4. The gamma spectra of the two thorium solutions in the 1.1 MeV region. Red: solution with concentrated copper-perchlorate, blue: solution with concentrated potassium-carbonate.

The key importance of nuclear electron binding is demonstrated by the fact that any deviation from nuclear stability causes either electron emission or absorption. These electron absorbing and emitting nuclei are in the orange and blue colored regions of figure 6.5.5. The emission of other particle types happens only under highly energized conditions, where the whole nuclear structure becomes destabilized.

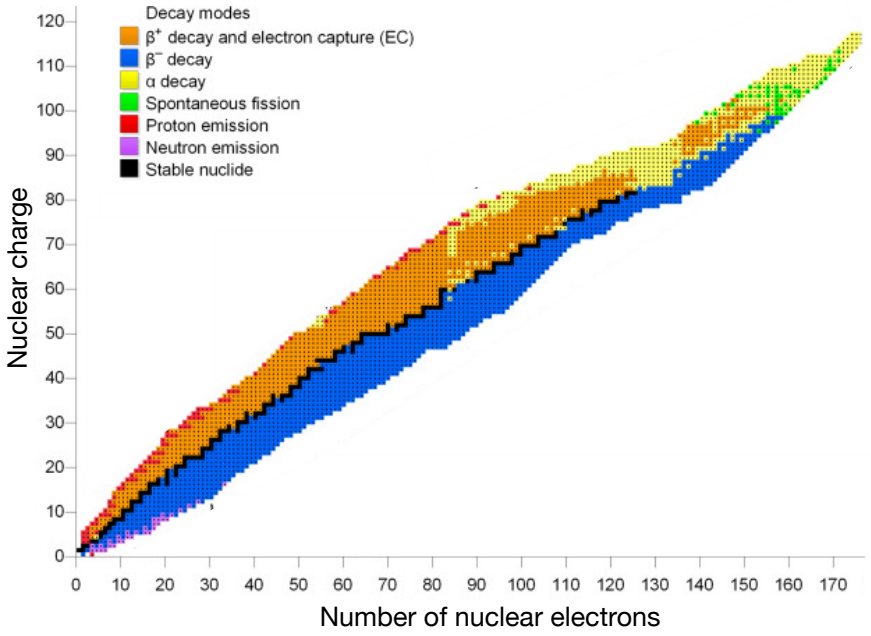

FIGURE 6.5.5. Stable isotopes comprise stable nuclear electron bonds. A deviation from stability (black isotopes) causes either electron emission (blue region) or electron capture (orange region). Other decay types happen only at the fringes, where the whole nuclear structure becomes destabilized.

6.6. A precise measurement of the nuclear electron mass

In the following, we use the e_n^- symbol to refer to the nuclear electron particle. As before, we emphasize that it behaves as a distinct particle only a tiny fraction of time. The e_n^- particle's nuclear capture involves a change of its wavefunction's quantum mechanical state. Quantum mechanical state changes must be accompanied by single frequency electromagnetic radiation. Therefore, the binding energy of the e_n^- capture process should be emitted as gamma radiation. On this basis, we seek experimental data of gamma emission from electron capture capable nuclei.

Suppose that an isotope with mass number M and charge Z is capable of e_n^- capture via the $(M, Z)+e_n^- \rightarrow (M, Z-1)$ reaction. Let E_b represent the binding energy of e_n^- capture. In the case of an ordinary electron capture, let E_{ec} represent the $(M, Z)+e^- \rightarrow (M, Z-1)$ reaction energy. Because of the same input isotope and same reaction end product, the difference between E_b and E_{ec} must correspond to the mass difference of the incoming particles. We may therefore determine the e_n^- mass from the following equation:

$$m_{en}c^2 - m_e c^2 = E_b - E_{ec} \tag{6.6.1}$$

where m_{en} is the free nuclear electron mass, and m_e is the ordinary electron mass.

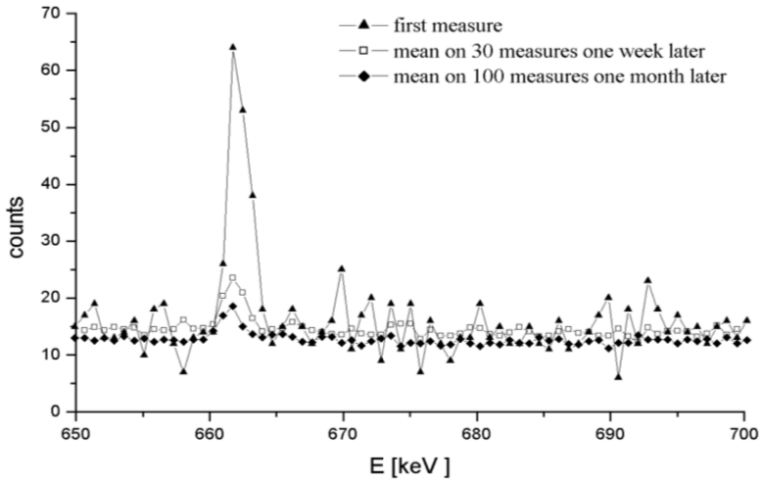

FIGURE 6.6.1. The gamma peak corresponding to a nuclear electron capture by ^{58}Ni. Measurement data from [**3**].

6.6.1. Nuclear electron capture by ^{58}Ni. The authors of [**3**] applied hot hydrogen treatment to a nickel metal. They observed unexpected gamma emission from hydrated nickel, and could not explain the source of the obtained gamma peak[1]. As shown in figure 6.6.1, this gamma peak is at 661.5 keV. At the same time, the authors of [**3**] also report observing the emission of neutrons, at low intensity. Since air always contains water vapor, a presence of e_n^- particles spontaneously generates neutrons via the $p^+ + e_n^- \rightarrow n$ reaction. We therefore interpret the origin of the gamma peak shown in figure 6.6.1 as e_n^- capture by certain nuclei.

The ^{58}Ni isotope of nickel is capable of e_n^- capture via the $^{58}Ni + e_n^- \rightarrow {}^{58}Co$ reaction. According to figure 6.6.1, the binding energy of the e_n^- capture is E_b=661.5 keV. In the case of an ordinary electron, the $^{58}Ni + e^- \rightarrow {}^{58}Co$ reaction is endothermic by E_{ec}=-381.6 keV. Because of the same reaction end product, the difference between E_b and

[1]One co-author of this book (Giorgio Vassallo) has been personally observing this experiment, and testifies the authenticity of the gamma peak shown in figure 6.6.1.

E_{ec} must correspond to the mass difference of the incoming particles. We may therefore determine the e_n^- mass from the following equation 6.6.1: it yields 1554 keV for the e_n^- mass.

While some e_n^- leptons produce the 661.5 keV peak via the $^{58}Ni + e_n^- \rightarrow {}^{58}Co$ reaction, most will simply decay. The decay of e_n^- leptons produces energetic electrons, and the intensity of their braking radiation must be proportional to the concentration of e_n^- leptons. This anticipated braking radiation signature is indeed observable in figure 6.6.1: the radiation count of "t_0 + 1 week" measurement is higher at all frequencies than the radiation count of "t_0 + 1 month" measurement, and this difference correlates with the 661.5 keV gamma peak height.

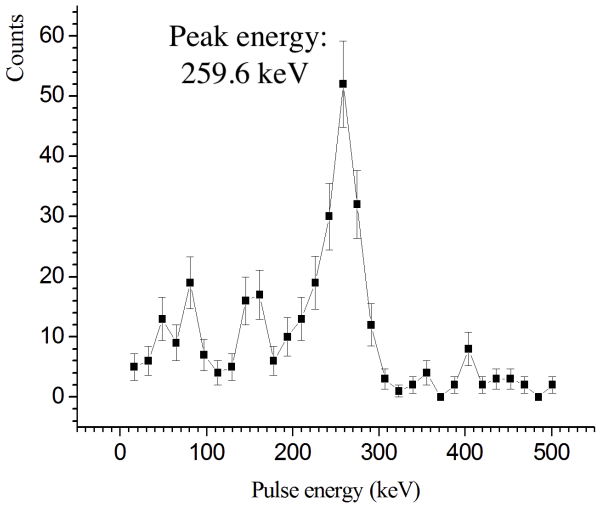

FIGURE 6.6.2. The gamma peak corresponding to a nuclear electron capture by a proton. The measurement methods are described in section 6.8.

6.6.2. Nuclear electron capture by ^{1}H. We found a second unexpected gamma emission peak during experiments on water vapor under high voltage spark discharges. The measurements were done under air atmosphere, and a shielded chamber was employed to minimize the background noise. The experimental details are given in section 6.8. This experiment is in fact a laboratory analogue of a natural lightning discharge. The physical processes during lightning discharges have been rather well studied, and several authors noted the production of neutrons by lightnings [**4, 5, 6**]. The author of [**5**] discusses similar neutron production by artificial lightning discharges in the laboratory. In our experiment, the produced neutrons are observed via the decay of ^{41}Ar, which originates from the capture of produced neutrons via the $^{40}Ar + n^0 \rightarrow {}^{41}Ar$ reaction. The details of this ^{41}Ar-based neutron observation are described in section 6.8.

Such observation of a neutron emitting process yet again signals the possible presence of e_n^- particles as well, as excess neutrons can be produced via the $p^+ + e_n^- \rightarrow n$ reaction. We therefore interpret the origin of the gamma peak shown in figure 6.6.2 as e_n^- capture by some nucleus. This interpretation is further corroborated by a time correlation analysis between the spark discharges and gamma photon emissions, which shows that the peak of figure 6.6.2 occurs right after each spark discharge, and has microsecond scale duration. The details of this time correlation analysis are given in section 6.8. Therefore the gamma peak cannot originate from any radioactive isotope contamination. Such short duration of the gamma peak emission is characteristic of a free e_n^- particle's short half-life.

Protons are the main electron capture capable nuclei in our experiment, and therefore the capture of nuclear electrons may be written as $p^+ + e_n^- \rightarrow n$. Figure 6.6.2 shows the measured gamma peak, which implies E_b=259.6 keV binding energy between a proton and a nuclear electron. For ordinary electrons, the $p^+ + e^- \rightarrow n$ reaction is endothermic by E_{ec}=-782.4 keV. We again use equation 6.6.1 to calculate the nuclear electron mass, and obtain 1553 keV.

A precise estimation of the $\mathbf{e_n^-}$ input mass: both measurements of this section show the e_n^- mass being in the 1553-1554 keV range, which cannot be a coincidence. The measurement described in section 6.6.1 employs a high-resolution gamma spectrometer, and shows 1554 keV e_n^- mass. Our precise result for the e_n^- mass is therefore $m_{en}c^2$=1554 keV. We emphasize that this is the input mass, prior to nuclear capture. In the next chapter we examine the captured nuclear electron mass.

6.7. An estimation of the nuclear electron half-life in free-particle state

In its free particle state, the nuclear electron must be a short-lived particle, otherwise it would have been discovered already. In order to determine its half-life, we must find photographed tracks showing a 1.5 MeV particle decaying into an electron.

At the JINR institute in Dubna, a group led by Vladimir A. Nikitin analyzed pair creation tracks in a bubble chamber, where particle-antiparticle pairs were generated from energetic photons [**7**]. Upon the analysis of 7000 such tracks, the authors of [**7**] found 47 anomalous lepton tracks. The analysis of these tracks revealed that they are produced by 4-10 MeV mass particles, that eventually decay into an electron or positron. Such a lepton is yet another electron-like particle that has been previously unknown. In two cases, the decay event was captured on the track photo. Figure 6.7.1 shows such a particle pair creation event and the subsequent decay of the negatively charged lepton particle. As can be seen in figure 6.7.1, the decay process is actually a two-step decay, and an electron is produced upon the second decay step. Since this intermediate lepton mass is between 4 and 0.5 MeV, its track is most probably an e_n^- track.

The final electron track is a small circle at end of the lepton track. The bubble chamber is under 1.5 T magnetic field, and thus we can calculate the electron's momentum from its track radius: its track data yields 1.925 MeV/c momentum. Our aim is to identify the half-life of the short-lived intermediate particle.

As can be observed in figure 6.7.1, the track of the intermediate e_n^- particle has three times higher radius than the electron track, and thus its momentum is p=5.8 MeV/c. At p=5.8 MeV/c momentum, the total energy of a 1.55 MeV mass particle is 6 MeV. This indicates a Lorentz boost factor of 4. Because of this high kinetic energy, the intermediate e_n^- speed is close to the speed of light. We can thus make an order of magnitude estimation of its half-life. Considering its track length of about 1.5 cm, it decays after 5×10^{-11} seconds in the laboratory frame. Taking into account the Lorentz boost factor of 4, the e_n^- half-life is in the range of 10^{-11} seconds.

The above described two-step decay process is further corroborated by the bubble chamber photograph shown in figure 6.7.2. Here, the positively charged lepton decays into a lighter intermediate particle, which we identify as e_n^+. The produced e_n^+ is attracted to electrons, and collides with two electrons along its path, transferring kinetic energy to them. Since this e_n^+ particle does not leave any track after its second collision, it has transferred most of its kinetic energy to an electron in that collision. In-between these two electron collisions, the track length of this intermediate particle is similar as in figure 6.7.1, confirming our half-life estimate.

The estimated $\sim 10^{-11}$ s e_n^- half-life is highly probable. To fully confirm it, we would need to know with certainty that we are looking at e_n^- particle tracks.

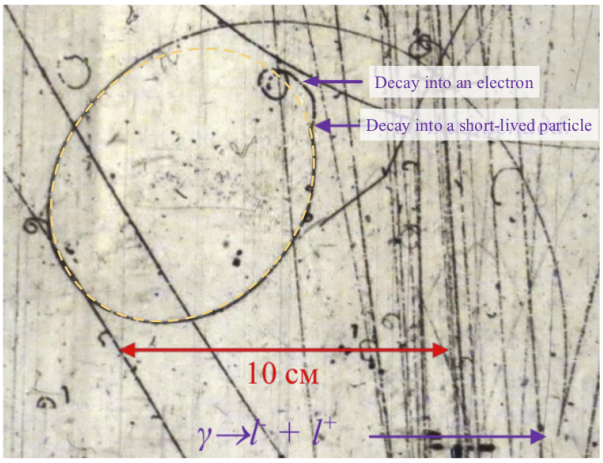

FIGURE 6.7.1. Heavy lepton pair creation in a bubble chamber. A lepton-antilepton pair is created at the bottom right corner. The other two purple arrows indicate the two decay events. The yellow dashed ellipse shows the elliptic track fitting of the negatively charged lepton. The circular track radius of the short-lived intermediate particle is three times the final electron's track radius. Photograph provided by V. A. Nikitin.

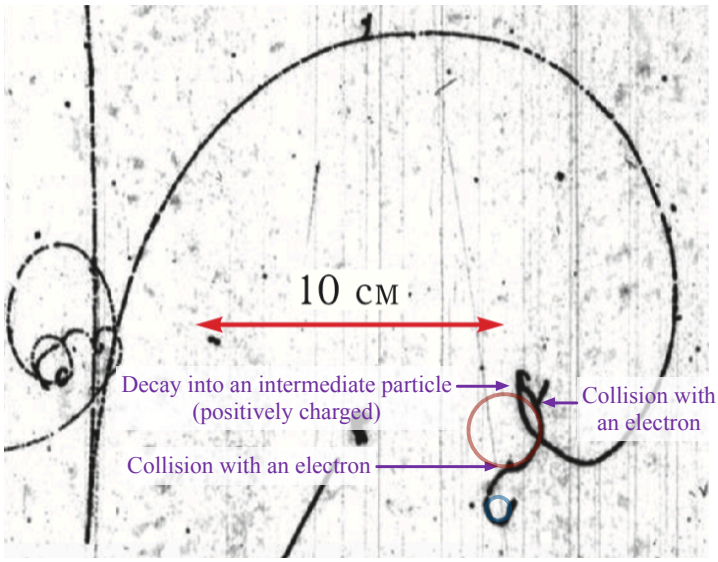

FIGURE 6.7.2. The lepton-antilepton pair is created at the bottom left corner, and the photograph shows the track of the positively charged particle. It decays into a 1.5 MeV intermediate particle, which collides with two electrons along its track. Reproduced from [**7**].

6.8. Experimental methods

Figure 6.8.1 illustrates the experimental setup for nuclear electron mass measurement. The electrode gap with a voltage of 20 kV is placed in a jet of finely dispersed drops of distilled water, supplied from the humidifier by an air stream. This jet of fine droplets is created by high-frequency mechanical vibrations. The pressure in the discharge zone is equal to atmospheric pressure. The discharge gap electrodes are located along the flow of a water-air jet of fine droplets. The flow moves from the cathode to the anode. After passing through the discharge zone, the water-air jet is directed to a ventilation tube, and is released into the atmosphere.

A gamma spectrometer is located above the discharge gap, and consists of a NaI crystal and a Photo-Electron Multiplier (PhEM). The spectrometer was calibrated by two peaks of the ^{241}Am isotope, which emits gamma rays at 26.3 keV and 59.6 keV energies. These instruments are placed in a lead box with a volume of 15×15×15 cm^3, assembled from 5 cm thick lead blocks.

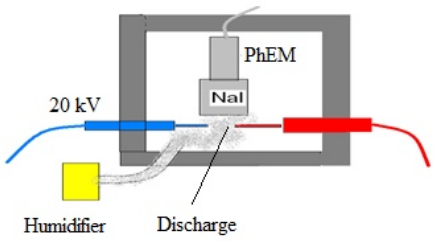

FIGURE 6.8.1. The experimental setup for recording gamma radiation during spark discharges in a water-air environment.

By placing the spectrometer and the discharge gap together into a lead box we reduce the gamma background signal in by 40 times, and thus significantly increase the signal-to-noise ratio. Figures 6.6.2 and 6.8.2 show the histogram of gamma spectra, which were recorded for 55 seconds. The gamma ray energy is shown along the abscissa axis. Along the ordinate axis, the number of pulses of electromagnetic radiation with a given energy are shown. A peak with an energy of 259.6 keV is clearly visible on figure 6.8.2. At that 259.6 keV energy, 53 pulses were registered in 55 seconds. When the same spark discharges were done in dry air atmosphere, i.e. without a jet of fine water droplets, no gamma signals were detected above the background.

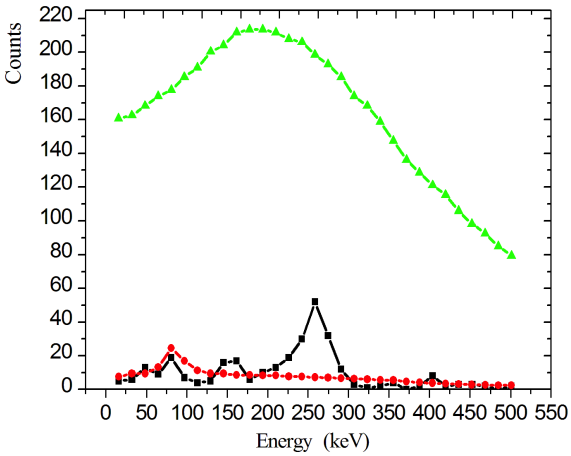

FIGURE 6.8.2. A comparison of gamma spectrograms. The black curve was recorded during a 20 kV spark discharge in water-air environment with the recorder located in a lead box, the red curve is the background signal on the recorder located in a lead box while the discharge is turned off, the green curve is the background signal on the recorder located outside the lead box while the discharge is turned off.

Figure 6.8.2 shows that the background level inside the lead chamber (red curve) is about 10 times lower than the registered peak signal. To the left of the 259 keV peak, another gamma peak with energy ranging from 125 to 175 keV is visible. This side peak

provides additional confirmation that the 259 keV peak value is correct, since it is the Compton shoulder of an electron-scattered gamma ray quantum, with the incoming energy of 259 keV.

The green curve of figure 6.8.2 shows the gamma background in the laboratory area outside the lead chamber. The background outside the lead chamber is about 190 pulses per 55 seconds at 259 keV energy, which exceeds by 3.4 times the peak of the black curve. Therefore, the use of lead box enclosure is essential.

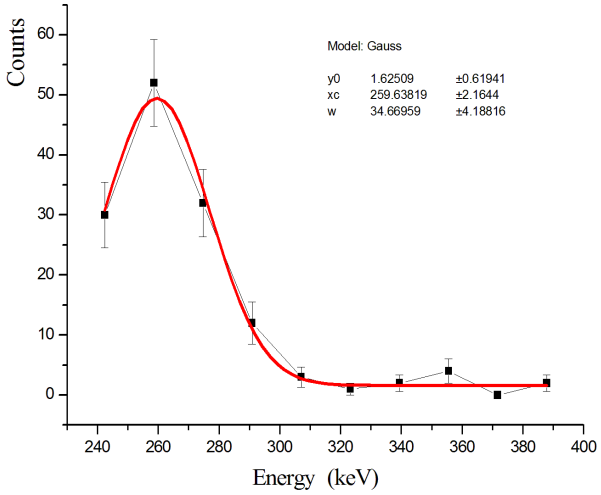

FIGURE 6.8.3. The normal distribution curve along the right branch of the 259.6 keV peak. $y0$ is the zero level of the Gaussian along the ordinate axis, xc is the location of the center point, and w is the mean square deviation.

We now address the statistical analysis of the distribution shown in figure 6.6.2. A direct statistical analysis of figure 6.6.2 data is complicated by the fact that the NaI crystal has poor spectral resolution. To the left of the 259 keV peak is the Compton shoulder, which distorts the normal distribution of the main peak. Figure 6.8.3 shows the right branch of the 259 keV peak, which is located far from the Compton peak. This allows us to reasonably apply the normal distribution statistics to the ensemble of experimental points. The red curve shows a normal distribution fitted to the experimental points[2]. It can be seen that the experimental distribution is well approximated by a normal curve centered at 259.6 keV, with a mean squared deviation of 34.7 keV^2. We note that the standard deviation in our experiment is larger than the ± 1 keV deviation shown in figure 6.6.1, which was recorded by a higher precision gamma spectrometer. Insofar as the gamma peaks of figures 6.6.1 and 6.6.2 are signatures of analogous e_n^- capture phenomenon, we can take the higher precision of ± 1 keV as the error margin of e_n^- mass measurement.

We also investigate the time correlation between the gamma ray signals and the electric discharge sparks. To do this, we use an oscilloscope to register gamma ray signals. In addition, a small radio antenna was also used, located at a distance of 0.5 m from the lead chamber. The oscillograms coming from the two channels of the oscilloscope are jointly analyzed: i.e. the signal from the PhEM and the signal from the radio antenna. The result of this experiment is a set of oscillograms obtained on the oscilloscope by repeatedly registering short pulses from the NaI detector and from the radio antenna (fast frame mode). The oscillogram recording was triggered when two conditions were

[2]this normal distribution was obtained using the Origin6 software

met by the gamma signal: i) the duration of the signal is more than 1.5 microseconds, and ii) the signal amplitude is more than 50 mV[3]. Such double condition for starting the oscillogram recording confidently ensures that it starts when the gamma ray quantum passes through the NaI crystal.

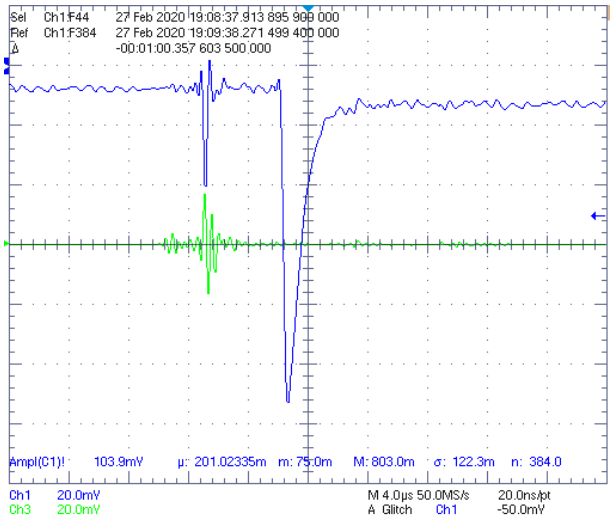

FIGURE 6.8.4. An exemplary oscillogram. The blue curve is the PhEM signal, and the green curve is the radio antenna signal. The large negative dip is the signature of a gamma ray quantum.

Spark discharges generate a bunch of high-frequency oscillations, which were recorded by the radio antenna located 0.5 m away. Each oscillogram shows 25 microseconds before and after the trigger condition. Considering that the sparking frequency is about 10 discharges per second, the probability that a gamma ray quantum and an electromagnetic oscillation signal would both randomly show up in one oscillogram is estimated to be 5×10^{-4}. That is, if the discharge and the formation of a gamma ray quantum are not correlated, then it would take several thousand oscillograms in order to see both signals (i.e from the antenna and from the PhEM) registered in the same oscillogram.

An exemplary oscillogram record is shown in figure 6.8.4. The green curve shows the signal from the radio antenna; it shows the registration of electromagnetic field oscillations at -9.6 microseconds. It is at this moment that an electric discharge occurs between the two electrodes. These oscillations are almost completed after 5 microseconds, i.e. this is the duration of the spark discharge. The blue curve shows the signal of PhEM; it also reacts to the electromagnetic field like the radio antenna, and shows an oscillating signal at the same time. But 6 microseconds after the spark signal a unipolar negative signal appears on the blue curve, typical for a gamma ray quantum. As explained in the previous paragraph, the probability of a random coincidence between these two signal types is extremely small. We found similar correlated signals on 26% of the recorded oscillograms. Keeping in mind that the oscillogram recording is triggered by any >200 keV gamma ray, i.e. not only the peak signal, we obtain a causal relationship between the spark discharges and the 259 keV gamma ray signal.

In summary, the above described analysis proves that the 259 keV gamma peak is statistically significant and it is correlated with spark discharge events in the water-air medium.

Figure 6.8.5 shows a gamma spectrum measurement made half hour after a spark-discharge experiment run. This spectrum has one gamma peak, at approximately 1.3 MeV

[3]this roughly corresponds to a gamma ray quantum of 200 keV

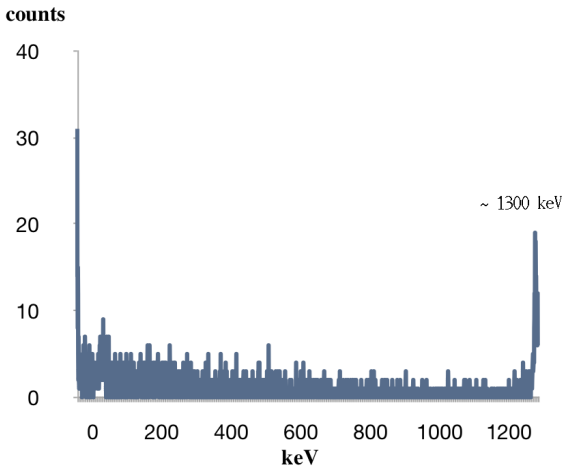

FIGURE 6.8.5. The gamma spectrum measured 30 minutes after a spark-discharge experiment run.

energy. There is only one radioactive isotope that has such radiation signature: it is ^{41}Ar. ^{40}Ar is present at 1% concentration in the atmosphere, and it has several orders of magnitude higher neutron capture cross section than nitrogen or oxygen. If spark discharges generate neutrons, they are preferentially captured by ^{40}Ar according to the $^{40}Ar + n^0 \rightarrow {}^{41}Ar$ reaction. The resulting ^{41}Ar isotope has 110 minutes half-life, and remains enclosed by the lead shielding box. The gamma spectrum of figure 6.8.5 thus shows the signature of ^{41}Ar production, which demonstrates neutron production during spark-discharges.

We note that this experiment is difficult to replicate because it requires not only thick radiation shielding, but also numerous experiment runs. Presently we do not know the reason why the observed gamma peak appears only in a certain fraction of experiment runs.

6.9. Conclusions

In conclusion, the nuclear electron concept is compatible with fundamental physics principles, does not violate energy conservation, and it is based on a direct interpretation of nuclear measurements. Applying the Heisenberg uncertainty principle, we modeled the neutron being in a single particle state most of the time, and in a proton + nuclear electron state a tiny fraction of time. We found that this model is more reasonable than assuming the non-existence of proton + nuclear electron state.

The nuclear β-decay is identified with the nuclear electron's decay into an ordinary electron plus neutrino radiation, and the calculated energy distribution of decay products matches the nuclear electron's radial oscillation pattern. Nuclear stability requires a sufficiently high binding energy of the nuclear electron, so that its decay into an electron would not be exothermic. We estimated the exponential wavefunction tail of a radially oscillating nuclear electron, and experimentally demonstrated its existence in β-decaying heavy nuclei. The existence of a giant nuclear halo in certain heavy isotopes is a new result, unexpected by preceding theories.

We measured the nuclear electron mass to be 1554 keV in its short-lived free-particle state.

This chapter lays the foundation for a rational discussion of nuclear structures. In the next chapter, we focus on the neutron's single particle aspect, and map out its internal

structure.

Acknowledgements: The authors thank the Baltic Scientific Instruments company for the gamma spectrum measurements.

Bibliography

[1] The DOE/NSF Nuclear Science Advisory Committee "The Frontiers of Nuclear Science - A Long Range Plan" (2007)

[2] A. Kovacs, G. Vassallo, A. O. Di Tommaso, and F. Celani "What is inside an electron: the physics of electromagnetic waves that are perceived as quantum mechanical waves", Zitter Institute (2025)

[3] S. Focardi et al "Evidence of electromagnetic radiation from Ni-H Systems", proceedings of the ICCF-11 International Conference on Condensed Matter Nuclear Science, Marseille, France (2004)

[4] A. V. Gurevich et al "Strong Flux of Low-Energy Neutrons Produced by Thunderstorms", Physical Review Letters, Volume 108 (2012)

[5] L. P. Babich "Thunderstorm neutrons", Physics-Uspekhi, Volume 62.10 (2019)

[6] T. Enoto et al "Photonuclear reactions triggered by lightning discharge", Nature, Volume 551 (2017)

[7] M. Ch. Anikina, V. A. Nikitin, V. S. Rikhvitskiy "Search for New Charged Particle in Mass Interval 2–100 MeV", Communication of the Dubna Joint Institute for Nuclear Research, 1-2022-62 (2022)

CHAPTER 7

The neutron structure is deduced via a direct interpretation of experimental data

Andras Kovacs[1]
[1] ExaFuse. E-mail: andras.kovacs@broadbit.com

ABSTRACT. While experimental physics progressed tremendously since the 1970s, the neutron model has remained essentially unchanged. Motivated by developments in both experiments and theory, we propose that the initial neutron decay step is not the emission of an 80 GeV mass boson particle, but the decay of a much lighter lepton particle.

Historically, investigations of deuteron photo-dissociation led nuclear scientists to assume that no electron-like particle is associated with neutron decay. We therefore re-examine these experiments in section 7.2. We demonstrate that deuteron photo-dissociation leads to $2p^+ + e^-$ products at high photon energies. Our calculations show why a deuteron always breaks up into $p + n$ particles at <3 MeV photon energy.

Aided by the insights built up over the preceding chapters, we explore the neutron's internal structure in section 7.4. We deduce the neutron's internal structure via a direct interpretation of experimental data.

7.1. Motivation

7.1.1. A brief overview of meson models. Before the 1970s, most scientists viewed the proton as an elementary particle. Starting from the 1970s, scientists working at high energy particle colliders proposed that protons and neutrons are not elementary particles, but comprise smaller sub-particles. According to their model, a proton and a neutron both comprise three quark sub-particles. The existence of quarks has been suggested initially in the 1960s, based on the theoretical efforts by Gell-Mann to model baryons and mesons [**3**], which were observed in a great variety during high energy nuclear experiments. While Gell-Mann's original quark theory required the F_2 momentum distribution to peak at $x = \frac{1}{3}$, reference [**6**] demonstrates that this is not the case because the experimentally observed F_2 peak is at $x = \frac{1}{9}$. This deviation from the required peak at $x = \frac{1}{3}$ was explained away via the hypothesis that the three quarks originally thought to form the proton are the so-called "valence quarks", which are swimming in the background of "sea quarks" [**4**]. These so-called sea quarks are a collection of quark-antiquark pairs, radiated by the three valence quarks. However, the calculations of 1970s still showed that the valence quarks together with the sea quarks only accounted for 54% of the proton's momentum [**2**]. A further hypothesis was added to supplement the momentum shortfall of the quarks; chargeless particles called gluons were introduced into the proton model [**5**]. Since gluons have no electric charge, the thinking was that they are there, but the electrons probing the proton in deep inelastic scattering cannot see them. These hypothesized gluons were assigned the missing proton momentum, and the resulting proton model became the quark-gluon model that it is today. But even with this model of "valence quarks" swimming in the background of "sea quarks and gluons", there seemed to be an angular momentum deficit with respect to the measured angular momentum of the proton, and therefore the presence of "virtual strange quarks" was also postulated in the 1990s [**7**].

Although the quark-based model was inspired by the great variety of mesons, the proposed quark masses do not add up the masses of observed mesons. According to quark proponents, this is explained by a negative binding energy between quarks: any particle's valence quark masses are only a small percentage of the total particle mass, with the bulk of the particle mass coming from particles which represent the binding force: i.e. virtual quarks and gluons. Moreover, the valence quark : virtual quark : gluon mass ratio is allowed to vary from particle to particle in order to match the observed masses. Now what is the physical meaning of negative binding energy? By definition, negative binding energy means a meta-stable bound state. This model implies that individual quarks should be easily observable upon the break-up of their meta-stable binding. Quark proponents therefore also postulated that the meta-stable bonds between quarks can never be dissociated. The energy balance was also turned upside down for annihilation reactions: the annihilation between the hypothetical u quark and d anti-quark is postulated to start by an 80 GeV endothermic step. In summary, it appears that the quark-based proton model has become embraced without any direct evidence, and maintaining it requires a forever expanding list of postulates.

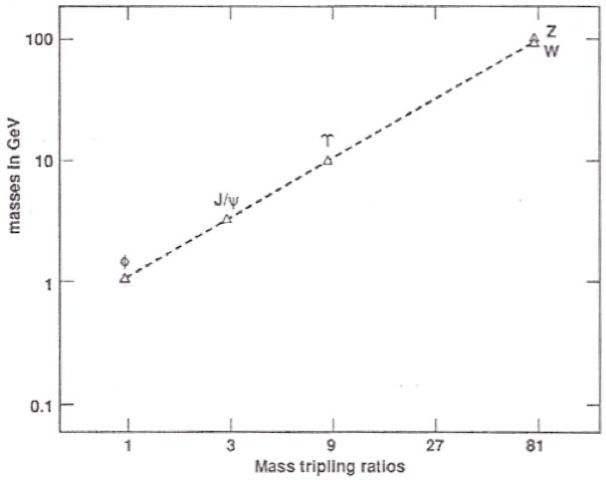

FIGURE 7.1.1. The mass tripling pattern of certain mesons, reproduced from [**11**].

We developed an electromagnetic proton model in chapter 3, which restores proton's elementary particle status. It gives tangible answers to questions, such as: what is the proton made of?, what generates the proton's spin?, what generates the proton's anapole magnetic moment?, and what is the meaning of the experimentally measured proton radius? While the preceding quark-based proton model violates Maxwell's equation via the so-called "renormalization" procedure and proposes complicated interactions among experimentally non-observable virtual particles, which are referred to as "sea quarks" and "gluons", our proton model respects Maxwell's equation and does not require the presence of energy conservation violating virtual particles. This proton model matches all data in high energy electron-proton scattering experiments, without employing postulates or hidden parameters.

The proton's elementary particle status implies that the neutron should comprise a proton and a negative elementary charge. What remains is to map out the Zitterbewegung structure of the neutron's positive and negative elementary charges.

Regarding mesons, an alternative modeling approach is to look for simple patterns of their mass variations. As illustrated in figure 7.1.1, some meson particles form a geometric mass-tripling pattern [**11**]. Coincidentally, our present work reveals an analogous

mass-tripling pattern. We already identified in chapter 6 that the nuclear electron is approximately three times heavier than an ordinary electron. We shall refer to the mass-tripled electron as the e_n^- particle in our work, where the "n" index stands for "nuclear". Continuing with this mass-tripling, we arrive at the mass difference between the charged π^- and neutral π^0 particles. Assigning this mass difference to a weakly bound e_π^- lepton, the emerging pattern is summarized by table 1. This alternative model suggests the existence of $e_\pi^- \to e_n^-$ and $e_n^- \to e^-$ decays. Such lepton decays indeed show up in neutron decay or in $\pi^- + p^+ \to \pi^0 + n^0$ interaction, both of which are well-known nuclear reactions:

$$n^0 \longleftrightarrow \left(p^+ + e_n^-\right)_{bound} \to p^+ + e^- + \bar{\nu}$$

$$\pi^- + p^+ \longleftrightarrow \left(\pi^0 + e_\pi^-\right) + p^+ \to \pi^0 + \left(e_n^- + p^+\right)_{bound} + \bar{\nu} \to \pi^0 + n^0 + \bar{\nu}$$

The main reason why this mass tripling pattern was not obvious from the start is the binding energy of the $(p^+ + e_n^-)_{bound}$ state, which impacts the neutron-proton mass difference.

Recalling the precise 1.554 MeV e_n^- mass measurement in chapter 6, the ratio between the e_n^- and e^- particle masses is 3.04. Looking again at figure 7.1.1, the specific ratio between the J/ψ and ϕ meson masses is 3.038, which is very close to 3.04. Similarly, the ratio between the Υ and J/ψ masses is also very close to this 3.04 value. Perhaps this ratio can be derived from some universal principle, which is valid for both leptons and mesons.

Lepton type	**Mass**	**Decays to**
e^-	m_e =0.511 MeV	stable
e_n^-	$m_n - m_p \approx 3 \cdot m_e$	e^-
e_π^-	$m_{\pi-} - m_{\pi 0} \approx 9 \cdot m_e$	e_n^-

TABLE 1. The electron's mass-tripling pattern.

7.1.2. A brief history of the neutron decay model. Regarding neutron decay, it was proposed in the 1970s that the nuclear beta-emission of electrons and antineutrinos is being mediated by 80 GeV mass W boson particles, i.e. an $X_Z^A \to X_Z^{A+1} + W^-(80GeV) \to X_Z^{A+1} + e^- + \bar{\nu}_e$ process, which temporarily violates energy conservation. The emission of this 80 GeV mass particle is supposedly allowed by Heisenberg uncertainty; i.e. nucleons are thought activate this uncertainty only above a specific neutron:proton ratio threshold, and keep it de-activated below that threshold. However, it seems to be a violation of the Heisenberg uncertainty principle to model it with an on-off switch.

Presently, claims about the structure and interactions of 80 GeV particles with 10^{-25} sec half-life are highly speculative. Claiming that the emission and absorption of neutrinos is mediated by 80 GeV virtual particles is a particularly extraordinary claim, and should require extraordinary evidence. However, the presence of a W boson was never experimentally observed during neutron decay.

The hypothesis of 80 GeV virtual particles is experimentally contradicted by the beta decay of the ^{163}Dy nucleus. It is known since 1992 that the ^{163}Dy nucleus beta decays in a fully stripped Dy^{66+} state, while the same ^{163}Dy nucleus is stable in a neutral atom [**12**]. Such beta decay of Dy^{66+} produces a bound state electron, which has a negative energy state with respect to a free electron. While most nuclear theorists insist that any beta decay reaction is completely independent from electromagnetism, it is clear that the electric potential is the controlling parameter of this beta decay process.

If beta decay was triggered by the formation of an 80 GeV mass W boson particle, such process would not care about the presence or absence of orbital electrons. Since the presence or absence of orbital electrons is the actual control parameter of the ^{163}Dy beta decay, it is impossible that any W boson particle is involved in this process.

A similar experimental contradiction is also presented by the beta decay of the ^{210}Bi nucleus. ^{210}Bi beta decays in its ground state, but remains stable in its 271 keV excited state, which is a long-lived excitation state. If beta decay was triggered by the formation of an 80 GeV mass W boson particle, such process would not care about the presence or absence of a nuclear excitation which has 5 orders of magnitude lower energy.

Based on these shortcomings, it is reasonable to consider an alternative model of neutron decays. A more preferable neutron decay model avoids experimental paradoxes and does not violate energy conservation. We therefore interpret nuclear β-decay as the decay of nuclear electrons, which were introduced in chapter 6.

7.2. Signatures of nuclear electrons in deuteron photo-dissociation

7.2.1. The historic interpretation of deuteron photo-dissociation. After Chadwick's discovery of the neutron in 1932, there were a lot of discussions whether it is an elementary particle or a hydrogen-like atom formed from electron and proton [**1**]. For example, Heisenberg and Rutherford were among those who argued that Chadwick's particle is a small hydrogen atom. Pauli however stated that the neutron should be viewed as an elementary particle. To decide who is right, Chadwick's team irradiated deuterons by 2.62 MeV photons, and saw deuterons splitting into a proton and a neutron, without the emission of any electron-like particle. Consequently, most nuclear physicists rejected the nuclear electron concept. With the discovery of the neutron's magnetic moment in 1940, most scientists also rejected Pauli's elementary particle neutron concept, as their elementary particle model assumed the absence of internal charge distribution.

The first deuteron photo-dissociation experiments were performed by Chadwick and Goldhaber in 1935 [**15**]: they passed 2.62 MeV gamma rays, emitted by a thorium source, into deuterium gas. The dissociation generated energetic protons with mean proton energy of 0.185 MeV. By conservation of momentum, the other released particle must carry away the same momentum. Since neutrons have about the same mass, a dissociation into a proton and a neutron means 0.185 MeV kinetic energy of the generated neutrons. These values imply a deuteron binding energy of $2.62 - 2 \times 0.185 = 2.25$ MeV. This value matches the experimental deuteron binding energy, measured by photon energy detection upon proton-neutron reactions. Thus the deuteron photo-dissociation into a proton and a neutron has been proven. Later work showed that the photon energy threshold for deuteron photo-dissociation is 2.26 MeV.

The observation of only proton plus neutron reaction products at this 2.62 MeV photon energy was historically thought to be a proof for the absence of electron-like sub-particles, based on the idea that energetic photons should primarily ionize away any light particles. The implicit assumption here is that an electron-like particle would more readily interact with $>$2.26 MeV photons than a proton, and would thus become ionized from the nucleus. In the following, we look into this possibility in the light of modern experimental data.

7.2.2. Compton scattering in nuclear context. At high photon energy, Compton scattering becomes the dominant photo-ionization process of ordinary electrons. Therefore, one cannot neglect the role of Compton scattering in deuteron photo-dissociation. Any particle's Compton scattering cross-section is given by the Klein-Nishina formula. 20-100 MeV photons have much less energy than the proton mass, and thus protons' Compton scattering is negligible in this energy range. On the other hand, this energy

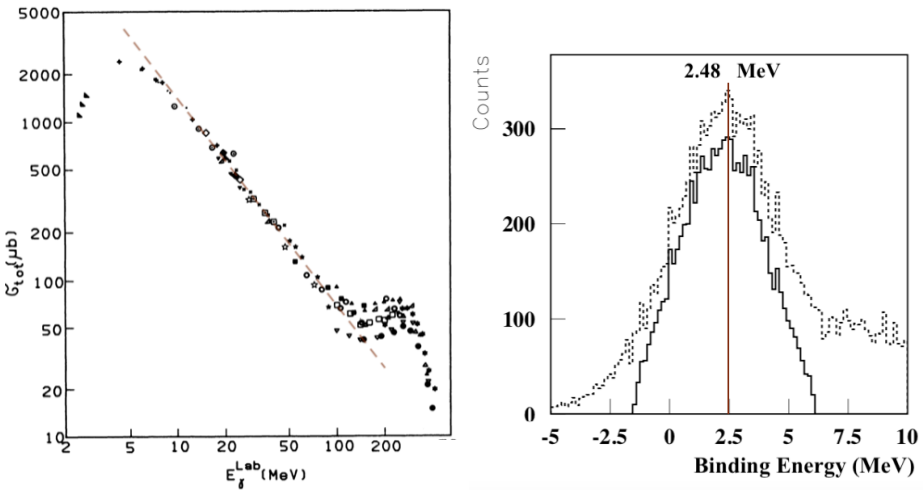

FIGURE 7.2.1. Deuteron photo-dissociation by high-energy radiation. Left: the p^+ counting based photo-dissociation cross section (microbarns), as a function of photon energy, reproduced from chapter 6 of [**17**]. Right: the binding energy among deuteron constituents, measured upon photo-dissociation by 30-50 MeV photons, reproduced from [**18**].

range is much higher energy than either the e^- or e_n^- mass. Therefore, according to the Klein-Nishina formula, the e^- and e_n^- Compton scattering cross sections vary at the same rate with respect to the photon energy. Within a certain photon energy range, if deuteron photo-dissociation is dominated by the negative charge's Compton scattering process, then this Compton scattering cross section can be approximated by the total deuteron photo-dissociation cross-section.

The electron's Compton scattering cross-section values at 20 and 100 MeV photon energy are shown in table 2, based on the data of reference [**16**]. Regarding the e_n^- particle, its Compton scattering cross-section is identified with $\frac{1}{2}$ of the deuteron photo-dissociation cross section in the 20-100 MeV photon energy range. A $\frac{1}{2}$ multiplier must be applied to the p^+ counting based experimental cross-section measurement because the ${}^2H^+ \rightarrow 2p^+ + e_n^-$ Compton scattering produces two protons. The obtained values at 20 and 100 MeV photon energy are displayed in the last column of table 2. As expected, the e^- or e_n^- cross sections vary at a similar rate with respect to the photon energy, which is a signature of Compton scattering.

	$\boldsymbol{e^-}$ (Xe)	$\boldsymbol{e^-}$ (Pb)	$\boldsymbol{e_n^-}$ (${}^2H$)
E_γ=20 MeV	14.9 mb	13.7 mb	0.29 mb
E_γ=100 MeV	2.02 mb	1.87 mb	0.035 mb
σ_{20}/σ_{100}	**7.4**	**7.5**	**8.3**

TABLE 2. A comparison between the e^- and e_n^- Compton scattering cross sections at 20 and 100 MeV photon energy. The millibarn values are the Compton scattering cross-sections of the particles identified in the first row.

When the negative elementary charge is removed via Compton scattering, the deuteron breaks up via the ${}^2H^+ \rightarrow 2p^+ + e_n^-$ pathway. Writing this process as ${}^2H^+ \rightarrow p^+ + n \rightarrow 2p^+ + e_n^-$, one may see that such three-body break-up requires $E_{b,D} + E_{b,n}$ energy input, where $E_{b,D}$=2226 keV is the ${}^2H^+ \rightarrow p^+ + n$ dissociation energy, and $E_{b,n}$ is the $p^+ - e_n^-$ binding energy within the neutron. As shown in the right side of figure 7.2.1, the binding

energy which was measured upon deuteron photo-dissociation by 30-50 MeV photons peaks at $E_{b,D} + E_{b,n}$=2.48 MeV energy, and not at 2.23 MeV energy. The two curves peaking at 2.48 MeV only differ in the applied signal filtering condition, which is explained in reference [**18**]. This data reveals that the $p^+ - e_n^-$ binding energy is $E_{b,n}$ ≈2.48-2.226 MeV=254 keV; this data well matches the $E_{b,n}$ ≈259 keV value deduced in chapter 6.

The above data indicates that Compton scattering is the dominant photo-dissociation process above 20 MeV photon energy. In this photon energy range, the $e^- + e^+$ pair creation process also has a high cross-section. Up to now, experimentalists assumed that any detected electrons originate from pair creation events, thereby not noticing the electrons originating from the deuteron break-up.

Applying the Klein-Nishina equation with 1.5 MeV nuclear electron mass and 2.48 MeV dissociation energy threshold, we find that the Compton scattering cross section falls to zero near 3.2 MeV photon energy. Below 3.2 MeV photon energy, the only remaining dissociation pathway is the photoelectric process. We thus look into the photoelectric reactions in the following paragraphs.

7.2.3. The photoelectric effect on nuclear electrons. During the chemical photo-dissociation of a H_2 molecule, the radiation field can either break the H_2 molecule into two H atoms [**19**] or it can ionize the H_2 molecule into an H_2^+ ion and an electron. Analogously, the nuclear photoelectric effect may yield either the ${}^2H^+ \rightarrow p^+ + n$ or the ${}^2H^+ \rightarrow p^+ + p^+ + e_n^-$ reaction pathway. We estimate the relative probability of these two pathways.

We already established in chapter 6 that the neutron appears as a single particle most of the time, i.e. the deuteron can be treated as a $p^+ + n$ system in the first approximation. The photoelectric effect then breaks up a deuteron mostly into $p^+ + n$ products. We also established in chapter 6 that the neutron appears as $p^+ + e_n^-$ system in a small fraction of the time. Analogously, the deuteron appears as a $p^+ + p^+ + e_n^-$ system in a small fraction of the time. Let us see how the photoelectric effect impacts a $p^+ + p^+ + e_n^-$ system.

To calculate the photoelectric effect on a $p^+ + p^+ + e_n^-$ system, we must define a three-body wavefunction. A reasonable wavefunction toy-model is to consider the three-body wavefunction being a Gaussian function of the sub-particles' distance:

$$\psi = De^{-\frac{\beta}{2}(\mathbf{r}_{p1}-\mathbf{r}_{en})^2} e^{-\frac{\beta}{2}(\mathbf{r}_{p2}-\mathbf{r}_{en})^2} e^{-\frac{\beta}{2}(\mathbf{r}_{p1}-\mathbf{r}_{p2})^2}$$

where $\mathbf{r}_{p1}$ and $\mathbf{r}_{p2}$ denote the two protons' position, and $\mathbf{r}_{en}$ denotes the nuclear electron's position. Such a wavefunction maximizes the Shannon entropy of its sub-particles. D and β are two unknown parameters, which can be calculated from two boundary conditions: the deuteron's charge radius is 2.1 fm, and the wavefunction is normalized to a unit probability over the whole space. We thus get $\beta = \frac{1}{24}$ fm^{-2} and $D = 0.0512$ fm^{-3}. The Hamiltonian operator of light-matter interaction is:

$$H = -\sum_i \frac{q_i}{m_i} \hat{\mathbf{A}}(\mathbf{r}_i) \cdot \hat{\mathbf{p}}_i$$

where q_i, m_i, $\mathbf{r}_i$, and $\hat{\mathbf{p}}_i$ are the given sub-particle's charge, mass, position, and momentum operator, while the $\hat{\mathbf{A}}$ operator corresponds to the electromagnetic wave's vector potential.

Upon photo-dissociation into $2p^+ + e_n^-$ reaction products, the wavefunction of the final state comprises three harmonic functions of the three resulting particles. Using the above Hamiltonian, we calculate the cross-section corresponding to the deuteron wavefunctions' transition from its initial ground state into its final dissociated state. Using 1.5 MeV e_n^- mass, we obtain less than 0.01 mb cross-section at any photon energy, which is far below

the experimental photo-dissociation cross-section. In the 1930s, theoreticians expected the orange curve of figure 7.2.2 to be orders of magnitude higher than the experimental cross-section, mainly because an electron-like particle is much lighter than the other two particles. In the light of actually performing the calculation, we can see that it is the low density of states associated with an electron-like particle which causes the ${}^2H^+ \rightarrow p^+ + n$ reaction pathway to have much higher probability than the ${}^2H^+ \rightarrow 2p^+ + e_n^-$ reaction pathway.

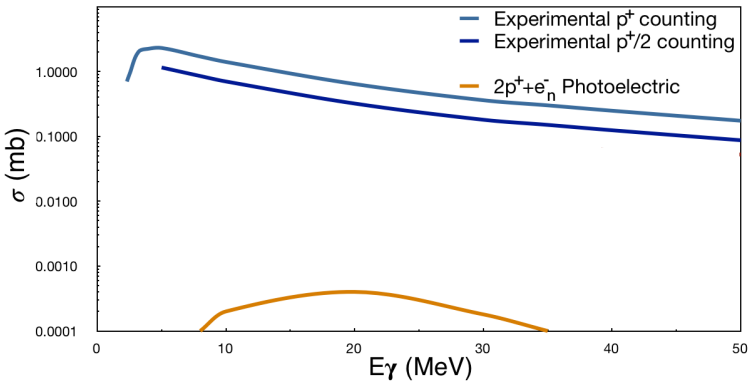

FIGURE 7.2.2. The experimental deuteron photo-dissociation cross-section (blue) and the calculated cross-section of the photoelectric ${}^2H^+ \rightarrow 2p^+ + e_n^-$ reaction (orange).

In summary, the results of sections 7.2.2-7.2.3 explain why the experimenters of the 1930s saw only $p+n$ photo-dissociation products, while working at $<$3 MeV photon energy.

7.3. Electron-emitting excited nuclei

In the following paragraphs, we go through data which demonstrate the emission of electrons from certain excited nuclei. If an electron-releasing excited state exists for an otherwise stable isotope, one may conclude that the involved nucleus contains negative elementary charges.

The ^{9}Be nucleus comprises two alpha sub-particles, and a neutron. It takes only 1665 keV to separate a neutron away from it, which is less energy than any of the ^{9}Be excitation energy levels. The energies of its lowest three excited states are shown in figure 7.3.1. It has been observed that any of these excitations break up the ^{9}Be nucleus with very close to 100% probability [**10**]. The 1684 keV and 2780 keV excitations decay by neutron emission; the remaining ^{8}Be nucleus then promptly splits into two alpha particles.

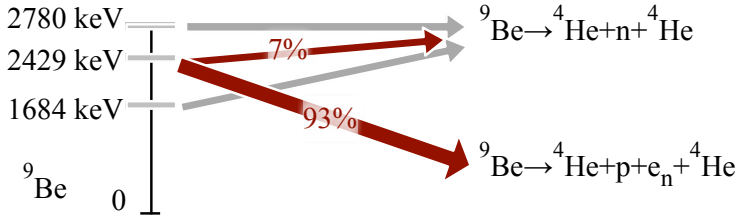

FIGURE 7.3.1. The lowest three excitation levels of ^{9}Be and their subsequent break-up reactions.

Interestingly, the 2429 keV excitation decays by neutron emission in only 7% of cases [**10**]. While, nuclear data tables do not say what break-up products emerge in the other 93% of cases, there is no other possibility than the ${}^9Be \rightarrow {}^4He + {}^4He + p + e_n$ reaction

shown in figure 7.3.1. The reasons for the impossibility of other reaction products are: i) ^{5}He and ^{5}Li do not exist, and ii) a proton separation into $^8Li + p$ would require over 16 MeV energy. Therefore, the 2429 keV excitation of ^{9}Be decays mainly by emitting a proton and an electron. Such a prompt release of an electron upon nuclear break-up demonstrates that a negative elementary charge must be present in the ^{9}Be nucleus.

In order to develop a generalized understanding of e_n^- particles' prompt nuclear emission, let us consider the β-decay process of excited nuclei. When a β-decaying isotope is in its ground state, it decays via electron emission, and the half-life of such a decay is measured in hours, days, or even years. When the same isotope is in an excited state, with the excitation level being just above the neutron separation energy, the β-decay also happens via neutron emission. This well-known process is observed in nuclear fission reactors; some of the produced fission fragments are in a long-lasting excited state, and β-decay via neutron emission. The delay between the fission event and a subsequent β-decay via neutron emission is measured in seconds or minutes. A nuclear fission reactor would in fact have uncontrollable chain reaction run-away without such delayed neutrons.

	Ground-state nucleus	**$> S_n$ excitation**	**$\gg S_n$ excitation**
β-decay type	e^- emission	n^0 emission	$e_n^- + p^+$ emission
Where is it observed?	Beta-decaying isotopes	Delayed n^0 in nuclear reactors	Fission events emitting prompt neutrinos, photo-dissociation

TABLE 3. A listing of various β-decay types, as a function of nuclear excitation level. S_n is the neutron separation energy.

We saw in section 7.2 that at moderate photon energy the main deuteron dissociation pathway is neutron release, while at high photon energy the main deuteron dissociation pathway is simultaneous $e_n^- + p^+$ release. Highly energetic nuclear excitations may β-decay via simultaneous $e_n^- + p^+$ release. Since a free e_n^- particle has very short half-life, its decay produces neutrino radiation almost instantaneously. The $e_n^- + p^+$ releasing beta decay therefore occurs in those uranium fission events that emit "prompt" neutrino radiation. These various categories of nuclear beta-decay are summarized in table 3.

7.4. Towards a deeper understanding of the neutron

7.4.1. The neutron's internal structure. Although we are still in the early stages of understanding the neutron, there is already sufficient experimental data to map out its internal constellation. On the basis of proton experimental data, we calculated the proton's internal structure in chapter 3, which is illustrated on the left side of figure 7.4.1. We derived the following proton parameter set: its major (toroidal) radius is 0.831 fm, its minor (poloidal) radius is 0.46 fm, and its Compton scattering radius is 0.0015 fm.

The proton and neutron transmute into each other and have very similar mass values; this indicates that the neutron's negative charge is imposed over a proton-like structure.

With the advancement of measurement techniques, it has become possible to directly map out the neutron's radial charge distribution. The proton versus neutron size can be compared e.g. via magnetic radius values, which have been measured for both particle types. As can be seen in table 4, the average magnetic radii differ by only 2%. These data indicate that the major (toroidal) neutron radius approximately retains the proton's 0.83 fm toroidal radius.

The mean radial distance of the neutron's negative charge can be extracted from so-called "neutron charge radius measurements". Such experiments compare the mean radial distance of the positive and negative charges, and yield -0.11 fm^2 **[20, 21]**. This

small difference matches the above-mentioned neutron magnetic radius measurements, and probably relates to the small probability of observing the e_n^- wavefunction's radial oscillation. These measurements mean that the neutron's negative charge has approximately the same Zitterbewegung radius as the toroidal proton radius: $r_- \approx 0.83$ fm.

Publication year	Mean proton magnetic radius	Mean neutron magnetic radius
1976	0.84 fm	0.87 fm
1995	0.835 fm	0.89 fm
2003	0.855 fm	0.88 fm
2012	0.86 fm	0.88 fm
2014	0.85 fm	0.86 fm
2021	0.845 fm	0.865 fm
2022	0.85 fm	0.865 fm

TABLE 4. Proton versus neutron magnetic radius measurements, as listed in [**22**].

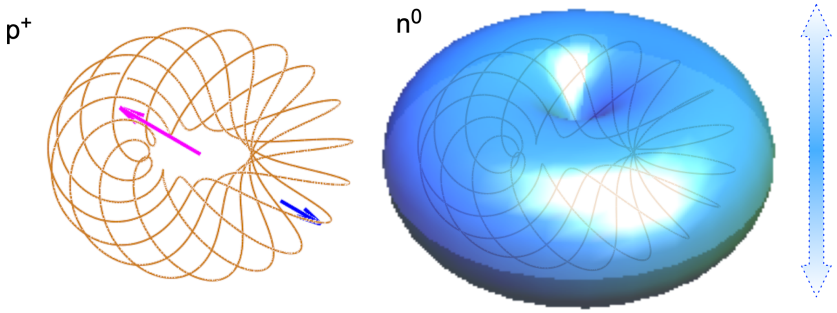

FIGURE 7.4.1. An illustration of the toroidal proton structure (left) and the neutron structure (right). The toroidal curve represents the Zitterbewegung path of the neutron's positive charge, and the blue torus represents its negative charge. The arrow on the right edge indicates the small oscillation probability of the negative charge.

A next question is to understand this negative charge's "classical radius". Let us recall from the preceding chapters that the classical particle radius is inversely proportional to the electric field energy in both electron and proton cases, and thus a measurement of this radius is a measurement of the particle mass. For the free e_n^- particle, its 1.554 MeV mass implies $2.82 \cdot \frac{0.511}{1.554}$ fm=0.93 fm "classical radius" radius, i.e. one third of the classical electron radius value.

We calculate the "classical radius" of the neutron's negative charge more precisely from magnetic moment considerations. The neutron's experimental magnetic moment value is $-1.913\mu_N$. The positive proton charge has $2.793\mu_N$ magnetic moment contribution; the e_n^- contribution is therefore $\mu_- = -4.706\mu_N$.

The nuclear electron circulates with speed c at r_-=0.83 fm radius. Without the anomalous magnetic moment contribution, its magnetic moment scales from the electron's Bohr magneton according to the $\frac{r_-}{r_{Compton}}$ ratio:

$$\mu_B \frac{r_-}{r_{Compton}} = -3.945\mu_N$$

We take its anomalous magnetic moment into account, using equation 2.4.5:

$$\mu_- = \mu_B \frac{r_-}{r_{Compton}} g = -3.945\mu_N \left(1 - \frac{r_{c-}}{2\pi r_-}\right)^{-1} = -4.706\mu_N \tag{7.4.1}$$

where g is the anomalous magnetic moment factor evaluated according to equation 2.4.5, and r_{c-} is the "classical radius" of the proton-bound e_n^- particle. We note that r_{c-} is the only unknown of the above equation, and evaluating it yields r_{c-}=0.84 fm. This is a peculiar result because $r_{c-} \approx r_-$; i.e. the neutron's negative charge circulates in such a toroidal volume whose poloidal and toroidal radii are the same. We may now summarize what we discovered about the neutron structure so far.

The internal structure of the high probability single-particle neutron state. In summary, the neutron's internal structure can be understood as follows: its positive charge has a toroidal Zitterbewegung structure with 0.83 fm toroidal radius, while its negative charge traces out an electron-like circular Zitterbewegung path. The negative charge has 0.83 fm classical and Zitterbewegung radii. This neutron structure represents a direct interpretation of experimental data, and it is illustrated on the right side of figure 7.4.1.

Kinetic energy estimation for the low probability $p^+ + e_n^-$ state. We identified in chapter 6 that there is a small probability of finding a neutron in the $p^+ + e_n^-$ two-particle state. Since the classical particle radius is inversely proportional to the relativistic particle mass, it follows that the proton-bound nuclear electron energy is approximately $0.511 \cdot \frac{2.82}{0.83}$ MeV=1.74 MeV. I.e. the kinetic energy of a proton-bound e_n^- particle increases by around 0.2 MeV with respect to its 1.554 MeV free particle state. The proton-bound e_n^- kinetic energy is thus similar to its 0.26 MeV binding energy. This result is a sanity check on our model because it is compatible with the virial theorem, which requires that the electric binding between a positive and a negative charge produces approximately the same binding energy and kinetic energy values.

Assessment of e^--e_n^- differences. At this point, one may ask what the main difference is between an electron a nuclear electron. Based on what we learnt so far, the e^--e_n^- difference is completely analogous to the e^--μ^- difference. In both cases, the heavier unstable particle soon decays into an electron, accompanied by neutrino emission. Neutral particle formation by proton capture requires a match between the lepton's classical radius and the proton's toroidal Zitterbewegung radius. If the proton's toroidal Zitterbewegung radius was three times larger, it could directly capture an electron into a structure like in figure 7.4.1. If the proton's toroidal Zitterbewegung radius was three times smaller, it could only capture a 4.5 MeV e_π^- particle into a structure like in figure 7.4.1. In other words, the e_n^- particle has a completely analogous internal structure to an ordinary electron.

7.4.2. Neutron stabilization by a high electric potential. We saw in section 7.1.2 that the electrostatic potential is a control parameter of nuclear beta decay. Here, we look into the role of electrostatic potential through the example of ^{17}O. The ^{17}O nucleus is an interesting case for the study of neutron dynamics: it contains a neutron-like sub-particle which is the most similar to a free neutron.

The ^{16}O nucleus comprises four alpha sub-particles. When a neutron is captured by ^{16}O, where will it reside? Considering that the charge radii of ^{16}O and ^{17}O are the exactly same, the captured neutron must be located in the nuclear center, surrounded

by four alpha sub-particles. Since the magnetic moment of ^{16}O is zero, the magnetic moment of ^{17}O can be attributed to the captured particles. Interestingly, the magnetic moment of ^{17}O is nearly the same as the neutron's magnetic moment. Specifically, the ^{17}O magnetic moment is $-1.894\mu_N$, which 99% matches the neutron's $-1.913\mu_N$ magnetic moment. These data indicate that the ^{17}O nucleus contains a neutron-like sub-particle at its center, as schematically illustrated in figure 7.4.2[1].

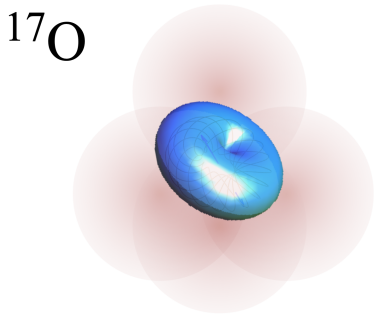

FIGURE 7.4.2. The ^{17}O nuclear structure. A neutron is in the center position, the red spheres illustrate alpha sub-particles.

^{17}O is a stable particle. The neutron at its center cannot decay, because the electron capture energy of ^{17}F is 2.76 MeV; the positive sign of electron capture energy means that the energy needed to remove an electron from the nucleus exceeds the 0.87 MeV maximum electron kinetic energy upon neutron decay. In other words a neutron becomes stabilized by being at a sufficiently high electrostatic potential, which prevents the electron's departure.

7.4.3. Neutron destabilization by a strong magnetic field. We now revisit the discussion of ^{9}Be excited states. As noted in section 7.3, the 2429 keV excitation of ^{9}Be decays mainly by emitting a proton and an electron, in contrast to the neutron-emitting 1684 keV and 2780 keV excitations. Therefore, the break-up of the neutron at 2429 keV excitation is controlled by some other parameter than just the excitation energy.

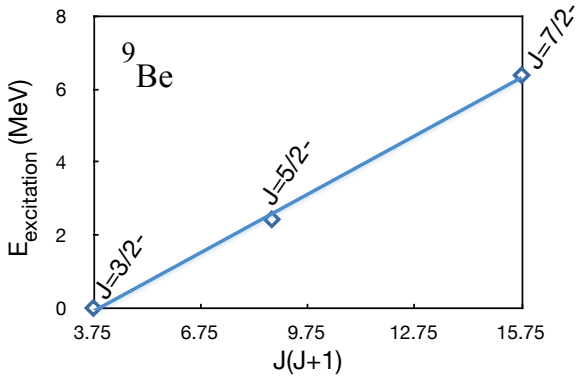

FIGURE 7.4.3. The rotational states of ^{9}Be

The ^{9}Be ground state has $J = \frac{3}{2}-$ rotational quantum number designation. Here, the "-" sign denotes the currently popular conjecture of a "negative parity state", which means

[1]While the ^{4}He charge radius is 1.7 fm, the ^{17}O charge radius is less than twice this size; it is only 2.7 fm. Four alpha sub-particles thus do not fit into ^{17}O without overlap.

that the nuclear wavefunction supposedly changes its sign upon the mirror reflection of spatial coordinates. The above-mentioned 2429 keV excited state has $J = \frac{5}{2}-$ rotational quantum number designation. Recognizing this pattern as a rotational series, the next rotational state is $J = \frac{7}{2}-$, and the corresponding excitation energy is 6380 keV.

The rotational Hamiltonian's eigenvalues are:

$$E_J = J\,(J+1)\,\frac{\hbar^2}{2I} \tag{7.4.2}$$

where E_J is the rotational energy eigenvalue at the rotational quantum number J, and I is the moment of inertia. Figure 7.4.3 shows the excitation energies as a function of $J(J+1)$. The three data points fit rather well onto a single line, which corresponds to the rotational excitations of a rigid structure. The data shown in figure 7.4.3 yields $\frac{\hbar^2}{2I}$=534 keV. Considering the 2.5 fm nuclear charge radius of ^{9}Be, this moment of inertia matches quite well the rotation of two alpha sub-particles around each other.

As the positively charged alpha sub-particles rotate around their center of mass, their rotation produces a strong magnetic field. The strength of this magnetic field is proportional to the rotational quantum number J because the moment of inertia remains constant. Since the neutron-like sub-particle breaks up in the $J = \frac{5}{2}-$ and $J = \frac{7}{2}-$ states, a sufficiently strong magnetic field appears to destabilize the neutron. Quantitatively, the magnetic moment values of the various ^{9}Be states are given in table 5. Its first two columns are literature data. Its last two columns are our predictions, calculated from the rotating alpha particles' J states. One may observe from table 5 values that, as a first approximation, the neutron remains stable if the magnetic moment of neighboring nucleons is $<\mu_N$, but becomes unstable if the magnetic moment of neighboring nucleons is $>\mu_N$.

	n	^{9}Be	^{9}Be* (2429 keV)	^{9}Be* (6380 keV)
μ	-1.913μ_N	-1.177μ_N	-0.686μ_N	-0.196μ_N
μ-μ_n	0	+0.736μ_N	+1.227μ_N	+1.717μ_N

TABLE 5. The magnetic moment of the neutron and various ^{9}Be states, in nuclear magneton units. The last row shows the magnetic moment values without the neutron's contribution.

7.4.4. Lepton number conservation. Since matter particles are created in particle-antiparticle pairs, the electron emission from neutron has been also modeled as some kind of particle-antiparticle pair creation process. The so-called "lepton number" is defined as a +1 value for a negatively charged lepton, and as a -1 value for a positively charged lepton. In a pair creation process, the total lepton number remains zero, and this has been referred to as the lepton number conservation rule.

In the context of neutron decay, the W-boson particle was hypothesized to be an intermediate particle, and its decay has been modeled as a particle-antiparticle pair creation process. For this reason, the W-boson particle has been assigned a 0 lepton number value and the emerging anti-neutrino has been assigned a -1 lepton value, even though it has no electric charge. However, this chapter demonstrated in numerous ways that there is no W-boson intermediate particle in neutron decay. In reality, the e_n^- is the intermediate particle of neutron decay, and it clearly has a +1 lepton number value. Insofar as neutron decay is modeled as a pair creation process, the emerging particle pair is: $p^+ + e_n^-$. This pair creation process means that the proton must have a -1 lepton number value, which

is perfectly in line with the results of chapter 3. The neutron particle retains the 0 lepton number value, as before.

One may ask what lepton number must be assigned then to a neutrino. We firstly approach this question from the perspective of muon decay. Up to now, it was hypothesized that a muon decay releases a neutrino-antineutrino pair. This hypothesis has been solely motivated by the above-mentioned W-boson decay model, which assigns a -1 lepton value to the anti-neutrino. In other words, modeling neutrinos as leptons forces theorists to model muon decays as a neutrino plus anti-neutrino pair creation process. While muon decays have been studied in numerous experiments, there is no experimental evidence at all for the simultaneous release of two neutrinos. On the other hand, there is experimental evidence [**23**] that the neutrinos produced by muon decay initiate the same nuclear reaction as in the famous Cowan–Reines neutrino experiment:

$$\bar{\nu} + p^+ \rightarrow n + e^+$$

Regarding the above reaction, we already identified the following correct lepton numbers: -1 for p^+, 0 for n, and -1 for e^+. This means that, in order to conserve lepton number, the incoming anti-neutrino must have 0 lepton number value. Consequently, we come to the conclusion that both neutrinos and anti-neutrinos have 0 lepton number value. The 0 lepton number assignment to neutrinos and anti-neutrinos also directly follows from chapter 5 results. Table 6 summarizes the correct assignment of lepton numbers to various particles.

Particle	e^-, e^+	e_n^-, e_n^+	μ^-, μ^+	p^-, p^+	n	ν, $\bar{\nu}$
Lepton number	+1, -1	+1, -1	+1, -1	+1, -1	0	0

TABLE 6. The correct assignment of lepton numbers.

Appendix: Neutron model parameters

$r_{p+} \simeq 0.46 \cdot 10^{-15} m$ poloidal radius of the positive elementary charge's Zitterbewegung
$r_{t+} \simeq 0.83 \cdot 10^{-15} m$ toroidal radius of the positive elementary charge's Zitterbewegung
$r_{c+} \simeq 1.54 \cdot 10^{-18} m$ classical radius of the positive elementary charge
$r_- \simeq 0.83 \cdot 10^{-15} m$ circulation radius of the negative elementary charge's Zitterbewegung
$r_{c-} \simeq 0.83 \cdot 10^{-15} m$ classical radius of the negative elementary charge
$\mu_+ \simeq +2.793 \mu_N$ toroidal magnetic moment of the positive elementary charge
$\mu_- \simeq -4.706 \mu_N$ magnetic moment of the negative elementary charge
$\mu_n \simeq -1.913 \mu_N$ net neutron magnetic moment

Bibliography

[1] A. Pais "Inward Bound", Clarendon Press (1986), p. 401.

[2] F. Halzen et al "Quarks & Leptons: An introductory course in modern particle physics", John Wiley and Sons (1984)

[3] M. Gell-Mann "A schematic model of baryons and mesons", Physics Letters, Volume 8, 3 (1964)

[4] J. D. Bjorken et al "Inelastic Electron-Proton and γ-Proton Scattering and the Structure of the Nucleon", Physical Review, Volume 185, 5 (1969)

[5] J. Kuti et al "Inelastic Lepton-Nucleon Scattering and Lepton Pair Production in the Relativistic Quark-Parton Model", Physical Review D, Volume 4, 11 (1971)

[6] W. L. Stubbs "The Nucleus of Atoms: One Interpretation", CreateSpace Independent Publishing Platform (2018)

[7] R. L. Jaffe "Where Does the Proton Really Get Its Spin?", Physics Today (1995)

[8] C. van der Leun et al "The deuteron binding energy", Nuclear Physics A, Volume 380.2 (1982)

[9] G. Vassallo et al "The electron and Occam's razor", Journal of Condensed Matter Nuclear Science, Volume 25 (2017)

[10] Nuclear data tables at www-nds.iaea.org

[11] M. H. MacGregor "The Enigmatic Electron", El Mac Books, 2nd edition (2013)

[12] M. Jung et al "First Observation of Bound-State β^- Decay", Physical Review Letters, Volume 69.15 (1992)

[13] H. Abele "The neutron. Its properties and basic interactions", Progress in Particle and Nuclear Physics, Volume 60 (2008), Pages 1–81

[14] A. Kovacs et al "Unified Field Theory and Occam's Razor: Simple Solutions to Deep Questions", World Scientific (2022)

[15] J. Chadwick et al "The nuclear photoelectric effect", Proceedings of the Royal Society of London, Volume 151.873 (1935)

[16] E. Storm et al "Photon cross sections from 1 keV to 100 MeV for elements Z=1 to Z=100", Nuclear Data Tables, Volume A7 (1970)

[17] H. Arenhövel et al "Photodisintegration of the deuteron: a review of theory and experiment", Springer (2012)

[18] D. Babusci et al "Deuteron photo-disintegration with polarised photons in the energy range 30–50 MeV", Nuclear Physics A, Volume 633.4 (1998)

[19] Y. Torizuka et al "Entangled pairs of 2p atoms produced in photodissociation of H_2 and D_2", Physical Review A, Volume 99.6 (2019)

[20] H. Atac et al "Measurement of the neutron charge radius and the role of its constituents", Nature communications, Volume 12.1 (2021)

[21] B. Heacock et al "Pendellösung interferometry probes the neutron charge radius, lattice dynamics, and fifth forces", Science, Volume 373.6560 (2021)

[22] U.G. Meissner "The proton radius and its relatives - much ado about nothing?", Journal of Physics: Conference Series, Volume 2586 (2023)

[23] C. Athanassopoulos et al "Evidence for neutrino oscillations from muon decay at rest", Physical Review C, Volume 54.5 (1996)

CHAPTER 8

Neutrino-induced inverse β-decay

Andras Kovacs[1]
[1] ExaFuse. E-mail: andras.kovacs@broadbit.com

ABSTRACT. In previous chapters, we introduced the idea of neutrinos being longitudinal electromagnetic waves, which have non-zero scalar field component. In this chapter, we validate this neutrino model through investigations of neutrino-induced inverse β-decay. Such nuclear reactions provide direct information about the captured neutrino radiation. They also gauge the intensity of neutrino-nucleus interactions. Lastly, we explore how electromagnetic scalar fields might be applied in macroscopic devices.

8.1. Inverse β-decays induced by long wavelength neutrinos

Between 1993-2014, Alexander Parkhomov undertook a pioneering series of experiments [**1, 2**], which appear to demonstrate that neutrinos are electromagnetic waves. In our interpretation of these experiments, they provide supporting evidence for chapter 5-6 results. Parkhomov constructed a metallic parabola shown in figure 8.1.1, which has beta emitting ^{60}Co material at its focal point. This parabola was aimed at the sky in a fixed position, scanning for low-frequency cosmic neutrinos. It swept the sky as the Earth rotates. As shown in figure 8.1.1, in a certain orientation the ^{60}Co decay rate increased by 3 orders of magnitude. This strong beta decay enhancement was simultaneously measured by two detectors, and the same effect was observed at several celestial orientations.

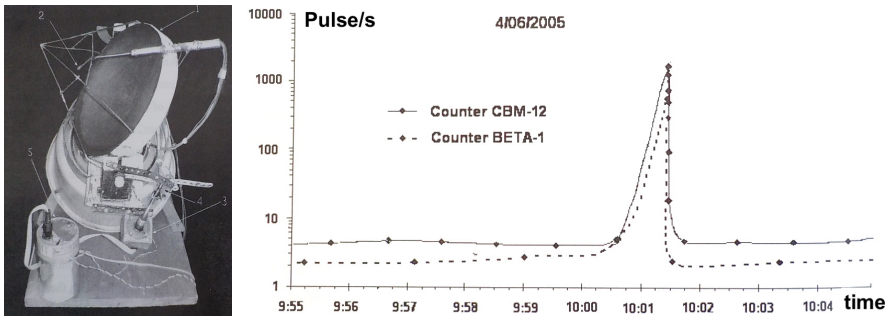

FIGURE 8.1.1. Measurement of cosmic neutrino induced nuclear beta decay. Left: parabolic metal antenna, with beta emitting ^{60}Co material at its focal point. Right: ^{60}Co decay rate during the experiment, as the antenna sweeps a small angle on the sky. Reproduced from [**1**].

The orientations associated with strong beta decay enhancement appear to point towards nearby stars. Furthermore, it is possible that our Sun's gravitational lensing effect magnifies the amplitude of electromagnetic radiation received from these stars.

A parabola collects incoming waves into its focal point only if the incoming wavelength is significantly larger than its surface roughness. Therefore, the incoming radiation has macroscopic wavelength. A reflection from a parabola surface is fundamentally an electromagnetic interaction. Regardless of whether a parabola reflects electromagnetic waves, sound waves, or small balls thrown at it, the underlying microscopic process is

always an electromagnetic interaction between the parabola material and the incoming wave components. The incoming neutrino radiation must interact electromagnetically, in order to be reflected. Without electromagnetic interaction, neutrinos would simply fly through the parabola.

Considering that neutrinos travel through space, may have macroscopically large wavelength, interact electromagnetically, and have been always observed to travel at the speed of light, in the author's opinion they are clearly electromagnetic waves and it is very difficult to interpret them otherwise.

Transversal electromagnetic waves dissociate nuclear structures only when their frequency is in the gamma range. However, transversal waves of macroscopic wavelengths do not have any effect on beta decaying isotopes. Furthermore, Parkhomov noticed that a glass parabola produces similar results to metallic parabolas; i.e. this electromagnetic wave reflects similarly from metallic and dielectric surfaces. For these reasons, the involved electromagnetic wave is not transversal, but longitudinal. Regarding neutrino theory, we established in chapter 5 that a neutrino is a longitudinal electromagnetic wave, which has non-zero scalar field component. The scientific literature refers to neutrino induced beta decay as "inverse beta decay". When the decaying nucleus is unstable, the required neutrino energy is arbitrarily small.

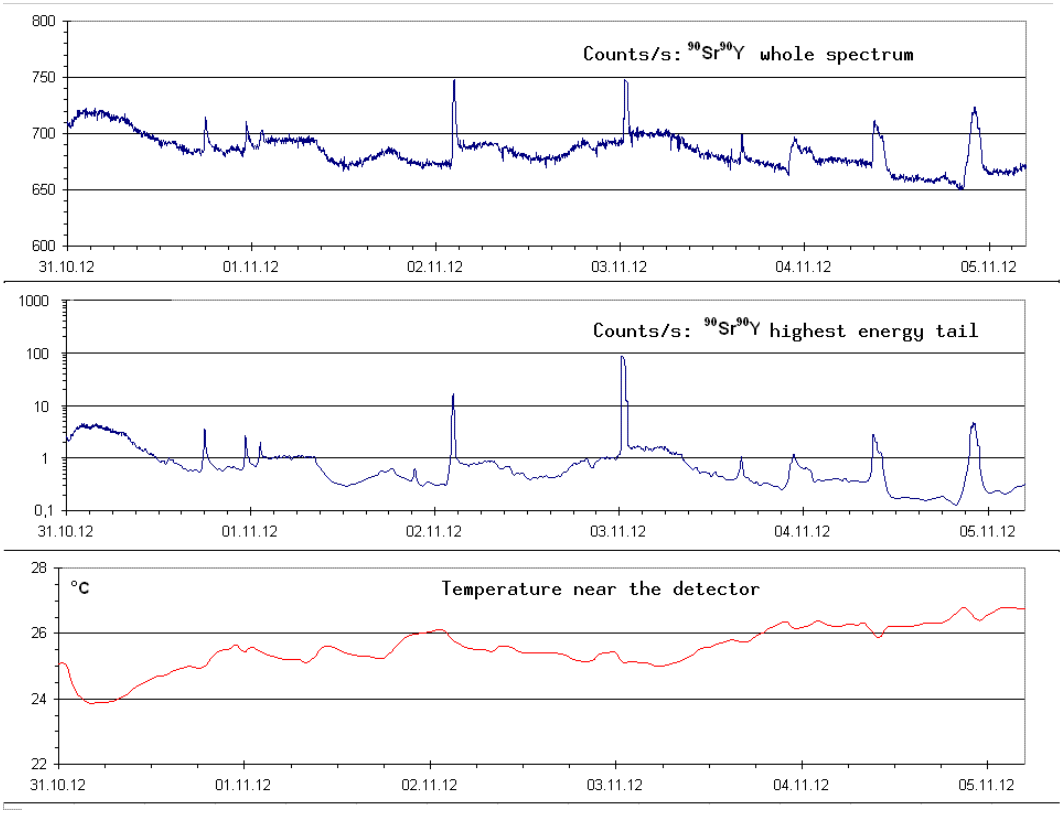

FIGURE 8.1.2. Measurement of beta decayed electron energy, induced by cosmic neutrino radiation. Top: the count rate of all emitted electrons. Middle: the count rate of most energetic electrons, near the maximum of ^{90}Sr beta decay energy. Bottom: temperature evolution. Data provided by Alexander Parkhomov.

In summary, our interpretation of Parkhomov's cosmic neutrino experiment is the following: i) the detected cosmic wave is a long wavelength electromagnetic radiation because it is collected by a parabola, ii) it is a longitudinal electromagnetic wave, and iii) this type of electromagnetic radiation strongly enhances the nuclear beta decay rate.

In a follow-up experiment, Parkhomov used the same set-up, but replaced the Geiger counter with a scintillation detector and energy filter in order to measure two count rates: the count rate of all emitted electrons, and the count rate of most energetic electrons. These count rates are respectively shown on the top chart and middle chart of figure 8.1.2. We note that the highest energy tail counts those electrons whose kinetic energy is near the maximum of ^{90}Sr beta decay energy.

As can be seen in figure 8.1.2 the count rate peaks measuring all emitted electrons grow less than 10%. On the other hand, the count rate peaks measuring the most energetic electrons grow by two orders of magnitude. This means that the absorbed neutrino radiation does not simply speed up nuclear beta decay, but induces electron emission only at the highest possible electron energy for the given beta decay. The inverse beta decay reaction is characterized by exactly such an electron energy distribution. An inverse beta decay reaction yields two reaction products, and is exemplified by the $\nu + n \rightarrow p^+ + e^-$ reaction. In this case, momentum conservation dictates that the decay energy is carried away mainly by the much lighter electron product.

With reference to chapter 6, the highest electron kinetic energy is associated with a decay event at the overlap position of the neutron's positive and negative charges. In contrast, we showed that an ordinary beta decay event is associated with a spatial separation of the neutron's positive and negative charges. We also discussed in chapters 6-7 that a neutron's positive and negative charges overlap most of the time, i.e. the neutron is mostly in single-particle state. It is thus anticipated that a randomly arriving neutrino wave finds overlapping elementary charges; a decay from this state produces the highest possible electron kinetic energy.

8.2. Inverse β-decays induced by short wavelength neutrinos

We established that long wavelength neutrino waves reflect from surfaces similarly to light reflection. Short wavelength neutrino waves are expected penetrate into materials also similarly to short wavelength gamma radiation. However, it would be surprising and illogical to find nearly infinite penetrating power of short wavelength neutrino waves. At this point, we must address the Homestake neutrino experiment [**3**], because its authors claim to measure solar neutrinos 2.5 km underground; this experiment is at the origin of neutrinos' nearly infinite penetrating power myth. How do the authors of reference [**3**] know that they are measuring solar neutrinos, and not thorium chain geo-neutrinos from the surrounding rock? They do not distinguish the two sources; this question remains unaddressed in reference [**3**]. Apparently, they assume that their inverse beta decay measurement is only sensitive to solar neutrinos, while thorium chain beta decay produces anti-neutrinos. However, the equivalence between neutrino and anti-neutrino waves follows from chapter 5 results. Furthermore, a recent experiment [**4**] claims to estimate thorium concentration from inverse beta-decay measurements.

Suspecting that the Homestake neutrino experiment has been detecting geo-neutrinos, we review in the following paragraphs an experiment that gauges the absorption of short wavelength neutrinos. Specifically, we discuss the inverse beta decay of ^{88}Sr, induced by energetic neutrinos.

The authors of [**5**] irradiated a uranium foil target by 62 MeV alpha particles. Kinetically induced uranium fission is known to occur already above 1 MeV impacting neutron energy and above 7 MeV impacting proton energy. This experimental condition therefore induces uranium fission, which promptly releases short wavelength neutrino radiation.

A few grams of $SrCO_3$ powder was placed in the vicinity of this uranium target, but separated from it by 0.1 mm thick kapton film. Such film thickness is selected in order

to block the passage of charged particles. This $SrCO_3$ powder is thus subjected to short wavelength neutrinos and gamma photons.

The employed $SrCO_3$ powder is enriched in ^{88}Sr: it comprises 99.2% ^{88}Sr, approximately 0.4% ^{86}Sr, and 0.4% ^{87}Sr. The uranium target was irradiated for seven hours at 1 μA current. The post-experiment gamma spectrum of the $^{88}SrCO_3$ powder is shown in figure 8.2.1, and we interpret this spectrum in the following paragraphs.

The ^{87}Sr isotope has a long-lived excitation at 388 keV energy. The 388 keV peak thus corresponds to the gamma-induced nuclear excitation of ^{87}Sr.

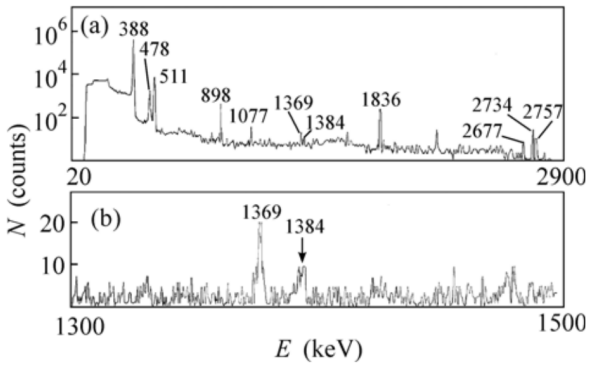

FIGURE 8.2.1. The gamma spectrum of irradiated strontium material, subjected to gamma radiation reaching up to 62 MeV. Spectrum a) shows the full measurement range between 20 and 2900 keV, spectrum b) shows the 1300 to 1500 keV energy range. Reproduced from [**5**].

The 898, 1836, and 2734 keV gamma peaks correspond to ^{88}Y. The 1077 keV gamma peak corresponds to ^{86}Y. Although there is 200 times as much ^{88}Sr than ^{86}Sr, the half-life of ^{86}Y is 200 times shorter than the ^{88}Y half-life; it is therefore anticipated that their decay radiation has peaks of comparable intensity. Regarding ^{87}Y, its gamma peaks are at 389 and 485 keV; these peaks are not visible because of the nearby larger the larger radiation of other isotopes. The 511 keV gamma peak corresponds to the positron emission by these yttrium isotopes.

The above-discussed yttrium isotopes are produced via neutrino-induced inverse beta decay:

$$^{88}Sr + \nu\,(> 3.6\,MeV) \rightarrow {}^{88}Y + e^-$$

$$^{86}Sr + \nu\,(> 5.24\,MeV) \rightarrow {}^{86}Y + e^-$$

The presence of ^{86}Y and ^{88}Y isotopes thus demonstrates neutrino-induced inverse beta decay, and the above-indicated high energy thresholds mean that the absorbed neutrinos have very short wavelength. What does this experiment tell us about the absorption of energetic neutrinos? Since the experiment uses only a few grams of target material, the strong signals seen in figure 8.2.1 mean that even short wavelength neutrinos have reasonably high nuclear absorption cross-section. That is exactly what we anticipate of electromagnetic waves. In the author's opinion, neutrinos flying through the Earth do not exist.

8.3. Achieving macroscopic scalar field in a laboratory

An essential difference between neutrinos and photons is that neutrinos have non-zero electromagnetic scalar field. Considering further the possibility of electromagnetic scalar

field induced nuclear decays, a practical challenge is to understand how such a scalar field might be created in laboratory setting. The key idea is to consider longitudinal phonons; from the macroscopic perspective, a longitudinal phonon is a longitudinal electromagnetic wave. It is mathematically equivalent to the transformation of electric and scalar field energies into each other, with the electric field pointing along the direction of wave propagation. For a longitudinal phonon wave traveling along the z direction, its mathematical solution was already pointed out in chapter 5:

$$E_z = E_0 \sin(\omega t - kz)\,,\; S = S_0 \sin(\omega t - kz)$$

In contrast to vacuum propagation, a phonon wave moves much slower than the speed of light; its propagation speed is determined by the electromagnetic parameters of a given material. The phonon is internally reflected at the surface of the given material, and such **a reflection process is always accompanied by an exponentially decaying tail on the other side of the interface**. The presence of an exponential tail beyond the reflection point directly follows from the conservation of electromagnetic momentum at the interface. The same principle applies to ordinary light waves or quantum mechanical waves as well, whose reflection is also accompanied by an exponential tail. Figure 8.3.1 illustrates a longitudinal phonon wave propagating inside the material, and its evanescent exponential tail. Microscopically, the phonon wave comprises nuclei and electrons; there is no real scalar field in-between these particles, and thus the sinusoidal wave is represented by a dashed line in figure 8.3.1. The situation is however different for the ν_t tail; it is in a vacuum region and therefore comprises only electromagnetic fields. The exponentially decaying field therefore comprises a real electromagnetic scalar field, and it is thus represented by a solid line in figure 8.3.1. I.e. the lattice particles, which generate a phonon wave, collectively create a non-zero electromagnetic scalar field beyond the interface.

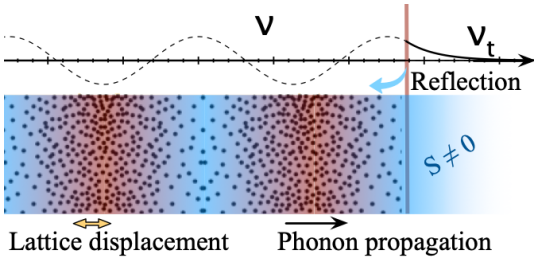

FIGURE 8.3.1. An illustration of a longitudinal phonon wave reflecting from the material surface. The vertical line represents the material surface, and the blue colored region beyond the surface represents the exponentially decaying tail of the reflecting phonon wave.

According to our analysis, bounding or layered surfaces could play a key role in inducing nuclear reactions. We showed in section 8.1 that even low energy neutrinos accelerate nuclear beta decay. Therefore, we predict that phonons reflecting from surfaces shall accelerate the decay of unstable isotopes. One could ask whether such reflecting phonons might induce the decay of an otherwise stable isotope. References [**6, 7**] suggest this possibility: their authors report unexpected nuclear reactions at layered material interfaces, while phonons are generated by the diffusion of hydrogen or deuterium across the involved materials. In the following chapter we take a closer look at the nuclear reactions taking place at such interfaces.

Acknowledgements: The author thanks Alexander Parkhomov for useful discussions.

Bibliography

[1] A. G. Parkhomov "Bursts of count rate of beta-radioactive sources during long-term measurements", International Journal of Pure and Applied Physics, volume 1.2 (2005), Pages 119-128

[2] A. G. Parkhomov "SPACE. EARTH. HUMAN. New Views on Science." (2019)

[3] B. T. Cleveland et al "Measurement of the solar electron neutrino flux with the Homestake chlorine detector", The Astrophysical Journal, volume 496.1 (1998)

[4] S. Abe et al "Abundances of uranium and thorium elements in Earth estimated by geoneutrino spectroscopy", Geophysical Research Letters, volume 49.16 (2022)

[5] B. G. Novatsky et al "Possible Observation of Light Neutron Nuclei in the Alpha Particle Induced Fission of ^{238}U", JETP Letters, Volume 96.5 (2012)

[6] Y. Iwamura et al "Excess energy generation using a nano-sized multilayer metal composite and hydrogen gas", Journal of Condensed Matter Nuclear Science, volume 33 (2020)

[7] Y. Iwamura et al "Anomalous heat generation that cannot be explained by known chemical reactions produced by nano-structured multilayer metal composites and hydrogen gas", Japanese Journal of Applied Physics, volume 63 (2024)

CHAPTER 9

Nuclear chemistry with alpha particles: experimental signatures of neutral particles with $4N$ mass pattern

Andras Kovacs[1] and **Heikki Sipilä**[2]
[1] ExaFuse. E-mail: andras.kovacs@broadbit.com
[2] Fenno-Aurum

9.1. Introduction

The neutron is the best-known neutral particle, and its nuclear capture is the basis of present-day nuclear energy production. In this chapter we look into the existence of heavier neutral particles, which could be also captured by some nucleus. Specifically, we look into neutral composites comprising alpha particles and nuclear electrons. If such neutral clusters exist for sufficiently long time, their nuclear capture can be used for the production of energy or new materials.

The search for electrically neutral multi-nucleon clusters is an old, but still unsettled problem of nuclear physics. Related publications anticipate short-lived and weakly bound neutron clusters [**2, 6**].

The observation of electrically neutral 4-nucleon particles has been reported in various high-energy experiments [**2, 6**]. Reports of neutral 2-, 6-, or 8-nucleon clusters are much more rare, and there are no reports of odd nucleon numbered neutral clusters. The scientific literature refers to such 4-nucleon clusters as "tetra-neutrons", as they are thought to be a meta-stable composite of four neutrons. However, the dissociation of neutral 4-nucleon particles into individual neutrons has never been observed.

Reference [**1**] assigns $2.6 \cdot 10^{-23}$ s half-life to tetra-neutrons. Such a short half-life precludes their absorption by any nucleus. However, the following sections describe 4-nucleon particle capture by other nuclei, which means that this particle's half-life must be many orders of magnitude longer than the tetra-neutron half-life.

Reference [**3**] argues that in case ^{88}Sr captures a tetra-neutron, it should transmute to ^{91}Sr, with the emission of an energetic neutron. In contrast to this expectation, section 9.3 describes ^{88}Sr to ^{92}Sr transmutation, without any ^{91}Sr reaction product. Yet again, it is called into question whether the involved neutral 4-nucleon particle could be a loosely bound neutron cluster.

These facts indicate that a neutral 4-nucleon particle should be regarded as a neutral $(^4He^{2+} + 2e_n^-)$ composite, rather than four loosely bound neutrons. In the following, we use the $^4He^0$ notation to refer to a hypothetical neutral alpha particle, which beta decays into an ordinary alpha particle.

9.2. The evolution of ^{242}Pu concentration in nuclear reactors

In uranium-fueled nuclear reactor cores, ^{239}Pu is produced via a neutron capture by ^{238}U. Further neutron captures generate heavier plutonium isotopes. Starting from ^{238}U, it takes four consecutive neutron captures to get to ^{242}Pu, and thus its concentration

should be very low in the initial stages of the fuel cycle. On the other hand, if ${}^4He^0$ particles were produced in nuclear reactor cores, then ^{242}Pu would be generated via a single capture reaction:

$$^{238}U + {}^4He^0 \rightarrow {}^{242}U \rightarrow {}^{242}Np + e^- \rightarrow {}^{242}Pu + 2e^-$$

In the absence of the above reaction, the experimental ^{242}Pu concentration must evolve according to the neutron capture calculation. In the presence of the above reaction, the experimental ^{242}Pu concentration must be higher than what is predicted by the neutron capture calculation, especially in the initial stages of the fuel cycle.

A recent study [**4**] analyzed over 250 fuel samples from multiple reactors, at various stages of burn-up. Under a low burn-up condition of $<$10 GW-day per fuel ton, the author of [**4**] finds on average 3 times higher than predicted ^{242}Pu concentration. In the same samples, the average ^{239}Pu concentrations match predictions, which means that the neutron capture calculations are correctly done. The largest concentration excess with respect neutron capture calculations is 400% for ^{242}Pu, while only 39% for ^{239}Pu. These large discrepancies demonstrate that the capture of ${}^4He^0$ particles is the main source of ^{242}Pu during the initial stages of the fuel cycle.

As the fuel cycles progress, the probability of ^{242}Pu production via four consecutive neutron captures rises steeply. The discrepancy between experimental and predicted ^{242}Pu concentrations becomes gradually smaller with rising burn-up rate [**4**]. Approximately the same result is found in reference [**5**]: relative to neutron capture calculations, 15-20% higher experimental ^{242}Pu/^{239}Pu ratio is observed in highly burnt up nuclear fuel. The correctness of the authors' neutron capture calculation is validated by the matching concentration of other isotopes, such as the ^{146}Nd/^{145}Nd ratio [**5**]. Consecutive neutron capture thus becomes the main source of ^{242}Pu only in the final stages of the fuel cycle.

In summary, the evolution of ^{242}Pu concentration demonstrates the presence of short-lived ${}^4He^0$ particles in nuclear reactor cores.

9.3. ^{88}Sr to ^{92}Sr transmutation via ${}^4He^0$ capture

Let us revisit the experiment described in section 8.2. The post-experiment gamma spectrum of the $^{88}SrCO_3$ powder is shown in figure 8.2.1, and it contains a 1384 keV peak which corresponds to the beta decay of ^{92}Sr. By continued monitoring of this gamma peak, the authors of [**6**] measure a half-life of 2.66 h, which also matches the 2.61 h half-life of ^{92}Sr. On the other hand, there are no peaks in the gamma spectrum belonging to ^{89}Sr, ^{90}Sr, or ^{91}Sr. Therefore, the initial ^{88}Sr transmutes in a single step to ^{92}Sr. We recognize this reaction as the nuclear capture of ${}^4He^0$ particles:

$$^{88}Sr + {}^4He^0 \rightarrow {}^{92}Sr \rightarrow {}^{92}Y + e^- \rightarrow {}^{92}Zr + 2e^-$$

The fm-scale size of the neutral ${}^4He^0$ particles is demonstrated by the fact that they pass through the 0.1 mm kapton tape before being captured by the ^{88}Sr nuclei.

When the authors of [**6**] repeated the same experiment with tantalum foil target, there was no peak at 1384 keV. It means that only certain nuclei are capable of emitting ${}^4He^0$ particles.

9.4. Experimental signatures of $2 \cdot {}^4He^0$ and $3 \cdot {}^4He^0$ clusters

Unusual, fusion-like nuclear transmutation of certain elements was observed in replicated experiments [**7, 8, 9, 10**]. It is necessary to find a mechanism that explains such transmutations. These transmuted elements were cesium, strontium, or barium, and they were implanted at the interface between palladium (Pd) and calcium oxide (CaO). During

the transmutation experiment, a flow of deuterium diffuses across these materials, which generates phonons. I.e. these reactions require phonons and take place at an interface layer; the proposed role of such interfaces and reflecting phonons was explained in chapter 8.

In these experiments, the ${}^{133}_{55}Cs \rightarrow {}^{141}_{59}Pr$, ${}^{88}_{38}Sr \rightarrow {}^{96}_{42}Mo$, ${}^{137}_{56}Ba \rightarrow {}^{149}_{62}Sm$, and ${}^{138}_{56}Ba \rightarrow {}^{150}_{62}Sm$ transmutations are specifically observed. In all cases, the mass number increases by 8 or 12 nucleons, not by any other mass number. These isotopes' high Coulomb barrier means that the observed transmutations involved the capture of neutral particles, comprising 8 or 12 nucleons. Therefore, these fusion-like reactions can be written as follows:

$$ {}^{133}_{55}Cs + 2 \cdot {}^4He^0 \rightarrow {}^{141}_{59}Pr + 4 \cdot e^- $$

$$ {}^{88}_{38}Sr + 2 \cdot {}^4He^0 \rightarrow {}^{96}_{42}Mo + 4 \cdot e^- $$

$$ {}^{137}_{56}Ba + 3 \cdot {}^4He^0 \rightarrow {}^{149}_{62}Sm + 6 \cdot e^- $$

$$ {}^{138}_{56}Ba + 3 \cdot {}^4He^0 \rightarrow {}^{150}_{62}Sm + 6 \cdot e^- $$

In the above equations, the $2 \cdot {}^4He^0$ and $3 \cdot {}^4He^0$ symbols represent neutral clusters, comprising $2 \cdot ({}^4He^{2+} + 2e^-_n)$ and $3 \cdot ({}^4He^{2+} + 2e^-_n)$ structures. The absence of post-experimental radioactivity implies that the indicated number of electrons are simultaneously emitted upon these clusters' nuclear capture; i.e. they are loosely bound nuclear electrons. Such a simultaneous nuclear emission of 4 or 6 electrons is impossible according to quark-based theories. The reality of these reactions supports chapters 6-7.

Figure 9.4.1 shows the evolution of ${}^{133}_{55}Cs$ and ${}^{141}_{59}Pr$ isotope concentrations with experimental time. In this case, the starting material comprises ${}^{133}_{55}Cs$ at the CaO-Pd interface. These concentration changes are the basis of the above identified ${}^{133}_{55}Cs + 2 \cdot {}^4He^0 \rightarrow {}^{141}_{59}Pr + 4 \cdot e^-$ reaction. As can be seen in figure 9.4.1, this reaction is well-replicable, and the transmutation rate is very large. The neutral $2 \cdot {}^4He^0$ structure has an apparently long half-life, so that it can produce such high transmutation rate in relatively short time. Similarly, figure 9.4.2 shows the evolution of Sr and Mo concentrations. In this case, the starting material comprises ${}^{88}_{38}Sr$ at the CaO-Pd interface, and the outcome demonstrates ${}^{88}_{38}Sr + 2 \cdot {}^4He^0 \rightarrow {}^{96}_{42}Mo + 4 \cdot e^-$ reaction. Once it is clarified how to produce $2 \cdot {}^4He^0$ and $3 \cdot {}^4He^0$ efficiently, there will be practical applications.

Since the above-described fusion-like reactions occur only in deuterated palladium environment, the $2 \cdot {}^4He^0$ and $3 \cdot {}^4He^0$ particles are probably emitted from Pd, which is the common factor in all of these experiments. Are $2 \cdot {}^4He^0$ and $3 \cdot {}^4He^0$ particle signatures present in other experiments involving deuterated palladium? Interestingly, references **[11, 12]** report particle track microphotographs, which appear to show $2 \cdot {}^4He^0$ and $3 \cdot {}^4He^0$ break-up events. Figure 9.4.3 shows a "double track" and a "triple track" pattern in a CR-39 particle detector, which was obtained during electrochemical Pd/D co-deposition experiments. No such tracks were detected in control experiments. Symmetric "double track" and "triple track" patterns are associated with a neutral particle induced reaction because they show a nucleus symmetrically fragmenting into two or three particles. If an energetic charged particle caused such a nuclear break-up, its track would be also seen in the CR-39 detector. On the other hand, an energetic neutral particle does not leave a trace while approaching the nucleus with which it collides. The authors of **[11, 12]** emphasize that the "triple track" pattern of figure 9.4.3 is analogous to CR-39 patterns seen when it is irradiated by 14 MeV neutrons: the "triple track" corresponds to the neutron-induced

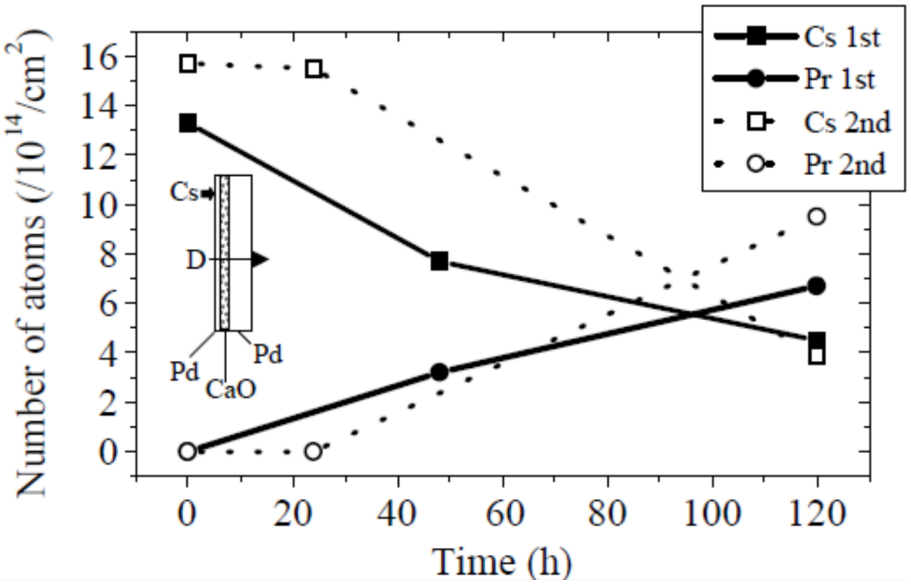

FIGURE 9.4.1. The evolution of $^{133}_{55}Cs$ and $^{141}_{59}Pr$ isotope concentrations with experimental time. The chart overlays the data of two experiment runs described in [**7, 8**].

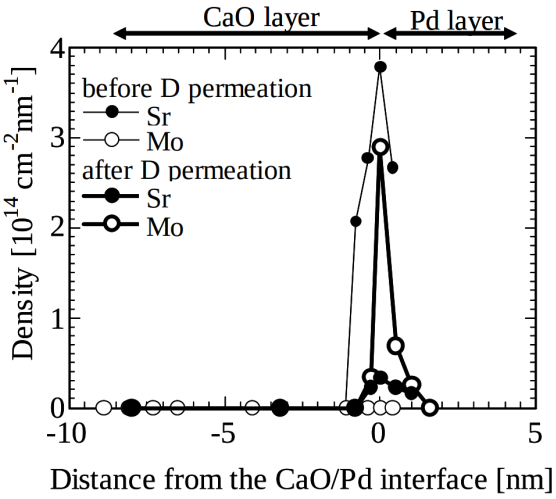

FIGURE 9.4.2. The concentration of Sr and Mo before and after the deuterium permeation experiment. The chart overlays pre- and post-experimental XPS measurements, reproduced from [**10**].

break-up of a ^{12}C nucleus into three ^{4}He particles. However, there is no reasonable source of high-energy neutrons in Pd/D co-deposition[1], and the energetic neutron hypothesis still can not explain the "double track" pattern of figure 9.4.3. The more logical explanation is that neutral $2 \cdot {}^4He^0$ and $3 \cdot {}^4He^0$ particles enter into the CR-39 detector, and the ^{4}He particles that fly apart upon $2 \cdot {}^4He^0$ or $3 \cdot {}^4He^0$ decay produce "double track" or "triple track" patterns in the CR-39 detector.

There are numerous reports of ^{4}He production during various Pd/D experiments. Reference [**13**] contains a good overview of measuring the tiny ^{4}He production during Pd/D experiments. In the context of $2 \cdot {}^4He^0$ and $3 \cdot {}^4He^0$ particles' already established

[1]Even if one assumes $D - D$ fusion, the resulting neutrons have too low energy to break-up a ^{12}C nucleus into three ^{4}He particles.

presence, they decay into ^{4}He particles and therefore ^{4}He measurements can be interpreted as $2 \cdot {}^4He^0$ and $3 \cdot {}^4He^0$ decay products' observation.

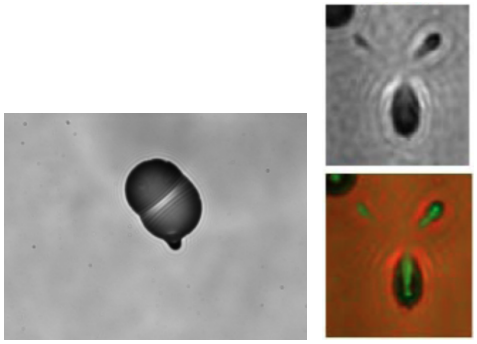

FIGURE 9.4.3. Microphotographs, which appear to show $2 \cdot {}^4He^0$ and $3 \cdot {}^4He^0$ break-up events: a "double-track" (left) and a "triple-track" (right) event in a CR-39 detector. These events occurred during electrochemical Pd/D co-deposition. Reproduced from **[11, 12]**.

We established in section 9.2 that neutral $^4He^0$ particles are emitted in a fraction of uranium fission events. This brings up the question of whether $2 \cdot {}^4He^0$ and $3 \cdot {}^4He^0$ originate from Pd fission events. I.e. the question is whether the fission of Pd is the main nuclear reaction in Pd/D or Pd/H based experiments, where hydrogen or deuterium diffuses through palladium. This question has been investigated in great detail via the long-duration experiments reported in references **[14, 15, 16]**: each of these works establish the nuclear fission reaction of palladium, where the $^{64}_{40}Zn$ isotope is the main reaction product. References **[14, 15, 16]** study both Pd/D and Pd/H based set-ups, where these hydrogen isotopes are pushed through palladium by both gas-phase and electro-chemical methods: the same outcome of $^{64}_{40}Zn$ main reaction product is obtained in all cases. In particular, reference **[15]** employs an easily replicable experimental set-up, and demonstrates that the distribution of appearing zinc isotopes strongly deviates from their natural abundance: mostly just the $^{64}_{40}Zn$ isotope is produced. The nuclear fission of palladium is thus established as the most likely source of $2 \cdot {}^4He^0$ and $3 \cdot {}^4He^0$ particles. The experimental set-up of reference **[15]** is a practical basis for the further exploration of neutral $2 \cdot {}^4He^0$ and $3 \cdot {}^4He^0$ production.

In conclusion, references **[7, 8, 9, 10, 12, 11, 13]** demonstrate various signatures of $2 \cdot {}^4He^0$ and $3 \cdot {}^4He^0$ particles, and references **[14, 15, 16]** report evidences of the palladium fission reaction where $2 \cdot {}^4He^0$ and $3 \cdot {}^4He^0$ are produced. When Fleischmann and Pons announced in 1989 their hypothesis of $D-D$ fusion in an electrochemical Pd/D based cell, there was a great deal of skepticism because their observations were difficult to reproduce and did not match the established properties of $D - D$ fusion. It soon turned out that Fleischmann and Pons did not run a Pd/H based control and their neutron measurement was poorly executed; their case for $D - D$ fusion thus fell apart. On the other hand, references **[14, 15]** established within 9 years that the actually occurring nuclear reaction is Pd fission, and it occurs in both Pd/D and Pd/H based experimental set-ups. The production of $2 \cdot {}^4He^0$ and $3 \cdot {}^4He^0$ particles is one surprising aspect of Pd fission. An other surprising aspect is that Pd fission produces only stable elements, as evidenced by the absence of post-experimental radioactivity in excess heat producing Pd/D and Pd/H based experiments. In the next chapter, we investigate a tungsten fission reaction that produces only stable elements, and find that it involves the prompt emission of nuclear electrons.

9.5. A material that continuously emits neutral $2 \cdot {}^4He^0$ particles

An interesting thorium-containing material has been synthesized at ExaFuse; its unexpected properties are reported in the last chapter of reference [**17**]. We made high-precision gamma spectrum measurements involving this material, using Baltic Scientific Instruments' high purity germanium (HPGe) based detector, which resides in a lead shielded chamber. Figure 9.5.1 shows a 0.6 g sample of this material being placed onto the detector; the sample material resides on a mylar film and it is surrounded by 800 kg lead shielding. There is approximately 8 cm distance between this sample and the lead shielding.

FIGURE 9.5.1. The placement of our thorium-containing sample material in the lead shielded HPGe detector.

After being in the detector for 2 hours, this sample was removed and the gamma spectrum of the empty detector was measured for 4 hours. Thereafter, the gamma spectrum of the empty detector was measured for another 16 hours. Surprisingly, gamma signatures of ^{214}Pb decay are seen in the gamma spectrum that is measured immediately after the sample removal, along with gamma signatures of the follow-up ^{214}Bi decay step. Figures 9.5.2 and 9.5.3 show these gamma signatures. However, these ^{214}Pb and ^{214}Bi peaks fade almost completely into the background in the next gamma spectrum, which was measured for 16 hours. The background spectrum was measured for 64 hours, before the experiment.

The ^{214}Pb half-life is 27 minutes, and the ^{214}Bi half-life is 20 minutes. The almost complete disappearance of ^{214}Pb and ^{214}Bi decay peaks after 4 hours is compatible with their half life, and proves that ^{214}Pb was produced while the sample was in the spectrometer. Since we measure ^{214}Pb signature after the sample was taken out from the spectrometer, ^{214}Pb must reside within the spectrometer, probably in its lead shielding. These observations lead up to the following puzzle: how was ^{214}Pb produced inside the lead shielding while the sample was in the spectrometer? The only plausible explanation is that some neutral particle has been emitted from our sample, which transmuted some lead nuclei into ^{214}Pb. Considering that the heaviest lead isotope is ^{208}Pb, the absorption of $^4He^0$ is not sufficient to produce ^{214}Pb. The inevitable conclusion is that the occurring lead transmutation must involve the absorption of $2 \cdot {}^4He^0$, i.e. the observed reaction is:

$$^{206}_{82}Pb + 2 \cdot {}^4He^0 \rightarrow {}^{214}_{82}Pb$$

A logical next question: does lead's ^{208}Pb main isotope also absorb $2 \cdot {}^4He^0$ particles? Such a process would produce ^{216}Pb, which decays within minutes to ^{212}Pb. The 10.6 hours half-life of ^{212}Pb is much longer; if ^{212}Pb is produced via $2 \cdot {}^4He^0$ absorption, it shall

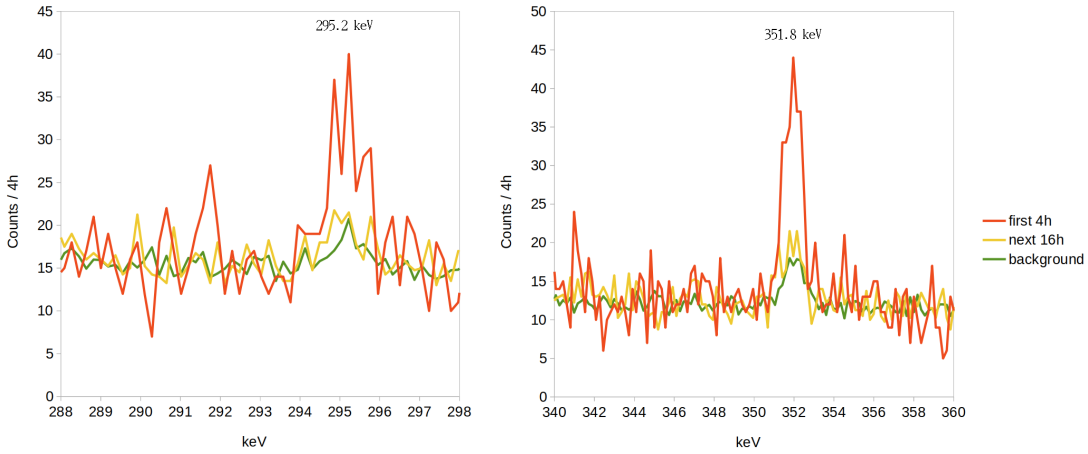

FIGURE 9.5.2. The ^{214}Pb decay peaks in the gamma spectrum, measured after the sample was removed from the detector.

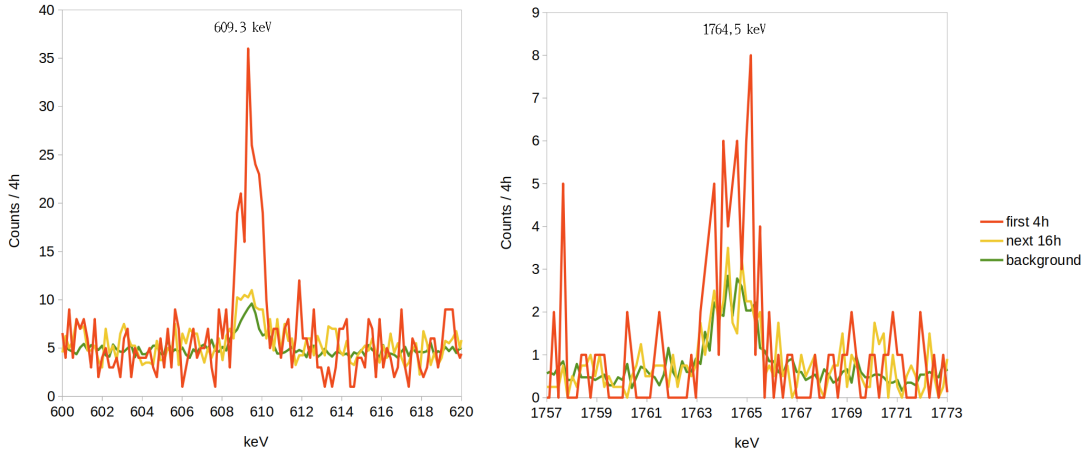

FIGURE 9.5.3. The ^{214}Bi decay peaks in the gamma spectrum, measured after the sample was removed from the detector.

essentially accumulate while the sample is in the detector. However, ^{212}Pb might also accumulate via the ${}^{208}_{82}Pb + {}^4He^0 \rightarrow {}^{212}_{82}Pb$ process. To check for either possibility, we look at the difference between the 2^{nd} and 1^{st} hour gamma counts, that are measured while the sample is in the detector. This measurement data is shown in figure 9.5.4. The clearly observable peak at 238.6 keV, which is the main gamma peak of ^{212}Pb decay, demonstrates that ^{212}Pb is accumulating. Our ^{212}Pb accumulation measurement is therefore a second evidence of neutral particle absorption in the lead shielding material, and it may correspond to either $^4He^0$ or $2 \cdot {}^4He^0$ absorption by ^{208}Pb.

Assuming that $2 \cdot {}^4He^0$ particles are emitted from thorium, we are observing the ${}^{232}_{90}Th \rightarrow {}^{224}_{90}Th + 2 \cdot {}^4He^0$ decay process. The resulting ^{224}Th soon decays into ^{208}Pb via a sequence of alpha particle emissions. Our results imply that the emission of neutral $2 \cdot {}^4He^0$ particles is continuous from our sample material: thorium essentially gains a new decay branch in our material, and this new decay branch involves $2 \cdot {}^4He^0$ emission.

For a detailed study of neutral $2 \cdot {}^4He^0$ particles, it is very useful to have a source continuously emitting them. We welcome related collaboration enquiries.

Acknowledgements: The authors thank the Baltic Scientific Instruments company for the gamma spectrum measurements.

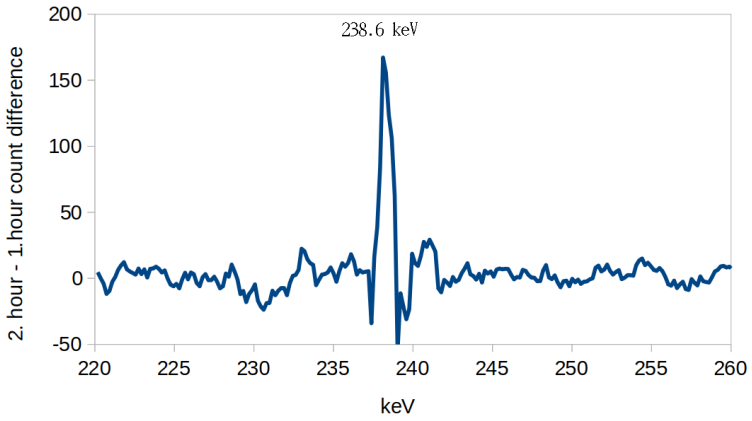

FIGURE 9.5.4. The difference between the 2nd and 1st hour gamma counts in the vicinity of the main ^{212}Pb decay peak, measured while the sample is in the detector. This peak signal demonstrates ^{212}Pb accumulation while the sample is being in the detector.

Bibliography

[1] https://www-nds.iaea.org

[2] T. Faestermann et al "Indications for a bound tetraneutron", Physics Letters B, volume 824 (2022)

[3] H. Fujioka et al "Search for particle-stable tetraneutrons in thermal fission of ^{235}U", Physical Review C, volume 108.5 (2023)

[4] M. Oettingen "The Application of Radiochemical Measurements of PWR Spent Fuel for the Validation of Burnup Codes", Energies, volume 15 (2022)

[5] J. S. Kim et al Analysis of high burnup pressurized water reactor fuel using uranium, plutonium, neodymium, and cesium isotope correlations with burnup", Nuclear Engineering and Technology, volume 47 (2015)

[6] B. G. Novatsky et al "Possible Observation of Light Neutron Nuclei in the Alpha Particle Induced Fission of ^{238}U", JETP Letters, volume 96.5 (2012)

[7] Y. Iwamura et al "Elemental Analysis of Pd Complexes: Effects of D_2 Gas Permeation", Japanese Journal of Applied Physics, Volume 41.7R (2002)

[8] T. Hioki et al "Inductively Coupled Plasma Mass Spectrometry Study on the Increase in the Amount of Pr Atoms for Cs-Ion-Implanted Pd/CaO Multilayer Complex with Deuterium Permeation", Japanese Journal of Applied Physics, Volume 52.10R (2013)

[9] S. Tsuruga et al "Transmutation Reaction Induced by Deuterium Permeation Through Nanostructured Multi-layer Thin Film", Mitsubishi Heavy Industries Technical Review, Volume 52, 4 (2015)

[10] A. Kitamura et al "In situ accelerator analyses of palladium complex under deuterium permeation". Condensed Matter Nuclear Science (2006)

[11] P. A. Mosier-Boss "It is Not Low Energy – But it is Nuclear", Journal of Condensed Matter Nuclear Science, volume 13 (2014)

[12] S. Szpak and F. Gordon "Chemical aspects of the Pd/^{N}H–H_2O system in its nuclear active state" (2011)

[13] M. McKubre et al "The Emergence of a Coherent Explanation for Anomalies Observed in D/Pd and H/Pd Systems; Evidence for ^{4}He and ^{3}He Production", proceedings of the ICCF-8 International Conference on Condensed Matter Nuclear Science, Bologna, Italy (2000)

[14] G. S. Qiao et al "Nuclear transmutation in a gas-loading H/Pd system", Journal of New Energy, volume 2.2 (1997)

[15] T. Ohmori et al "Nuclear transmutation reaction occurring during the light water electrolysis on Pd electrode", International Journal of the Society of Materials Engineering for Resources, volume 6.1 (1998)

[16] G. C. Fralick et al "Transmutations observed from pressure cycling palladium silver metals with deuterium gas", International Journal of Hydrogen Energy, volume 45 (2020)

[17] A. Kovacs et al "The Bose-Einstein condensation of electrons: a long overdue discovery of how superconductors really work", Zitter Institute (2025)

CHAPTER 10

A simple demonstration of nuclear electrons

Andras Kovacs[1]
[1] ExaFuse. E-mail: andras.kovacs@broadbit.com

10.1. Halogen lamps based experimental method

Inspired by Alexander Parkhomov's halogen lamp experiments [**1**], we operate halogen lamps under elevated AC voltage. We choose this method because working with halogen lamps is relatively simple, and their mass production facilitates experimental replicability. Under elevated voltage operation, the tungsten filament temperature reaches around 2500°C temperature, and carries over 20 000 A/cm^2 current density; this is about the highest current density that any metallic wire may carry without breaking up. In a halogen lamp, the current density going through a filament is maximized immediately after turning the lamp on, when the cold filament resistance is still low. To periodically reach such a maximized current density, we operate halogen lamps under repeating ON-OFF regime. The ratio of ON and OFF times is adjusted such that the lamp surface would not overheat.

We employ halogen lamps designed for 220 V operation. These lamps have 400 W nominal power. When operated at 300 V AC voltage; the consumed power is ∼600 W.

10.2. Gamma radiation during continuous lamp operation

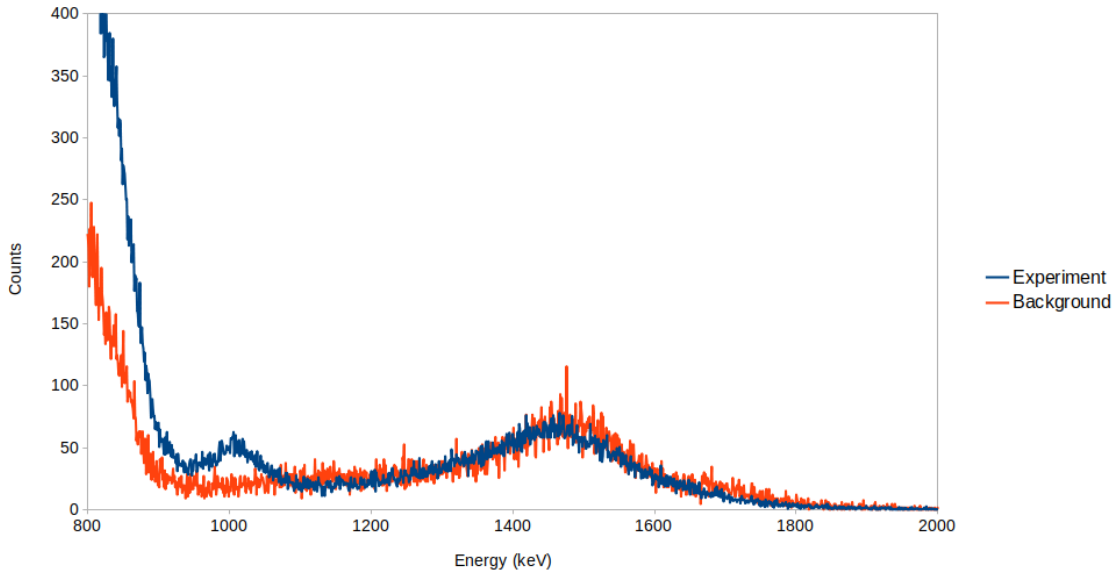

FIGURE 10.2.1. The gamma spectrum during the elevated voltage halogen lamp experiment.

A halogen lamp was immersed into $Li_2B_4O_7$ powder, contained in an air-cooled steel enclosure. This lamp is then operated at 300 V AC voltage. We used an NaI detector

based gamma spectrometer, which was placed next to the enclosure. The ratio of ON-OFF times are adjusted so that the lamp surface temperature would not exceed 300°C. The gamma spectrum was measured over the course of 30 hours.

In the 0.1-0.9 MeV range, we did not detect any excess gamma signal. In the 1-2 MeV range, we measured the gamma spectrum shown in figure 10.2.1. The peak at 1460 keV is the ^{40}K peak of the background. The faint peak around 1 MeV appears only in the experiment, and we note that this newly appearing gamma peak location is approximate because our spectrometer has a low energy resolution. The presence of this 1 MeV gamma peak demonstrates that some low-intensity nuclear reaction has been initiated in the halogen lamp.

10.3. Analysis of composition changes

Several lamps were operated at 300 V AC voltage for 8 days, in ambient air. The repeating ON-OFF regime was used. Most lamps remained operational at the end of our experiment.

After the experiment, filaments from fresh lamps versus post-experiment lamps were analyzed by X-Ray Fluorescence (XRF) method. For this measurement, we broke the lamps open, and removed filament pieces by a tweezer. Our XRF instrument measures in the 1-20 keV range, and the spectra of fresh versus post-experiment filaments differ only in the 6-7 keV region: figure 10.3.1 shows an Fe peak appearing in the filament spectrum of 8 days operated lamps. This excess signal is small, but statistically significant.

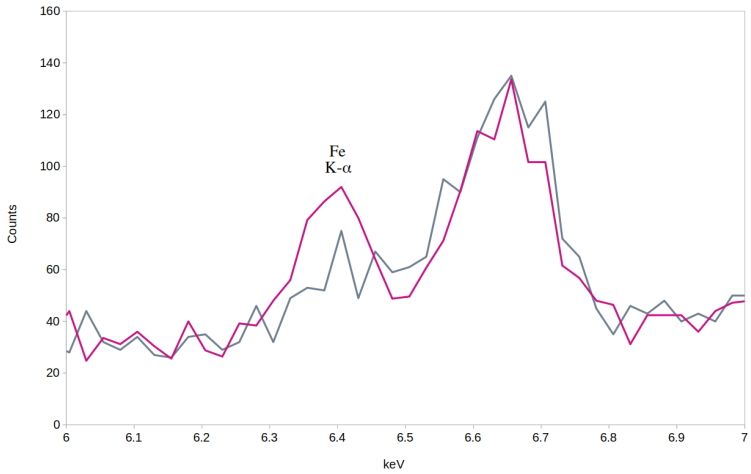

FIGURE 10.3.1. The 6-7 keV XRF spectra of tungsten filaments, measured at 40 kV XRF voltage setting. Gray: filament pieces from fresh lamps. Red: a filament pieces from post-experiment lamps.

Since Fe is the only newly appearing element in post-experimental filaments, other reaction counter-products must have been emitted from the filament. To detect other reaction products, fresh lamps versus post-experiment lamps were also analyzed by XRF. We used intact lamps for this measurement, and measured XRF spectra at 40 kV XRF voltage setting. At such photon energy, x-rays mostly pass through the quartz encasing. The spectra of fresh versus post-experiment lamps differ only in the 4-5 keV region: figure 10.3.2 shows an Xe peak appearing in the spectrum of 8 days operated lamps[1].

[1]We note that a 4.1 keV peak could potentially correspond to Sc as well. However, Sc can be excluded in this case because it has a very similar melting and boiling temperature to Fe. If Sc was present, it would have been detected in the filament's XRF scan as well, but the filament's spectrum does not contain any 4.1 keV peak.

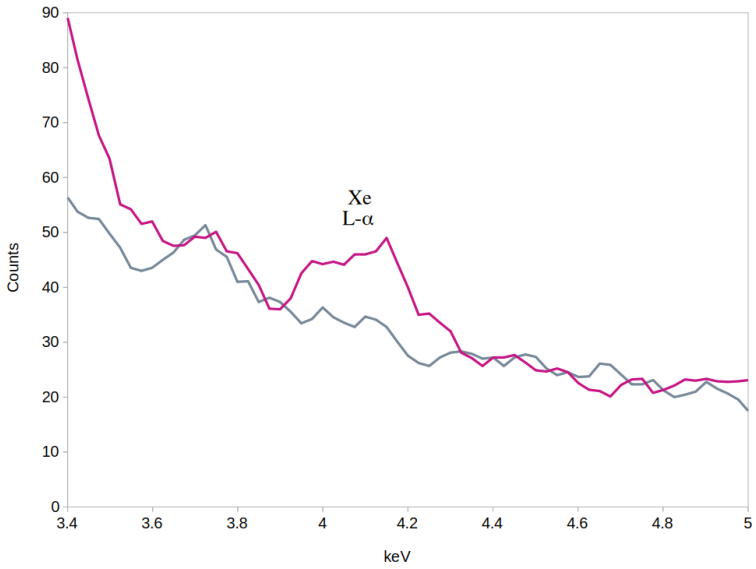

FIGURE 10.3.2. The 3.4-5 keV XRF spectra of intact halogen lamps, measured at 40 kV XRF voltage setting. Gray: fresh lamps. Red: post-experiment lamps.

We emphasize that the XRF instrument measures the average composition of the given sample, or sample region. It is not sensitive microscopic local variations of sample composition.

10.4. Discussion

We observe only two newly appearing elements in our halogen lamp experiment, namely: Fe and Xe. Unlike the randomly varying fission products of neutron-mediated uranium fission, the reaction products of our experiment indicate one well-defined nuclear reaction. The occurring nuclear reaction is corroborated by the excess gamma photon measurement during the experiment. We did not detect excess radioactivity from post-experiment lamp samples. It means that the occurring nuclear reaction produces stable isotopes.

The Fe and Xe reaction products demonstrate that a small fraction of tungsten nuclei splits into two nuclear fragments. Accounting for mass and charge conservation, we obtain the following tentative nuclear fission reaction:

$$(10.4.1) \qquad {}^{186}_{74}W \rightarrow {}^{56}_{26}Fe + {}^{130}_{54}Xe + 6e^{-}$$

where we used the main iron isotope mass and an exemplary tungsten isotope mass.

The above nuclear reaction formula is exothermic by 105 MeV. While most of this reaction heat is carried away by neutrino radiation that always accompanies nuclear electron emission, some fraction is carried by the reaction products' kinetic energy. Therefore, by varying the halogen lamp operating conditions from mildest to harshest, a growing excess heat production is anticipated. Such a calorimetric excess power measurement is reported in reference [**1**]; it confirms a growing excess power as the halogen lamp operating condition is varied from mildest to harshest.

A key point of formula 10.4.1 is that the emission of six electrons happens promptly during the fission reaction. When Fe and Xe are the end-products, tungsten must fission directly into these elements for several reasons. Firstly, a hypothetical fission into short-lived parent isotopes would have produced much higher excess gamma radiation than what we have detected. Secondly, xenon cannot be a beta decay product because its parent

isotopes such as ^{130}Te, ^{128}Te, and ^{126}Te are practically stable. Thirdly, iron cannot be a beta decay product because its parent calcium isotopes would be grotesquely neutron-rich and would decay by neutron emission.

Regarding the triggering mechanism of such nuclear fission, readers may wonder whether tungsten fission is directly triggered by a high current density condition, or whether a high current density condition firstly leads to some special state of tungsten atoms. We find an important clue in reference [**1**]: in several experiments, a rather significant tungsten concentration is observed outside of the quartz tube - as if the evaporated tungsten gained the ability to pass through quartz. Such a strange condition of certain tungsten atoms implies their much smaller atomic size than the Si-O distance in quartz. The last chapter of reference [**2**] reports meta-stable atoms that appear to be in exactly such a compact state. This last chapter of reference [**2**] is cited in the preceding chapter as well; the meta-stable atomic states described in reference [**2**] might be the key to uncovering the triggering mechanism of novel nuclear reactions.

In conclusion, the prompt nuclear emission of numerous electrons demonstrates the reality of the nuclear electron model described in chapters 6-7.

Acknowledgements: This research received partial funding from the European Union's Horizon2020 research and innovation program under grant agreement no. 951974, and received partial funding from Marc Fleury (LENR Capital). The author thanks Alexander Parkhomov for useful discussions. The XRF measurements have been performed at the FinFocus company.

Bibliography

[1] A.G. Parkhomov, R.V. Karabanov, and E. Belousova "Investigation of LENR Processes Near Incandescent Metals", Journal of Condensed Matter Nuclear Science, Volume 36 (2022)

[2] A. Kovacs et al "The Bose-Einstein condensation of electrons: a long overdue discovery of how superconductors really work", Zitter Institute (2025)